

Wavelength-Preserving Polarization-Insensitive All-Optical 3R
Regenerator Based on Self- and Cross-Phase Modulation and
Offset Filtering Utilizing Raman Amplification

by

Sung Han Chung

A thesis submitted to the
Department of Electrical and Computer Engineering
in conformity with the requirements for
the degree of Doctor of Philosophy

Queen's University
Kingston, Ontario, Canada

October 2009

Copyright © Sung Han Chung, 2009



Library and Archives
Canada

Published Heritage
Branch

395 Wellington Street
Ottawa ON K1A 0N4
Canada

Bibliothèque et
Archives Canada

Direction du
Patrimoine de l'édition

395, rue Wellington
Ottawa ON K1A 0N4
Canada

Your file Votre référence
ISBN: 978-0-494-65311-1
Our file Notre référence
ISBN: 978-0-494-65311-1

NOTICE:

The author has granted a non-exclusive license allowing Library and Archives Canada to reproduce, publish, archive, preserve, conserve, communicate to the public by telecommunication or on the Internet, loan, distribute and sell theses worldwide, for commercial or non-commercial purposes, in microform, paper, electronic and/or any other formats.

The author retains copyright ownership and moral rights in this thesis. Neither the thesis nor substantial extracts from it may be printed or otherwise reproduced without the author's permission.

AVIS:

L'auteur a accordé une licence non exclusive permettant à la Bibliothèque et Archives Canada de reproduire, publier, archiver, sauvegarder, conserver, transmettre au public par télécommunication ou par l'Internet, prêter, distribuer et vendre des thèses partout dans le monde, à des fins commerciales ou autres, sur support microforme, papier, électronique et/ou autres formats.

L'auteur conserve la propriété du droit d'auteur et des droits moraux qui protègent cette thèse. Ni la thèse ni des extraits substantiels de celle-ci ne doivent être imprimés ou autrement reproduits sans son autorisation.

In compliance with the Canadian Privacy Act some supporting forms may have been removed from this thesis.

While these forms may be included in the document page count, their removal does not represent any loss of content from the thesis.

Conformément à la loi canadienne sur la protection de la vie privée, quelques formulaires secondaires ont été enlevés de cette thèse.

Bien que ces formulaires aient inclus dans la pagination, il n'y aura aucun contenu manquant.


Canada

Abstract

Optical regeneration has the potential to significantly increase the reach of long-haul transmission systems. In this thesis, wavelength-preserving polarization-insensitive all-optical 3R regeneration is investigated and demonstrated for 10 and 40 Gb/s signals. The all-optical regenerator utilizes a self-pulsating laser for clock recovery, cross-phase modulation (XPM) based spectral broadening in a highly nonlinear fiber (HNLF) and offset filtering for retiming, and self-phase modulation based spectral broadening in a HNLF and offset filtering for reshaping. Raman amplification is used to increase the XPM-based spectral broadening and thus allow a design that meets the tradeoffs involved in simultaneously achieving good retiming and reshaping performance. The regenerator is shown to reduce amplitude noise and timing jitter while not causing a BER penalty. To fully validate the regeneration scheme, the cascadability is demonstrated using a recirculating loop. For a 10 Gb/s signal, with a regenerator spacing of 240 km, a return-to-zero, on-off-keyed (RZ-OOK) signal was transmitted over 18,000 km (75 loops) with a power penalty of 1.6 dB at a BER of 10^{-9} compared to the back-to-back case. For a 40 Gb/s signal, with a regenerator spacing of 80 km, a RZ-OOK signal was transmitted over 8,000 km (100 loops) with a power penalty of 1.2 dB. In addition, all-optical 3R regeneration is demonstrated using a multimode

quantum-dot Fabry P erot laser with ultra-low timing jitter.

Acknowledgments

I am truly blessed to have Dr. John C. Cartledge as my supervisor for the Ph.D. program. Throughout the long journey of the education, he has always been supportive, kind, and patient for me. He not only gave me flexibility in doing research but also thoroughly supervised me so that I would not deviate too much for no gain. I sincerely respect his knowledge, diligence, thoroughness, and insight for research. Without his supervision, it was not possible for me to come this far.

I want to express thanks to all the members of the Lightwave Systems Research Lab for their willingness to cooperate and help each other. Special thanks to Chris Ito, Na Young Kim, and Xufeng Tang for their help to expand my knowledge in the area of optical communications. I should also acknowledge Patricia Greig for her excellent support and National Microelectronics and Photonics Testing Collaboratory for providing with equipment for the experiment. I also want to thank the staffs of the Department of Electrical and Computer Engineering for their administrative work.

I cannot forget to acknowledge Haewon Kim, not only my wife but also best friend. She has always been with me throughout the program and I am thankful for her support and cheer. Finally I would like to dedicate this thesis to my parents. I am deeply grateful for their unconditional love and support for me.

Table of Contents

Abstract	i
Acknowledgments	iii
Table of Contents	iv
List of Tables	vii
List of Figures	viii
Acronyms	xiv
Chapter 1:	
Introduction	1
1.1 Optical Networks	1
1.2 All-optical regeneration	6
1.3 Literature review	9
1.4 Problem overview and motivation	15
1.5 Thesis contribution	16

Chapter 2:

All-Optical 3R Regenerator	19
2.1 Introduction	19
2.2 Retiming stage	22
2.3 Reshaping stage	52
2.4 Performance measures and methodology	61
2.5 Summary	72

Chapter 3:

The Regenerator for a 10 Gb/s Signal	73
3.1 Experimental setup	74
3.2 Characterization of the regenerator	79
3.3 Performance of the 3R regenerator	86
3.4 Summary	103

Chapter 4:

The Regenerator for a 40 Gb/s signal	104
4.1 Redesign of the regenerator for 40 Gb/s	105
4.2 Performance of the regenerator	117
4.3 Recirculating loop experiment	128
4.4 Summary	133

Chapter 5:

Quantum-Dot Laser and Its Application	134
5.1 Redesign of the regenerator	135

5.2	Performance of the regenerator	138
5.3	Summary	148
Chapter 6:		
	Conclusions	149
6.1	Summary and contributions	149
6.2	Conclusions	151
6.3	Future work	152
	Bibliography	153

List of Tables

3.1	Regenerator parameters for a 10 Gb/s signal.	78
3.2	Parameters for the recirculating loop experiment for a 10 Gb/s signal.	92
4.1	Regenerator parameters for a 40 Gb/s signal.	119
4.2	Parameters for the recirculating loop experiment for a 40 Gb/s signal.	129
5.1	Regenerator parameters with a QD-FP laser for a 40 Gb/s signal. . .	141

List of Figures

1.1	Simple block diagram of the 3R regenerator.	9
2.1	An example of the conventional all-optical 3R regenerator.	20
2.2	An example of a conventional all-optical 3R regenerator that is wavelength-preserving	20
2.3	Block diagram of the proposed all-optical 3R regenerator.	21
2.4	Block diagram of the retiming stage	22
2.5	Illustration of the three section DFB laser.	23
2.6	Schematic illustration of the amplitude spectrum of the reflectivity. . .	24
2.7	Schematic illustration of the spectral location of the two detuned DFB sections.	25
2.8	Schematic illustration of the operating principle for the retiming stage; XPM-HNLF: XPM inducing HNLF.	28
2.9	Measured relative group delay for 1 km of highly nonlinear fiber	30
2.10	Dependence of the calculated chirp on the time delay for a 10 Gb/s signal.	34
2.11	Dependence of the calculated chirp on the time delay for a 40 Gb/s signal	35
2.12	Measured XPM broadened spectra of the data signal	36

2.13 Schematic illustration of the optical spectra of the pump and probe signals	44
2.14 Schematic illustration of the Example 4.	46
2.15 Measured XPM broadened spectrum with EDFA only.	47
2.16 Measured XPM broadened spectrum with EDFA and Raman amplification.	49
2.17 Measured filter offset versus timing jitter with (a) EDFA only and (b) EDFA and Raman amplification	50
2.18 Schematic illustration of the ideal power transfer function for reshaping.	52
2.19 Schematic illustration of the operating principle for the reshaping stage.	53
2.20 Schematic illustration of the ideal and realistic peak power transfer functions.	62
2.21 Eye diagram and power level distributions.	63
2.22 Simple block diagram of the experimental setup.	66
2.23 Block diagram of the transmitter	67
2.24 Block diagram of the signal degradation	68
2.25 Block diagram of the pre-amplified receiver	70
2.26 Block diagram of the recirculating loop	70
3.1 3R regenerator setup for a 10 Gb/s signal	75
3.2 Experimental setup for a 10 Gb/s signal	76
3.3 Measured filter offset versus timing jitter for the retiming stage only.	79
3.4 Power transfer function of the reshaping stage.	80
3.5 BER versus threshold with different filter offsets.	81

3.6	Optical spectra at several locations in the regenerator	82
3.7	Eye diagrams at several locations in the regenerator	83
3.8	Output versus input RMS timing jitter after retiming and reshaping with SOP scrambling.	84
3.9	BER versus threshold with $\Delta\lambda_{\text{off1}}=-0.3\text{nm}$	85
3.10	Dependence of the BER on the received optical power (ROP) at input signal OSNR = 20 dB.	86
3.11	Output versus input timing jitter with a scrambled SOP and two fixed SOPs.	87
3.12	Dependence of the BER on the input signal OSNR (ROP=-15dBm).	88
3.13	Dependence of the BER on the input signal OSNR (ROP=-38dBm).	89
3.14	Eye diagrams for input signal OSNR of 18 dB and a scrambled SOP	90
3.15	Experimental setup of the recirculating loop	91
3.16	Dependence of the Q-factor on the transmission distance with different regenerator spacings.	93
3.17	Eye diagrams for 1R regeneration with different regenerator spacings	94
3.18	Dependence of the BER on the ROP with 80 km regenerator spacing.	95
3.19	Dependence of the BER on the ROP with 160 km regenerator spacing.	96
3.20	Dependence of the BER on the ROP with 240 km regenerator spacing.	96
3.21	Eye diagrams for 3R regeneration with different regenerator spacings	98
3.22	Dependence of the BER on the ROP after 7,200 km transmission with different regenerator spacings.	99
3.23	Dependence of the BER on the ROP after 80,000 km transmission with different regenerator spacings.	99

3.24	Experimental setup with the regenerator outside the loop.	100
3.25	Dependence of the Q-factor on the transmission distance with the regenerator outside a loop.	101
3.26	Dependence of the timing jitter on the transmission distance with the regenerator outside a loop.	101
3.27	Dependence of the BER on the ROP with the regenerator outside a loop.	102
4.1	Block diagram of the clock recovery and the test setup	106
4.2	Optical spectrum of the self-pulsating laser at 40 GHz	107
4.3	RF spectrum of the detected signal from the self-pulsating laser at 40 GHz	108
4.4	Dependence of the RMS timing jitter on the input signal OSNR.	108
4.5	Eye diagram of the recovered clock signal for an input signal OSNR of 30 dB	109
4.6	Measured relative group delay for 1 km of the XPM-HNLF.	110
4.7	Dependence of the Q-factor in the retiming stage on the filter offset.	113
4.8	Dependence of the RMS timing jitter after the retiming stage on the filter offset.	114
4.9	Dependence of the Q-factor on the filter offset in the reshaping stage only.	115
4.10	Dependence of the RMS timing jitter on the filter offset in the reshaping stage only.	116
4.11	Regenerator setup for a 40 Gb/s signal	117

4.12	Experimental setup of the regenerator for a 40 Gb/s signal	120
4.13	Optical spectra of the data signal at several locations in the regenerator	121
4.14	Optical spectra of the clock signal after XPM-HNLF with and without the data signal	122
4.15	Dependence of the Q-factor on the input signal OSNR.	123
4.16	Eye diagrams without and with the 3R regenerator for input signal OSNR values of 15, 18, and 21 dB	124
4.17	Dependence of the output signal RMS timing jitter on the input signal RMS timing jitter.	125
4.18	Dependence of the BER on the input signal OSNR of the regenerator with a ROP of -15 dBm.	125
4.19	Dependence of the BER on the input signal OSNR of the regenerator with a ROP of -32 dBm.	126
4.20	Dependence of the BER on the input signal OSNR of the regenerator with input SOP scrambled and different received optical powers.	127
4.21	Loop experiment setup for a 40 Gb/s signal.	128
4.22	Dependence of the Q-factor on the transmission distance.	130
4.23	Dependence of the RMS timing jitter of the output signal on the trans- mission distance.	130
4.24	Dependence of the BER on the ROP with 80 km regenerator spacing.	131
4.25	Eye diagrams for 1R and 3R regeneration with a different number of loops	132
5.1	Optical spectrum of the quantum-dot laser	136

5.2	RF spectrum of the free-running quantum-dot laser	137
5.3	Dependence of the RMS timing jitter of the retimed signal on the filter offset.	138
5.4	Block diagram of the regenerator using the quantum-dot laser.	139
5.5	Optical spectra at several locations in the regenerator	143
5.6	Experimental setup of the regenerator using the quantum-dot laser. . .	144
5.7	Dependence of the Q-factor on the input signal OSNR of the regener- ator using the QD-FP laser.	144
5.8	Eye diagrams without and with the regenerator using the QD-FP laser	145
5.9	Dependence of the output signal RMS timing jitter on the input signal timing jitter of the regenerator using the QD-FP laser.	146
5.10	Dependence of the BER on the input signal OSNR of the regenerator with the ROPs of -15 dBm and -30 dBm.	147

Acronyms

3R reamplification, reshaping, and retiming

AAPN Agile All-Photonic Network

AOM acousto-optic modulator

ASE amplified spontaneous emission

AWG arbitrary waveform generator

BBS broad band source

BER bit error ratio

CD chromatic dispersion

CW continuous wave

DC direct current

DCA digital communication analyzer

DCF dispersion compensating fiber

DFB distributed feedback

DSF dispersion shifted fiber

DUT device under test

DWDM dense wavelength division multiplexing

EAM electroabsorption modulator

ED error detector

EDFA erbium doped fiber amplifier

ER extinction ratio

FEC forward error correction

FP Fabry P erot

FWHM full width at half maximum

FWM four-wave mixing

GVD group-velocity dispersion

HNLF highly nonlinear fiber

LD laser diode

MZ Mach-Zehnder

MZM Mach-Zehnder modulator

NOLM nonlinear optical loop mirror

NRZ non-return to zero

NZDSF non-zero dispersion-shifted fiber

OBPF optical bandpass filter

OEO optical to electrical to optical

OOK on-off-keyed

OSA optical spectrum analyzer

OSNR optical signal to noise ratio

PMD polarization mode dispersion

PPG pulse pattern generator

PRBS pseudo-random bit sequence

PTF power transfer function

QD quantum dot

QD-FP quantum-dot Fabry P erot

RF radio frequency

RMS root mean squared

ROP received optical power

RSD relative standard deviation

RZ return to zero

RZ-OOK return to zero on-off keyed

SBS stimulated Brillouin scattering

SDH synchronous digital hierarchy

SMF single mode fiber

SNR signal-to-noise-ratio

SOA semiconductor optical amplifier

SONET synchronous optical network

SOP state of polarization

SP self-pulsating

SP-DFB self pulsating-distributed feedback

SPM self-phase modulation

SPM-HNLF SPM highly nonlinear fiber

TDM time division multiplexing

TOD tunable optical delay

VOA variable optical attenuator

WDM wavelength division multiplexing

XAM cross absorption modulation

XGM cross gain modulation

XPM cross-phase modulation

XPM-HNLF XPM highly nonlinear fiber

Chapter 1

Introduction

1.1 Optical Networks

In the near future, more sophisticated types of data traffic will be required compared to the current demand. For example, on demand interactive high definition internet TV may prevail over conventional cable or satellite TV and internet based networking between homes and businesses will evolve beyond what has been predicted. In accordance with the trend, packet type data traffic is also rapidly increasing as the internet attempts to reach everyday electronic systems and appliances such as computers, cell phones, video games, TVs, and home heating systems. This will require a communication network that can provide a large bandwidth for end users. Moreover, the network should provide a flexible means to accommodate various types of data traffic.

For decades, optical networks have provided a large amount of bandwidth for applications from metro to long haul and hold the key potential for next generation communication networks. Optical networks provide high capacity and possibly reduced

costs for new applications. Therefore optical networks are strong candidates for the foundation of next generation communication networks.

1.1.1 Brief history of optical networks

Telecommunication networks have evolved from simple telephone point to point service to data transmission at a rate of over a terabit per second. Over the last century, communication networks have gone through different stages from asynchronous to synchronous and to optical [1–3].

Asynchronous networks

The beginning of digital networks was based on asynchronous technology. In asynchronous networks, each network component used its own clock source. Thus due to variations of the different clock sources, signals from different transmitters exhibited variations in time at the receiver. Moreover, there was not a standard to maintain and evolve the network to a higher level. Thus, as companies started to develop network components, they were not necessarily compatible with products made from other companies.

Synchronous networks

In a synchronous network, the digital transitions in the signals occur at exactly the same rate. Although there may be phase differences between two signals due to propagation delays, timing jitter, etc., it should be traceable and within an acceptable range. The demand for standardized networks pushed the development of networks such as

the synchronous optical network (SONET) in the U.S. and Canada (or synchronous digital hierarchy (SDH) in the rest of the world). SONET is a standardized optical communication transport that transfers multiple digital bit streams over optical fibers. In SONET, standards have been set for various aspects such as line rates, forward error correction (FEC) schemes, bit rate hierarchies, and operations and maintenance functionality. It also detailed the required network elements, network architectures and functionality. Manufactured network components can be used interchangeably.

One of the characteristics that enabled SONET to survive through ever increasing bandwidth requirements is scalability. SONET has an open-ended hierarchy so that, in theory, the bit rate can be scaled without any upper limit. However, as the bit rate increases (e.g., 40 Gb/s), the physical limitation of the optical components (e.g., laser source, optical fiber properties, etc.) make SONET less practical. Moreover, end users are demanding a variety of services that require different types of traffic. To accommodate such demands, a new type of optical network is needed that can offer large bandwidth and flexibility.

Optical networks

To increase the capacity of the network without changing too many of the existing network components, optical networks have employed wavelength division multiplexing (WDM) technology. Optical networks have defined network architectures based on wavelengths but do not specify detailed requirements on bit rates or frame structures. Specific network components are determined depending on how the wavelengths are transmitted, groomed, or implemented in the network.

Networks can be divided into several layers. The highest layer is the service layer, in

which data traffic is generated and transmitted into the telecommunications network. The second layer is the SONET layer that provides restoration, performance monitoring, and provisioning. The SONET layer is transparent to the service layer. Third is the optical layer. The ideal optical layer would replace the SONET layer by doing the same functions in the optical domain. In practice, due to the limitation of the state-of-the-art technology, the optical layer will probably complement the SONET layer and provide similar functionality as SONET with more operations performed in the optical domain. For example, high speed data signals with nonstandard SONET formats will be able to be transmitted over the optical layer bypassing the SONET layer. The optical layer is still being defined by the standards body. It will eliminate many optical to electrical to optical (OEO) conversions as the data traffic is processed in the optical domain. This will remove the potential bottleneck due to the speed limitation of electronics (although the speed of electronics is also increasing rapidly) and offer an environmentally friendly solution by reducing the power consumption of the high speed electronics.

1.1.2 Agile All-Photonic Networks

The demand for networks that support high capacity and flexibility rapidly increases to accommodate various types of data traffic such as voice, text, image, movie, broadcasting, etc. Current fiber optic communications networks involve OEO conversions for signal processing in the intermediate nodes but it is more desirable to process the signal in the optical domain. With the development of all-optical switches, the all-photonic network is drawing much interest. The all-photonic network will reduce

OEO conversions in the intermediate nodes and allow fiber optics to reach close to the end users.

In 2003, acknowledging the benefit of all-photonic networks, Canadian universities, companies, and government laboratories established a research network called Agile All-Photonic Network (AAPN). The objective of the AAPN research network was to expand the reach of the all-photonic network closer to the end users with no use of OEO conversion for the data flow [4]. To achieve this, two main research directions were set; the development of the network architecture and enabling technologies.

For the network architecture, an overlaid star network was proposed [5]. To achieve high bandwidth and flexibility, WDM technology is combined with burst mode time division multiplexing (TDM). The data stream is parsed into small burst of data (i.e., optical packets) to efficiently handle various types of data. The signal processing of the optical data packets is performed all-optically while network management is done using separate control signals either optically or electrically. Optical bursts are routed from one edge node to the other through a core network.

In addition to the network architecture, various optical components need to be developed to support the agility of the all-photonic network. The key enabling optical components include amplifiers, switches, wavelength converters, receivers, and regenerators. Due to the new network architecture, the optical components also need to meet new requirements to handle bursts of signals. For example, high speed optical switching is required to route packet signals and clock recovery must be performed within a fraction of a packet duration. Among these enabling technologies, the optical regenerator is also important since it can significantly increase the transmission reach.

1.2 All-optical regeneration

As an optical signal propagates through a transmission link comprised of fiber and various components, the signal becomes degraded by various impairments such as amplified spontaneous emission (ASE) noise, dispersion, and fiber nonlinearities. In order to transmit the optical signal a longer distance, the signal should be regenerated in the intermediate nodes by cleaning up the accumulated noise and distortion. Optical regeneration can be performed in three ways; reamplification, reshaping, and retiming. If only reamplification is performed using an optical amplifier, it is called 1R regeneration. If the reamplification and reshaping are performed, it is called 2R regeneration. When the retiming function is added, it becomes 3R regeneration.

In order for an optical regenerator to be considered a strong candidate for next generation optical networks, it is necessary that it meets most of the following requirements.

Wavelength preservation

It is desired for the regenerator to preserve the wavelength as the input data signal. If the output signal wavelength is different from that of the input signal, the optical network would have to be carefully designed to manage the wavelength changes in the intermediate nodes, which will induce significant complexity in the network design. Some regeneration techniques, such as those based on four-wave mixing (FWM) and self-phase modulation (SPM) with offset filtering, normally end up with a different output signal wavelength compared to the input data signal wavelength [6–8].

Polarization insensitivity

The performance should be assured for any state of polarization (SOP) of the input data signal. Regeneration methods that are sensitive to the SOP of the input data signal are not very practical since most optical components do not have a means to compensate for polarization effects. For SOP sensitive regeneration methods, added complexity is required to achieve polarization-insensitive regeneration.

Cascadability

Another important requirement for a regenerator is cascadability. A regenerator is designed to operate in the intermediate nodes of a network to prevent noise or distortion from accumulating. For long haul transmission, regeneration is required at several intermediate nodes in order to maintain the signal quality. Therefore the optical regenerator must be cascadable without degrading the system performance.

High speed

Because current communication services require more and more bandwidth, it is recommended for the regenerator to operate at higher bit rates. Thus, it is desirable to develop a regenerator that can operate not only at a bit rate of 10 Gb/s but also at bit rates of 40 Gb/s or higher.

Multi-channel regeneration

The majority of research has been done for single channel regeneration. For WDM systems, optical signals are demultiplexed, regenerated, and then multiplexed back for

transmission over the next span. Recently, there are groups of researchers working on multi-channel regeneration techniques [9–12]. In the literature, 4-channel regeneration has been demonstrated [13] but there is a challenge to increase the number of channels that can be simultaneously regenerated.

Integrability

In order to offer a compact solution and reduce the cost, it is desired to have the regenerator integrated in a small package. Semiconductor based regenerators, those that use semiconductor optical amplifiers (SOAs), are good candidates [14–19]. However, due to the slow gain recovery time from SOAs, there is a concern about this regeneration technique for high bit rates. The majority of the SOA based regenerators have been demonstrated for 10 Gb/s signals although there are some results reported at 40 Gb/s [20].

Pulse width

The pulse width of the output signal should be the same as that of the transmitted data signal in the absence of distortion and it should be a practical value. For SPM based regenerators, a narrow pulse width is desired to increase the spectral broadening for the same average launch power to a nonlinear medium (e.g., highly nonlinear fiber (HNLF)). Likewise, for SOA based regenerators, it is also desired to use a narrow pulse width to mitigate pattern effects caused by slow gain recovery time. For example, techniques have been demonstrated for a bit rate of 10 Gb/s using a pulse width of 2 ps [21]. However, the pulse width should not be too narrow from a practical perspective and the duty cycle of the input data signal should be around 33~50%.

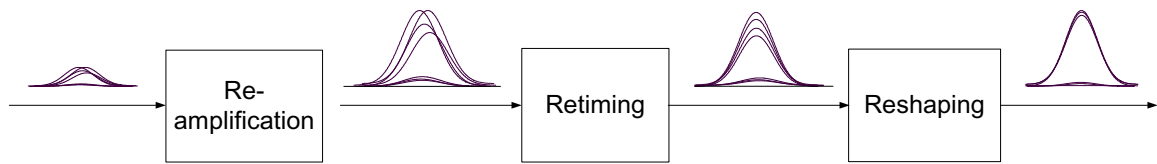


Figure 1.1: Simple block diagram of the 3R regenerator.

1.3 Literature review

In the context of regeneration, 3R represents reamplification, reshaping, and retiming. Fig. 1.1 shows a simple block diagram of the 3R regenerator. A degraded input signal is first amplified to compensate for transmission loss. After the reamplification stage, the signal is realigned in the retiming stage and the amplitude noise is suppressed in the reshaping stage. The order of the retiming and reshaping stages can be interchanged depending on the regenerator structures. An all-optical regenerator performs its regenerative function (i.e., reamplification, reshaping, and retiming) in the optical domain. Reamplification can be done by optical amplifiers such as an erbium doped fiber amplifier (EDFA) or SOA. For retiming, an all-optical clock recovery module is required to provide a reference signal for realigning the jittered data signal. For reshaping, some form of nonlinear optical gate is needed to suppress amplitude noise in the one and zero levels. In this section, the current technologies for optical regeneration are reviewed.

1.3.1 Clock recovery

One of the most important components for 3R regeneration is the clock recovery module. In today's commercial optical network, the clock recovery can be done electrically using a phase locked loop [22]. In the literature, methods are found that combine

optical and electrical signal processing [23,24]. For electrical clock recovery, the locking time using a phase locked loop is typically on the order of micro-seconds [25] which is not fast enough for optical burst networks. For example, AAPN has defined a packet duration of 10 μ s and a guard time of 1 μ s. Thus the clock recovery should be done in the nano-second time scale. On the other hand, many optical clock recovery schemes have also been reported [26–38]. All-optical clock recovery can be done using a Brillouin active filter [33], Fabry P erot (FP) filter [34, 35, 37], temporal Talbot effect [39], or self-pulsating (SP) laser [27, 28, 32]. Among them, a SP laser can provide fast clock recovery on the order of nano-seconds suitable for all-optical regeneration [27, 28, 32, 40]. A SP laser is a semiconductor based laser that outputs a pulsed signal rather than a continuous wave (CW) signal with a DC input current. When the data signal is injected to the SP laser, free running self pulsation is locked to the data signal producing a recovered clock signal. In this thesis, SP lasers are used for all-optical clock recovery which will be further discussed in Sec. 2.2.1.

1.3.2 Nonlinear optical signal processing

To regenerate the signal in the optical domain, nonlinear optical signal processing is required to gate the data signal all-optically. For 2R regeneration, an input data signal is applied to an optical gate that has a step-like nonlinear power transfer function so that the amplitude noise in the one and zero levels is suppressed. For 3R regeneration, a control signal is generated for the nonlinear optical gate from the input data signal and the control signal gates either a data signal or recovered clock signal depending on the regeneration scheme.

Cross absorption modulation

One way to gate an optical signal is by using cross absorption modulation (XAM) in an electroabsorption modulator (EAM) [41–43]. When a pump signal (e.g., data) enters the EAM, it modulates the absorption of a probe (e.g., clock) signal. The advantage of XAM using the EAM is that it is compact and can be integrated with other semiconductor components. The disadvantage is that EAMs were not originally designed for XAM and it is challenging to handle high input power needed to saturate the absorption [43]. Further research is required to achieve a high speed, strong XAM process for low input power. In addition, the absorption is dependent on the SOP of the input signal [43] and wavelength [44, 45], which address issues to be used for signal regeneration.

Cross gain modulation

Cross gain modulation (XGM) in an SOA can be used to perform signal processing [20, 46–52]. XGM occurs when a pump signal modulates the gain of a nonlinear medium and hence the power of a probe signal. The SOA also allows integration of the device with other semiconductor devices. However, SOAs have a relatively slow gain recovery time that causes pattern effects for high bit rates [53–56]. They also add ASE noise that degrades the signal-to-noise-ratio (SNR) [57].

Four-wave mixing

In addition, FWM can be used to achieve a nonlinear optical gate in a nonlinear medium such as a HNLF [6, 58]. The process is based on the nonlinear phenomenon called

the Kerr effect [59]. When more than two optical signals with different frequency copropagate along a nonlinear medium, new frequency components can be generated due to the modulation of the refractive index at different frequencies. FWM also occurs in SOAs that are designed to have high nonlinearities. However, ASE and the low FWM efficiency can affect the performance [60–62]. Although the FWM process has been shown to be effective for signal regeneration, it is sensitive to the SOP of the input data signal [59] and to the data wavelength once the pump wavelength is determined. Parametric amplification has also been used to regenerate the optical signal [63]. Parametric amplification is similar to FWM but the copropagating probe signal can be amplified through parametric nonlinear interactions from the pump signal.

Self- and Cross-phase modulation

One of the most studied nonlinear effects in the optical signal processing is the SPM caused by the Kerr effect. The SPM process is polarization independent and has a femto-second response time [59]. Thus it is suitable for high speed optical signal processing. Mamyshev first demonstrated the SPM based data regeneration [64] and since then many research groups have investigated the SPM process in the context of regeneration both numerically and experimentally [7, 65–73].

Another nonlinear process caused from the Kerr effect is cross-phase modulation (XPM). In XPM, a time varying intensity change of the pump signal causes the probe signal to experience a nonlinear phase modulation which can be used to gate the probe signal [74–80]. XPM can be used in various applications such as Kerr shutters [74, 75], nonlinear optical loop mirrors [76, 77], multiplexers [78], and regenerators [79]. Although the XPM process has been used for many interesting applications,

the disadvantage is that XPM is a polarization dependent process. However, a recent report has shown that with proper design, polarization-insensitive XPM can be achieved [81].

Polarization-insensitive XPM

Although XPM is a polarization dependent nonlinear process, polarization-insensitive XPM can be achieved under certain conditions [81]. Polarization-insensitive XPM techniques have been reported in applications such as demultiplexing [82–84], modulation format conversion [85], and wavelength conversion [86]. Recently, polarization-insensitive all-optical retiming has also been demonstrated [87].

1.3.3 Regeneration schemes

For optical regeneration, a variety of optical signal processing schemes have been investigated [88, 89].

One of the most studied types of the regenerator is that based on SPM in a HNLF and offset filtering as Mamyshev reported in 1998 [64]. The SPM based regenerator can be wavelength-preserving by simply cascading two of them together, in which case the performance can also be improved. In the context of 3R regeneration, an optical signal has been transmitted over 1 million km [69]. In order to reduce the complexity, a bi-directional configuration has been proposed [12, 90, 91]. Special fibers with very high nonlinearity (1000 times higher than that of a single mode fiber (SMF)) have also been used for SPM based regenerators [92, 93]. A number of research groups have characterized the regenerator numerically and analytically [68, 70, 94–97]. Recently,

there have been reports on multi-channel regeneration [12, 98, 99].

FWM is also a nonlinear process that is suitable for optical regeneration [100, 101]. An SOA as well as HNLFF can be used as a nonlinear medium to induce FWM. The regenerative properties of pump-modulated FWM have also been investigated [8, 102]. FWM is a ultra-fast process suitable for high bit rate transmission. However due to its sensitivity to the SOP of the input signals, additional complexity is required to mitigate this problem.

One of the important nonlinear mediums is the SOA because it can be incorporated in a photonic integrated circuit and possibly offers a low cost solution. [15, 16, 20]. Recently, a 10 Gb/s signal has been transmitted over 1 million km using an SOA based Mach-Zehnder interferometer in the context of 3R regeneration [14].

In addition, there are other methods to achieve optical regeneration, such as nonlinear optical loop mirrors [77, 103–105], saturable absorbers [106, 107], parametric amplifiers [108], and EAMs [41].

1.3.4 Retiming

Retiming has been successfully demonstrated utilizing synchronous modulation by transmitting optical signals over 1 million km [14, 69]. In this method, a portion of the optical signal is converted to an electrical signal for electrical clock recovery, which is then used to remodulate the data signal using an optical modulator.

All-optical retiming is generally achieved using the nonlinear interaction between data and recovered clock signals [79, 109]. Some techniques are not of practical interest when the regenerative performance has a dependence on the SOP of the

input data signal (e.g., conventional XPM). To cope with the issue, other techniques can be used to achieve the polarization-insensitive retiming. Some of the techniques include signal depolarization [110], polarization diversity, [111], fiber twisting [86], and polarization independent XPM [82]. In addition, preprocessing of the input data signal can be used to fix the SOP of the input data signal (e.g., wavelength conversion).

1.4 Problem overview and motivation

Many research groups have investigated all-optical 3R regenerators in order to develop a regenerator that meets the requirements described in Sec. 1.2. However, unfortunately, there has not been a regenerator that meets all of the requirements and further research is necessary to make the regenerator a strong candidate for optical network components.

Recently, an all-optical regenerator has been demonstrated that is based on cross- and self-phase modulation and offset filtering [65]. The regenerator, which is based on ultra-fast nonlinear processes and is polarization-insensitive, was demonstrated for a 10 Gb/s return to zero on-off keyed (RZ-OOK) signal. It also operates for a practical pulse width (duty cycle of 40%) and the output signal has the same pulse width as the input signal.

In order to fully validate the regenerator, a recirculating loop experiment should be performed. In such an experiment, the optical signal repeatedly circulates inside a loop which requires that the regenerator be wavelength-preserving. However, the initial implementation of the regenerator was not wavelength-preserving because the optimum offset in the retiming stage was different from the optimum offset in the

reshaping stage and each stage was separately optimized. Hence it was not possible to demonstrate the cascability .

The demonstration of the cascability of the regenerator using a recirculating loop experiment is very important. Since the regenerator is based on the nonlinear transfer function, it is not straightforward to analyze the performance. Furthermore, there have been cases that a regenerator has shown good performance when it was used once but failed to perform well when it was cascaded several times in a recirculating loop for long-haul transmission [112].

1.5 Thesis contribution

Although a variety of optical regeneration techniques have been proposed, none of them has yet met all the requirements to become a strong candidate for optical networks. Among the many types of regenerators, XPM/SPM based regeneration has met many requirements and has potential for further improvement. This thesis further investigates the XPM/SPM based regenerator and provides the following contributions;

1. Raman amplification is utilized in the retiming stage and polarization-insensitive retiming is achieved which allows wavelength-preserving regeneration. As the offset was increased in the retiming stage to preserve the wavelength of the input data signal, without Raman amplification, an increased dependency on the SOP of the input data signal was observed. When a Raman pump signal is counter propagated, it is possible to increase the offset in the retiming stage and achieve a small dependency on the SOP of the input data signal. Without Raman

amplification, it is difficult to co-design the retiming and reshaping stages so that the regenerator is both wavelength-preserving and polarization-insensitive, which are critical features from a practical perspective.

2. Design guidelines are formulated for the proposed regenerator at 10 and 40 Gb/s. These guidelines provide important information on the regenerator parameters such as the signal walk-off, filter offset, filter bandwidth, fiber parameters, and peak powers. With these guidelines, one can easily determine most of the important parameters in designing a regenerator.
3. Wavelength-preserving polarization-insensitive all-optical 3R regeneration is demonstrated utilizing Raman amplification for a 10 Gb/s RZ-OOK signal. The regenerator does not cause a bit error ratio (BER) penalty while it reduces the amplitude noise and timing jitter. The regenerator is shown to be polarization-insensitive and preserve the input signal wavelength and pulse width.
4. Cascadability of the regenerator is demonstrated using a recirculating loop at 10 Gb/s. With a regenerator spacing of 240 km, a 10 Gb/s RZ-OOK signal was transmitted over 18,000 km (75 loops) with a power penalty of 1.6 dB compared to the back-to-back case at a BER of 10^{-9} . When the 3R regenerator was not used, the power penalty was about 6 dB after 960 km (4 loops). Within a laboratory setting, a loop experiment provides the ultimate test of a regenerator.
5. The regeneration scheme is demonstrated at a bit rate of 40 Gb/s. In order to increase the bit rate from 10 to 40 Gb/s, a different SP laser was used to recover the clock signal at 40 GHz and key regenerator parameters were redesigned. The

regenerator at 40 Gb/s is shown to suppress the amplitude noise and timing jitter and does not cause a BER penalty.

6. Cascadability of the regenerator at 40 Gb/s is demonstrated using a recirculating loop. With a regenerator spacing of 80 km, a 40 Gb/s RZ-OOK signal was transmitted over 8,000 km (100 loops) with a power penalty of 1.2 dB compared to the back-to-back case at a BER of 10^{-9} . When the 3R regenerator was not used, the power penalty was over 6 dB after 640 km (8 loops).
7. The all-optical 3R regeneration is demonstrated using a quantum-dot Fabry P erot (QD-FP) laser. Although the QD-FP laser offers benefits such as the ultra-low timing jitter and high Brillouin threshold, it is not suitable for communication systems due to its multimode characteristics. However, the proposed regeneration scheme does not use the recovered clock signal for transmission of the next span and can utilize the benefits of the QD-FP laser.

Chapter 2

All-Optical 3R Regenerator

In the context of regeneration, 3R represents reamplification, reshaping, and retiming. If only reamplification and reshaping are performed, it is called 2R regeneration. When the retiming function is added, it becomes 3R regeneration. In this chapter, the all-optical 3R regenerator is described that is considered in this thesis. In section 2.1, an introduction is given for the all-optical 3R regenerator. In sections 2.2 and 2.3, operating principles are described for the retiming and reshaping stages, respectively. In section 2.4, performance measures and methodology are discussed and a summary is given in section 2.5.

2.1 Introduction

The conventional scheme for optical regeneration is shown in Fig. 2.1. First, the input data signal is split into two paths. One path is used to recover the clock signal and the other path is applied to the nonlinear optical gate to modulate the clock

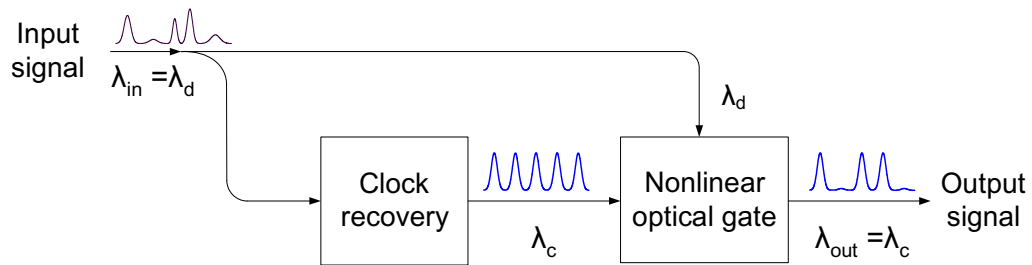


Figure 2.1: An example of the conventional all-optical 3R regenerator.

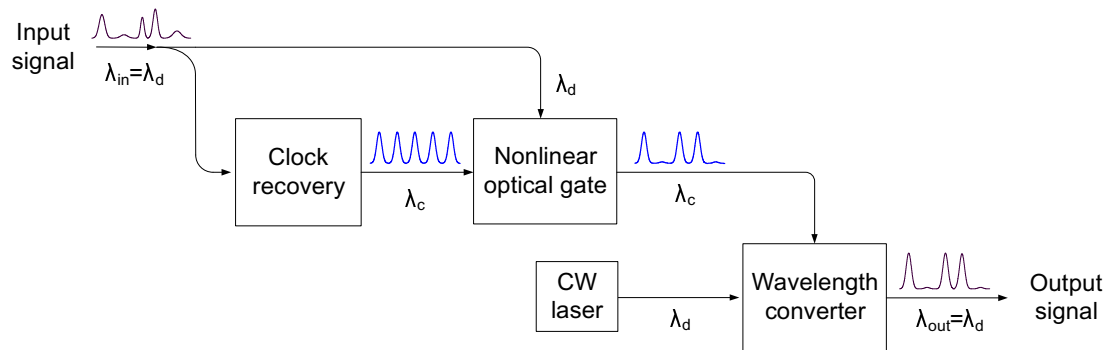


Figure 2.2: An example of a conventional all-optical 3R regenerator that is wavelength-preserving; CW: continuous wave.

signal. In this scheme, the clock signal wavelength (λ_c) is generally different from the data signal wavelength (λ_d). From a practical point of view, it is important to keep the wavelength of the regenerated signal the same as the input data signal. Thus, additional complexity is required to obtain wavelength-preserving regeneration (e.g., a wavelength converter or second stage regenerator to bring the wavelength back to the input data signal wavelength). Fig. 2.2 shows an example of a regenerator that preserves the wavelength of the input data signal. In this regeneration scheme, an additional CW source is used at the same wavelength as the input data signal. Thus

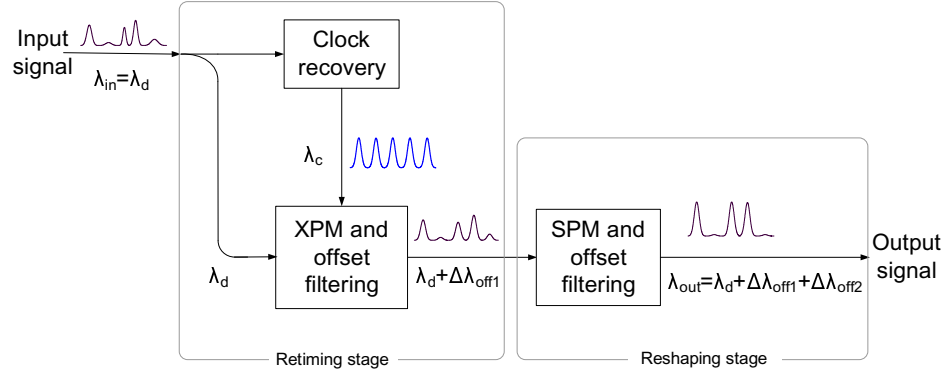


Figure 2.3: Block diagram of the proposed all-optical 3R regenerator.

for a WDM application, the wavelength of the CW laser source needs to match the wavelength of the data signal.

The all-optical 3R regenerator proposed in this thesis is wavelength-preserving as shown in Fig. 2.3. The regenerator is comprised of a retiming stage and a reshaping stage. In the retiming stage, a SP laser is used to recover the clock signal which induces XPM on the data signal in a nonlinear medium (e.g., HNLFF). The offset filter in the retiming stage with a filter offset of $\Delta\lambda_{\text{off1}}$ is used to slice a portion of the spectrum to retime the data signal. In the reshaping stage, SPM based spectral broadening and offset filtering with a filter offset of $\Delta\lambda_{\text{off2}}$ reduces amplitude noise in the one and zero levels [64]. If the two filter offsets in the retiming and reshaping stages meet the following condition,

$$\Delta\lambda_{\text{off1}} + \Delta\lambda_{\text{off2}} = 0, \quad (2.1)$$

then the overall regeneration scheme is wavelength-preserving.

In the following, each part of the regenerator is discussed in detail as well as the performance measures used to evaluate the regenerator performance.

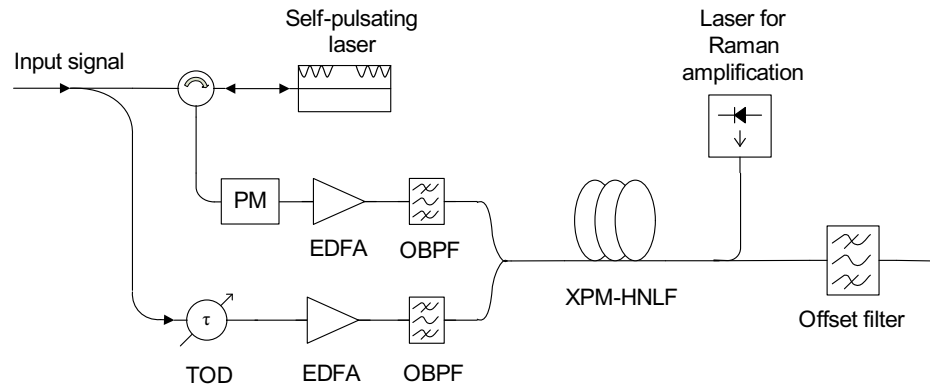


Figure 2.4: Block diagram of the retiming stage; PM: phase modulator, EDFA: erbium doped fiber amplifier, OBPF: optical bandpass filter, TOD: tunable optical delay, XPM-HNLF: XPM inducing highly nonlinear fiber.

2.2 Retiming stage

The retiming stage consists of a clock recovery module, HNLF with Raman amplification for XPM, and offset filter. Fig. 2.4 shows a block diagram of the retiming stage. The input signal is split and one path is applied to the SP laser via an optical circulator to produce a clock signal that is used as a pump signal for XPM in the HNLF. If the spectrum of the recovered clock signal is narrow (e.g., a self pulsating-distributed feedback (SP-DFB) laser), stimulated Brillouin scattering (SBS) can occur in the XPM-HNLF. The clock signal is thus phase modulated to increase the SBS threshold. The clock signal is then amplified and filtered to remove ASE noise out-of-band of the signal. The other path for the data signal includes a tunable optical delay (TOD) to properly align the data and clock signals in time before the XPM highly nonlinear fiber (XPM-HNLF). Then the data signal is amplified, filtered and fed into the XPM-HNLF together with the clock signal. At the output of the XPM-HNLF, the offset filter slices a portion of the data signal and the retimed data signal is obtained.

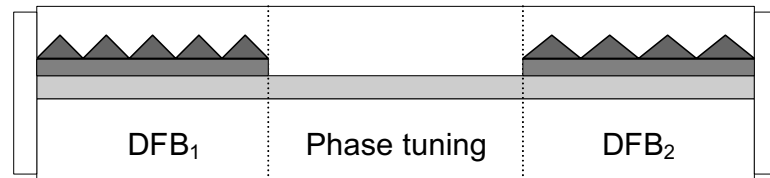


Figure 2.5: Illustration of the three section DFB laser.

2.2.1 Clock recovery

In communication systems, the receiver extracts the clock signal from the data signal in order to properly process the received signal. In the context of all-optical 3R regeneration, a low-jitter optical clock signal is required to retune the data signal. For all-optical clock recovery in this thesis, three different SP lasers are considered; a distributed feedback laser for a 10 Gb/s signal, and a phase controlled mode beating laser and QD-FP laser for a 40 Gb/s signal.

Self pulsating-distributed feedback laser

The self pulsating-distributed feedback (SP-DFB) laser is used to recover a 10 GHz clock signal. It is also called a dispersive self Q-switching laser and consists of three sections in an InGaAsP/InP ridge waveguide [32,113,114]. As shown in Fig. 2.5, two end sections are DFB sections and the middle section is a phase tuning section. One DFB section is injected above threshold and used as a lasing section. The other end section is injected near transparency and used as a dispersive reflector. The phase tuning section is used to fine tune the phase of the facet reflection to meet the condition for self-pulsation. Fig. 2.6 shows the amplitude spectrum of the reflector of the SP-DFB laser. The wavelength of the lasing section is positioned at a point of negative steep slope in the reflectivity of the reflector section. In this condition, a

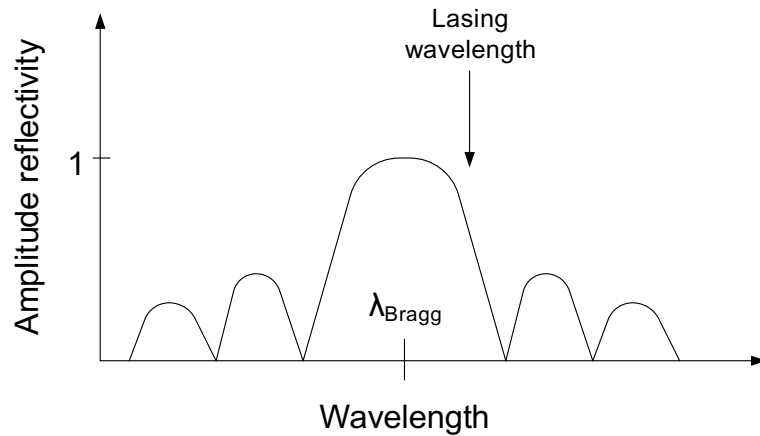


Figure 2.6: Schematic illustration of the amplitude spectrum of the reflectivity.

portion of the signal power is reflected back to the lasing section and the signal power increases. As the signal power increases due to the increased stimulated emission, the carrier density decreases. As the carrier density decreases, chirp occurs, which causes the lasing wavelength to shift to the longer wavelength (i.e., outside of the reflectivity spectrum). As a result, the laser is switched off. Once the laser is switched off, the chirp goes to zero and the lasing wavelength shifts back to the point of negative steep slope in the reflectivity spectrum. Thus the laser is switched back on. In this way, amplitude modulation causes a wavelength modulation due to the change in refractive index and it causes the laser to switch on and off. The SP frequency can be tuned by adjusting the injection currents (mainly the lasing section).

Phase controlled mode beating laser

For a 40 Gb/s signal, a phase controlled three section mode beating laser is used to recover the clock signal [27, 113–115]. The laser consists of two DFB sections at both ends and one phase tuning section in the middle. The structure of the laser

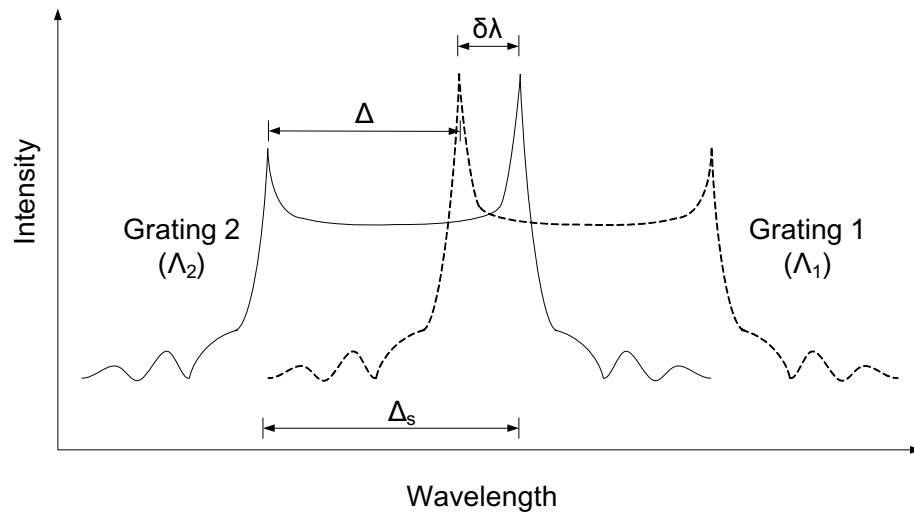


Figure 2.7: Schematic illustration of the spectral location of the two detuned DFB sections.

is similar to Fig. 2.5. In this laser, two DFB sections are spectrally detuned with slightly different Bragg wavelengths (Λ_1 and Λ_2) using two different grating periods. (These grating periods are different from those of the SP-DFB laser although the laser structures are similar.) Injection currents for both end sections are set above threshold to operate in the lasing condition. Thus each end section has two main functions; it is a source of one laser mode and a Bragg reflector for the other mode. Fig. 2.7 illustrates the optical spectrum of the two detuned DFB sections. The lasing signal from each section is oscillating in the laser with the slightly detuned reflector on the other side. These two laser modes coexist in the laser and the superposition of these modes produces a beating-type self-pulsation. As shown in Fig. 2.7, the spectral distance $\delta\lambda$ is determined by the difference Δ between the detuning of the two Bragg

wavelengths and the width Δ_s of the stopband given by

$$\delta\lambda = |\Delta - \Delta_s| \quad (2.2)$$

$$= |\Lambda_1 - \Lambda_2 - \Delta_s|. \quad (2.3)$$

Then the SP frequency is determined by the spectral difference $\delta\lambda$ and given approximately as [27]

$$f_0 = \frac{c}{\lambda^2} \delta\lambda. \quad (2.4)$$

The relative detuning is the main parameter to control the self-pulsating frequency and it can be varied by adjusting the injection current of one of the DFB sections.

Passively mode locked quantum dot Fabry P erot laser

A quantum-dot Fabry P erot (QD-FP) laser is a multi-mode laser with quantum dots embedded in a Fabry P erot resonator. In a multimode laser, if all the longitudinal modes are out of phase, the laser emits a CW signal. On the other hand, if all the modes are in phase or locked to each other, the laser emits a SP pulse train with a SP frequency determined by the spacing between the modes. When the longitudinal modes of the laser are locked to each other, it is called a mode locked laser. The SP pulse width is governed by the optical bandwidth. The repetition rate is determined by the frequency spacing between the longitudinal modes of the laser cavity. If a single pulse is assumed to travel inside a FP cavity, the laser output has a repetition rate proportional to the round trip time of the pulse in the cavity. The round trip time depends on the group index N_g and the length of the cavity L . Thus for the FP cavity, the round trip time is

$$T_{\text{round trip}} = \frac{2LN_g}{c}, \quad (2.5)$$

where c is the speed of light. Recently, semiconductor quantum dot (QD) lasers have drawn much interest due to their fast carrier dynamics and broad gain spectrum [28, 40]. The QD-FP laser considered in this thesis is a passively mode locked laser and can achieve lower threshold current, lower chirp, higher gain, and higher thermal stability than quantum well or bulk structures [116]. The single section laser obtains passive mode locking without employing a saturable absorber and the end facets are cleaved forming a FP cavity. Recently developed QD lasers based on InAs/InP can operate in the wavelength of 1.4 - 1.6 μm [116]. One drawback of the QD laser for the clock recovery is that its performance depends on the SOP of the input signal. This can be overcome by employing techniques that make the SOP of the input signal to the QD laser constant. It can be done by utilizing cascaded lasers [117] or adding a wavelength converter in front of the QD laser [118, 119]. However, polarization-insensitive clock recovery using the QD-FP laser is not considered in this thesis and the SOP of the input data signal is fixed when the QD-FP laser is used.

2.2.2 XPM based retiming

Fig. 2.8 shows the operating principle for the retiming stage. The recovered clock signal is used as a pump to induce XPM on the data signal. For simplicity, the data signal is assumed to have small intensity so that the SPM of the data signal is negligible. When the data and clock signals copropagate inside the XPM-HNLF, the clock signal experiences SPM induced chirp and the data signal experiences the XPM induced chirp. Since the induced chirp on the data signal is due to the clock signal, the XPM induced chirp on the data signal is the same for all data pulses. To increase

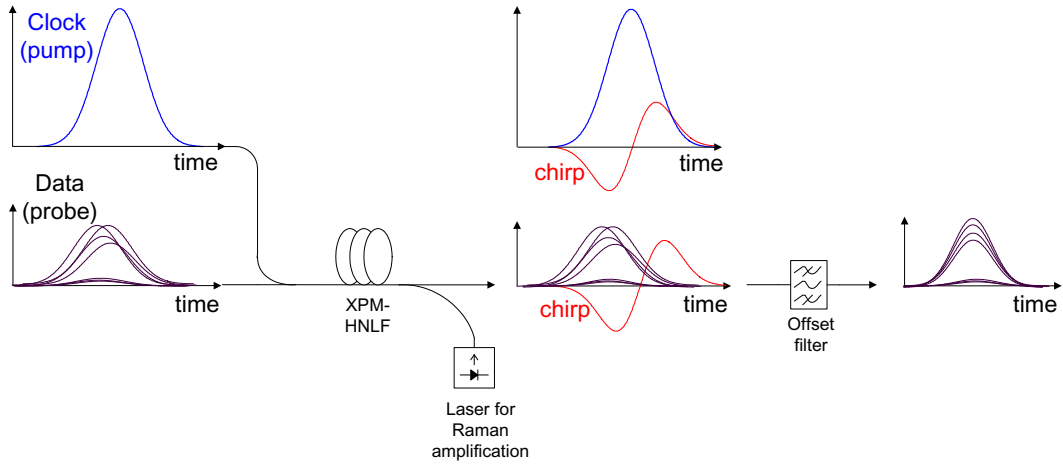


Figure 2.8: Schematic illustration of the operating principle for the retiming stage; XPM-HNLF: XPM inducing HNLF.

the XPM efficiency, a Raman pump signal is counter propagated in the XPM-HNLF. After spectral broadening, an offset filter slices a portion of the data signal to retime the data signal.

XPM induced spectral broadening

For optimal retiming, the data signal spectrum should broaden widely around the offset filter. In order to describe the XPM induced spectral broadening in the XPM-HNLF, we consider the slowly varying pulse envelopes of two signals copolarized and copropagating along a distance z of the fiber with non-overlapping spectra given as

$$A_1(z, t), \quad A_2(z, t). \quad (2.6)$$

For simplicity, the SOPs of the two signals are assumed to be constant during propagation and fiber losses are neglected. Then the governing equations of the two slowly varying pulse envelopes considering group-velocity dispersion (GVD), SPM, and XPM

are given by [59, Sec. 7.4]

$$\frac{\partial A_1}{\partial z} + \frac{i\beta_{21}}{2} \frac{\partial^2 A_1}{\partial T^2} = i\gamma_1(|A_1|^2 + 2|A_2|^2)A_1, \quad (2.7)$$

$$\frac{\partial A_2}{\partial z} + d \frac{\partial A_2}{\partial T} + \frac{i\beta_{22}}{2} \frac{\partial^2 A_2}{\partial T^2} = i\gamma_2(|A_2|^2 + 2|A_1|^2)A_2, \quad (2.8)$$

where β_{2j} and γ_j are the GVD and nonlinearity parameters for the j -th signal ($j = 1, 2$), respectively, and

$$T = t - \frac{z}{v_{g1}}, \quad (2.9)$$

$$d = \frac{v_{g1} - v_{g2}}{v_{g1}v_{g2}}. \quad (2.10)$$

In (2.9), time T is measured in a reference frame of the pulse travelling at speed v_{g1} and in (2.10) d is the group-velocity mismatch parameter obtained from group velocities (v_{g1}, v_{g2}) of the two copropagating signals. If the first pulse is used as a reference with a pulse width of T_0 , the walk-off length L_W and the dispersion length L_D are defined as

$$L_W = \frac{T_0}{|d|}, \quad (2.11)$$

$$L_D = \frac{T_0^2}{|\beta_{21}|}. \quad (2.12)$$

Example 1

10 Gb/s signal

Fig. 2.9 shows the measured dependence of the relative group delay on wavelength for 1 km of fiber. The delay values are relative to the group delay at 1550 nm. Consider a Gaussian shaped pulse

$$U(0, T) = \exp\left(-\frac{T^2}{2T_0^2}\right). \quad (2.13)$$

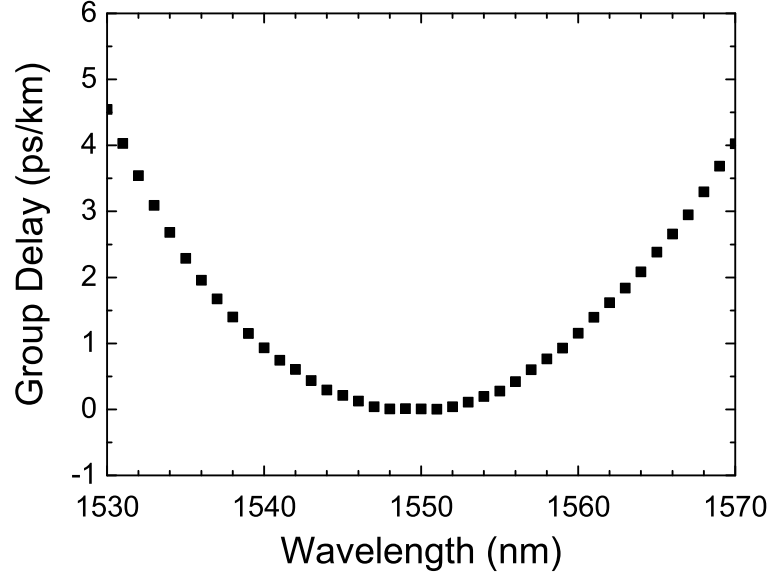


Figure 2.9: Measured relative group delay for 1 km of highly nonlinear fiber. The delay values are relative to the group delay at 1550 nm.

If we assume the pulse widths of the data and clock signals are both 40 ps (full width at half maximum (FWHM)), using the relation for a Gaussian pulse

$$T_{FWHM} = 2\sqrt{\ln 2}T_0, \quad (2.14)$$

the pulse width of $1/e$ intensity point (T_0) is 24 ps. If the data and clock signal wavelengths are 1544 nm and 1538 nm, respectively, the corresponding group delays are 0.29 ps/km and 1.4 ps/km. Then the walk-off length is calculated to be $L_W = 21.6$ km. Compared to a typical length of the XPM-HNLF (e.g., 2 - 4 km), the walk-off length is much longer than the length of the XPM-HNLF. Thus the effect of the signal walk-off is negligible for a 10 Gb/s signal.

40 Gb/s signal

If we assume the pulse width of the data and clock signal is both 11 ps (FWHM) with

the data and clock signal wavelengths of 1545 nm and 1567 nm, respectively. The corresponding group delays are 0.21 ps/km and 2.94 ps/km, respectively. Then the walk-off length is found to be $L_W = 2.42$ km. In this example, the walk-off length is comparable to the length of the XPM-HNLF. Due to the signal walk-off, the XPM efficiency reduces for a 40 Gb/s signal.

For the XPM-HNLF, the dispersion is designed to be small so that pulses do not broaden and the dispersion length is assumed to be much longer than the length of the fiber $L \ll L_D$. In this case, we can ignore the dispersion effect in the nonlinear Schrödinger equation and the propagation equations for the two signals are given as

$$\frac{\partial A_1}{\partial z} = i\gamma_1(|A_1|^2 + 2|A_2|^2)A_1 \quad (2.15)$$

$$\frac{\partial A_2}{\partial z} + d\frac{\partial A_2}{\partial T} = i\gamma_2(|A_2|^2 + 2|A_1|^2)A_2, \quad (2.16)$$

where d is defined in (2.10). The solutions for (2.15) and (2.16) after a fiber length L are given by

$$A_1(L, T) = A_1(0, T)e^{i\phi_1(L, T)} \quad (2.17)$$

$$A_2(L, T) = A_2(0, T - dL)e^{i\phi_2(L, T)}, \quad (2.18)$$

where the nonlinear phase shifts $\phi_1(L, T)$ and $\phi_2(L, T)$ are given by

$$\phi_1(L, T) = \gamma_1 \left(L|A_1(0, T)|^2 + 2 \int_0^L |A_2(0, T - zd)|^2 dz \right), \quad (2.19)$$

$$\phi_2(L, T) = \gamma_2 \left(L|A_2(0, T)|^2 + 2 \int_0^L |A_1(0, T + zd)|^2 dz \right). \quad (2.20)$$

The second terms in (2.19) and (2.20) show the XPM contributions and they depend on the group velocity mismatch. For simplicity, assume the signal pulses have Gaussian

shapes with a pulse width of T_0 with initial amplitudes at $L = 0$, which are given by

$$A_1(0, T) = \sqrt{P_1} \exp\left(-\frac{T^2}{2T_0^2}\right), \quad (2.21)$$

$$A_2(0, T) = \sqrt{P_2} \exp\left(-\frac{(T - T_d)^2}{2T_0^2}\right), \quad (2.22)$$

where P_1 and P_2 are peak powers and T_d denotes the time delay between the two pulses. Substituting (2.21) into (2.19) produces a nonlinear phase term that can be expressed using the error function $\text{erf}(\cdot)$ as [59, Sec. 7.4.1]

$$\phi_1(L, \tau_d, \tau) = \gamma_1 L \left(P_1 e^{-\tau^2} + P_2 \frac{\sqrt{\pi}}{\delta} [\text{erf}(\tau - \tau_d) - \text{erf}(\tau - \tau_d - \delta)] \right), \quad (2.23)$$

where

$$\tau = T/T_0, \quad \tau_d = T_d/T_0, \quad \delta = dL/T_0. \quad (2.24)$$

By taking the derivative of ϕ_1 , the XPM induced frequency chirp on the signal $A_1(L, \tau)$ is given by

$$\begin{aligned} \Delta v_1(L, \tau_d, \tau) &= -\frac{1}{2\pi} \frac{\partial \phi_1}{\partial T} \\ &= \frac{\gamma_1 L}{\pi T_0} \left[P_1 \tau e^{-\tau^2} - \frac{P_2}{\delta} (e^{-(\tau - \tau_d)^2} - e^{-(\tau - \tau_d - \delta)^2}) \right]. \end{aligned} \quad (2.25)$$

If we assume the pump and probe condition ($P_1 \ll P_2$) so that only the XPM effect is significant, the first term in the right hand side of (2.25) can be ignored. In this case, the XPM induced frequency chirp on the probe signal $A_1(L, \tau)$ can be given by

$$\Delta v_1(L, \tau_d, \tau) = -\text{sgn}(\delta) \Delta v_{max} [e^{-(\tau - \tau_d)^2} - e^{-(\tau - \tau_d - \delta)^2}], \quad (2.26)$$

where $\text{sgn}(\cdot)$ is the signum function and the maximum XPM induced chirp Δv_{max} by the copropagating signal A_2 is defined as

$$\Delta v_{max} = \frac{\gamma_1 P_2 \min(L, L_W)}{\pi T_0 |\delta|}, \quad (2.27)$$

where $\min(L, L_W)$ denotes the minimum value between the fiber length L and the walk-off length L_W . It is notable that the maximum XPM induced chirp Δv_{max} increases with the fiber length L but is limited by the walk-off length L_W . For simplicity, fiber loss is assumed to be zero in deriving the above equation. In the wavelength domain, the XPM-induced chirp is expressed as

$$\Delta\lambda_1(L, \tau_d, \tau) = -\text{sgn}(\delta)\Delta v_{max} [e^{-(\tau-\tau_d)^2} - e^{-(\tau-\tau_d-\delta)^2}] \frac{\lambda^2}{c}. \quad (2.28)$$

So far, two propagating signals were assumed to be copolarized. If the SOP of the pump and probe signals is arbitrary, the polarization factor ($\frac{1}{3} \leq b \leq 1$) should be included in the equation;

$$\Delta\lambda_1(L, \tau_d, \tau, b) = -b \cdot \text{sgn}(\delta)\Delta v_{max} [e^{-(\tau-\tau_d)^2} - e^{-(\tau-\tau_d-\delta)^2}] \frac{\lambda^2}{c}. \quad (2.29)$$

If the two copropagating signals are copolarized, the polarization factor b is maximized to 1 and if orthogonally polarized, b reduces to 1/3.

Example 2

10 Gb/s signal

If the length of the XPM-HNLF is 2 km, the signal walk-off is negligible compared to the walk-off length (21.6 km). The relative time delay between the data and clock signals does not change as the two signals propagate down the fiber. When the signal walk-off is negligible, the maximum XPM induced chirp occurs where the slope of the clock signal intensity is steepest. In this case, the delay that maximizes the XPM has been analyzed in [120] to be

$$\Delta T_{d, \max \text{XPM}} = \pm \frac{T_0}{\sqrt{2}}. \quad (2.30)$$

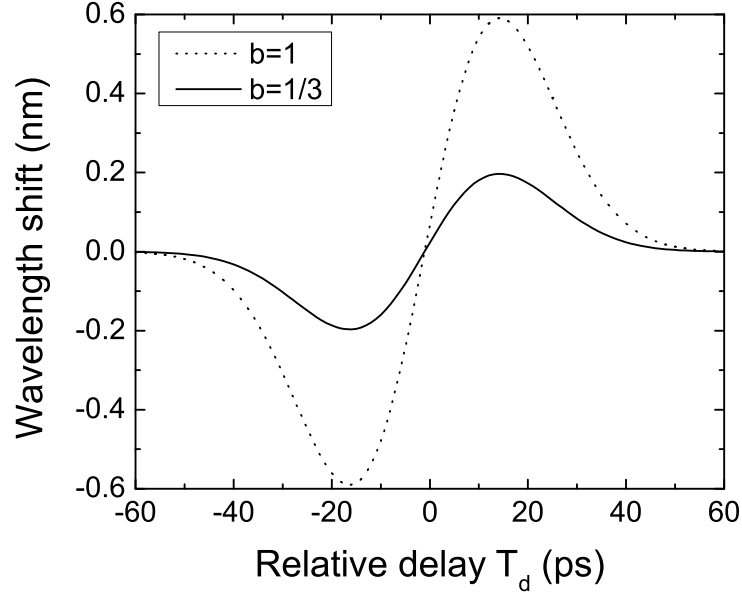


Figure 2.10: Dependence of the calculated chirp on the time delay for a 10 Gb/s signal. Chirp is for the center of the data pulse ($T=0$).

If the pulse width of the clock signal is 36 ps (FWHM) assuming a Gaussian pulse shape, the delay that maximizes the XPM induced chirp is ± 15.3 ps. Fig. 2.10 shows the dependence of the chirp (instantaneous wavelength change) at the center of the data pulse ($T=0$) on the relative time delay between the data and clock pulses. In plotting of (2.29), two values of b were used ($b = \frac{1}{3}, 1$). The peak power of the clock signal (P_2) was 277.8 mW (~ 20 dBm) which is the maximum available launch power to the XPM-HNLF using a typical EDFA. Other parameters are the same as in Example 1. As shown in the figure, maximum chirp occurs at delays of 14 ps and -16 ps which agrees well with (2.30). Small deviation of the delay from the theoretical value is due to the slight walk-off between the two signals. For a peak power of 277.8 mW, the maximum attainable chirp is ± 0.2 nm for signals with the orthogonal SOP

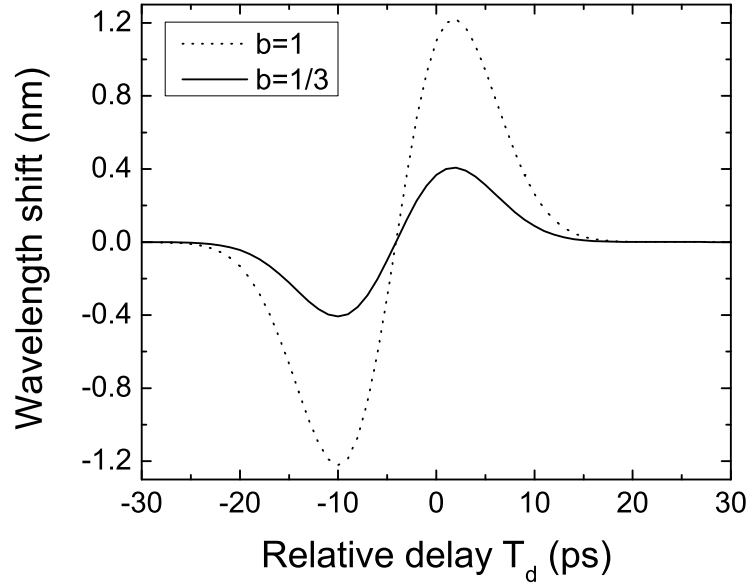


Figure 2.11: Dependence of the calculated chirp on the time delay for a 40 Gb/s signal. Chirp is for the center of the data pulse ($T=0$).

($b = \frac{1}{3}$).

40 Gb/s signal

For a 40 Gb/s signal, the walk-off length is calculated to be 2.41 km from Example 1. It is comparable to the length of the XPM-HNLF and (2.30) is not valid since the signal walk-off can not be ignored. Furthermore, the walk-off effect reduces the XPM efficiency. If the length of the XPM-HNLF is 3 km, the pulse width of the clock signal is 12.5 ps (FWHM), and P_2 is 200 mW (~ 20 dBm), the XPM induced chirp can be obtained from (2.29). Fig. 2.11 shows the dependence of the XPM induced chirp at the center of the data pulse ($T=0$) on the relative time delay T_d . For a 40 Gb/s signal, the signal walk-off causes the maximum chirp to occur at delays of 2 ps and -10 ps. These delays are not centered around 0 ps due to the non-negligible signal

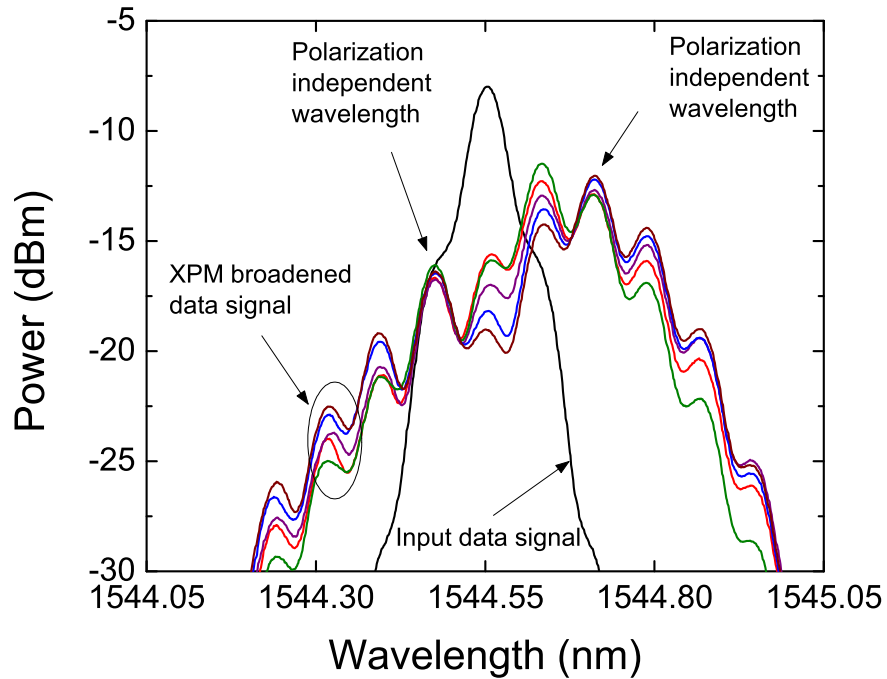


Figure 2.12: Measured XPM broadened spectra of the data signal. Polarization independent-wavelengths are found at offsets of around ± 0.16 nm from the center wavelength. Reprinted with the author's permission [65].

walk-off. The maximum attainable chirp is ± 0.4 nm for signals with the orthogonal SOP ($b = 1/3$).

2.2.3 Polarization independent XPM: spectral crossing

Fig. 2.12 shows optical spectra of the XPM broadened data signal (a 10 Gb/s RZ-OOK signal) with 5 different SOPs of the input data signal. In general, XPM induced spectral broadening varies with the relative SOP between two copropagating signals (i.e., the data and clock signals). Under appropriate conditions, there exist wavelength regions for which the XPM broadened spectrum is polarization-independent. In Fig. 2.12, the dependency of the SOP of the input data signal is minimum at around

± 0.16 nm offset from the center wavelength. Salem *et. al.* analyzed two methods of achieving polarization-independent XPM (i.e., utilizing fiber birefringence and spectral crossing) [81]. For the polarization-insensitive retiming, the spectral crossing method was employed [87].

In the following, the spectral crossing method [81] is revisited to explain under which condition the polarization-independent regions exist in the XPM induced spectral broadening. To begin with, the vector theory of the nonlinear propagation equation is introduced. When two signals are copropagating (i.e., clock and data signals) in the fiber, the total optical field is given by

$$\begin{aligned} \mathbf{E}(x, y, z, t) = & [\hat{\mathbf{x}}A_{1x}(z, t)F_{1x}(x, y)e^{i\beta_{1x}z} \\ & + \hat{\mathbf{y}}A_{1y}(z, t)F_{1y}(x, y)e^{i\beta_{1y}z}]e^{-i\omega_1 t} \\ & + [\hat{\mathbf{x}}A_{2x}(z, t)F_{2x}(x, y)e^{i\beta_{2x}z} \\ & + \hat{\mathbf{y}}A_{2y}(z, t)F_{2y}(x, y)e^{i\beta_{2y}z}]e^{-i\omega_2 t}, \end{aligned} \quad (2.31)$$

where $F_{nm}(x, y)$ and β_{nm} ($n = 1, 2$ and $m = x, y$) are the fiber mode profiles and propagation constants, respectively. $\hat{\mathbf{x}}$ and $\hat{\mathbf{y}}$ are x- and y- polarization unit vectors, respectively. $A_{nm}(z, t)$ is the slowly varying envelope of the electric field component. If the pump ($n = 2$) and probe ($n = 1$) condition is assumed ($P_2 \gg P_1$), the nonlinear propagation equation of the probe signal A_{1x} and A_{1y} can be expressed as [121]

$$\begin{aligned} \frac{\partial A_{1x}}{\partial z} + \beta'_{1x} \frac{\partial A_{1x}}{\partial t} + \frac{i}{2} \beta''_{1x} \frac{\partial^2 A_{1x}}{\partial t^2} = & i\gamma \left(2|A_{2x}|^2 + \frac{2}{3}|A_{2y}|^2 \right) A_{1x} \\ & + \frac{2i\gamma}{3} A_{2x}^* A_{2y} A_{1y} e^{i[(\beta_{2y} - \beta_{2x}) + (\beta_{1y} - \beta_{1x})]z} \\ & + \frac{2i\gamma}{3} A_{2x} A_{2y}^* A_{1y} e^{-i[(\beta_{2y} - \beta_{2x}) - (\beta_{1y} - \beta_{1x})]z}, \end{aligned} \quad (2.32)$$

$$\begin{aligned}
\frac{\partial A_{1y}}{\partial z} + \beta'_{1y} \frac{\partial A_{1y}}{\partial t} + \frac{i}{2} \beta''_{1y} \frac{\partial^2 A_{1y}}{\partial t^2} &= i\gamma \left(2|A_{2y}|^2 + \frac{2}{3}|A_{2x}|^2 \right) A_{1y} \\
&+ \frac{2i\gamma}{3} A_{2y}^* A_{2x} A_{1x} e^{i[(\beta_{2x}-\beta_{2y})+(\beta_{1x}-\beta_{1y})]z} \\
&+ \frac{2i\gamma}{3} A_{2y} A_{2x}^* A_{1x} e^{-i[(\beta_{2x}-\beta_{2y})-(\beta_{1x}-\beta_{1y})]z},
\end{aligned} \tag{2.33}$$

where β'_{nm} and β''_{nm} are the first and the second derivatives of the propagation constant β_{nm} . For simplicity, the pump (clock) signal is assumed to be linearly polarized along the x-axis and remains in this SOP throughout the fiber. This assumption is valid if the fiber length is short since the recovered clock signal from the SP laser has a fixed SOP. Then there is no y-polarization component of the pump signal and $A_{2y} = 0$. This assumption significantly simplifies the propagation equation because the second and third terms in (2.32) and (2.33) vanish and the two simplified equations are given by

$$\frac{\partial A_{1x}}{\partial z} + \beta'_{1x} \frac{\partial A_{1x}}{\partial t} + \frac{i}{2} \beta''_{1x} \frac{\partial^2 A_{1x}}{\partial t^2} = i\gamma 2|A_{2x}|^2 A_{1x}, \tag{2.34}$$

$$\frac{\partial A_{1y}}{\partial z} + \beta'_{1y} \frac{\partial A_{1y}}{\partial t} + \frac{i}{2} \beta''_{1y} \frac{\partial^2 A_{1y}}{\partial t^2} = i\gamma \frac{2}{3} |A_{2x}|^2 A_{1y}. \tag{2.35}$$

If we assume the evolution of the pump signal $A_{2x}(z, t)$ can be determined either analytically or numerically, the above equations can be considered as a linear time-varying system with the input probe signal $A_{1m}(0, T)$ and the corresponding output signal $A_{1m}(L, T)$. We assume the SOP of the probe signal does not change as the signal propagates along the fiber. If the input probe signal is polarized in the x-direction, then the output signal is also polarized in the x-direction. Then the solutions

to (2.34), (2.35) can be expressed as

$$A_{1x}(L, T) = h_x(t), \quad (2.36)$$

$$A_{1y}(L, T) = 0, \quad (2.37)$$

where $h_x(t)$ is a solution obtained by solving (2.34) with the assumption that the input probe amplitude is $A_{1x}(0, t) = \sqrt{\rho(t)}$. On the other hand, if the input probe signal is y -polarized, the output signal can be expressed as

$$A_{1x}(L, T) = 0,$$

$$A_{1y}(L, T) = h_y(t). \quad (2.38)$$

To generalize, the input probe signal with an arbitrary SOP can be expressed as

$$\begin{bmatrix} A_{1x}(0, t) \\ A_{1y}(0, t) \end{bmatrix} = \sqrt{\rho(t)} \begin{bmatrix} e_x \\ e_y \end{bmatrix}, \quad (2.39)$$

where e_m ($m = x, y$) is the normalized complex number indicating the Jones vector of the input signal, which is the vector representation of a polarized signal and satisfies $|e_x|^2 + |e_y|^2 = 1$. Then the output signal is given by

$$\begin{aligned} A_{1x}(L, t) &= e_x h_x(t), \\ A_{1y}(L, t) &= e_y h_y(t). \end{aligned} \quad (2.40)$$

Then, we consider the power spectrum of the output probe signal

$$S(\omega) = |e_x|^2 |H_x(\omega)|^2 + |e_y|^2 |H_y(\omega)|^2, \quad (2.41)$$

where $H_m(\omega)$ is the Fourier transform of $h_m(t)$ ($m = x, y$). So far we have obtained the output power spectrum of the probe with an arbitrary input SOP. In order to have

the polarization-independent region, the XPM induced spectral broadening should be large enough so that the spectra with two extreme SOPs ($|H_x(\omega)|^2$, $|H_y(\omega)|^2$) exhibit spectral crossing at some frequency ω_0 ,

$$|H_x(\omega_0)|^2 = |H_y(\omega_0)|^2 = S_0. \quad (2.42)$$

At this frequency the output power spectral density with an arbitrary SOP is also given by

$$S(\omega_0) = S_0(|e_x|^2 + |e_y|^2) = S_0. \quad (2.43)$$

Therefore, if the copolarized and the orthogonally polarized probe signals (relative to the pump signal) have a spectral crossing point at frequency ω_0 due to XPM, the output spectrum with an arbitrary SOP also crosses the same point at frequency ω_0 . In fact there are more than one crossing points in the spectrum (left and right side of the center wavelength of the probe signal). This verifies the existence of the polarization-independent region under appropriate conditions.

2.2.4 Offset filter for retiming

After the XPM induced spectral broadening, the offset filter is used to slice a portion of the XPM broadened signal, which results in the retimed data signal. The offset filter should be designed so that the output signal of the retiming stage is polarization-insensitive and suitable for the reshaping stage to further suppress amplitude noise. In this section, two most important parameters for the offset filter are discussed; the bandwidth and the filter offset.

Filter bandwidth

The bandwidth of the offset filter affects the pulse width of the output signal. If the same pulse width is desired as the input pulse width, T_{FWHM} , at the output of the offset filter, we can determine the required filter bandwidth [59]. To begin with, we consider a Gaussian shaped input data signal

$$A_1(0, T) = \sqrt{P_1} \exp\left(-\frac{T^2}{2T_0^2}\right), \quad (2.44)$$

where T_0 is the pulse width of the $1/e$ intensity point with the relation $T_{FWHM} = 2\sqrt{\ln 2} T_0$. Then the corresponding spectral width ($1/e$ half-width) is given by

$$\Delta f_0 = \frac{1}{2\pi T_0}. \quad (2.45)$$

Using the relation $\Delta f_{FWHM} = 2\sqrt{\ln 2} \Delta f_0$, the desired FWHM spectral width that produces an output pulse width of T_{FWHM} is given by

$$\begin{aligned} \Delta f_{FWHM} &= 2\sqrt{\ln 2} \Delta f_0 \\ &= \frac{2\sqrt{\ln 2}}{2\pi T_0} \\ &= \frac{2 \ln 2}{\pi T_{FWHM}}, \end{aligned} \quad (2.46)$$

or in the wavelength domain

$$\begin{aligned} \Delta \lambda_{FWHM} &= \frac{\lambda^2}{c} \Delta f_{FWHM} \\ &= \frac{2 \ln 2 \lambda^2}{\pi c T_{FWHM}}. \end{aligned} \quad (2.47)$$

The required filter bandwidth can be calculated from (2.47) to maintain the same pulse width at the output of the filter.

For the retiming stage, the output pulse width is not as restricted as the reshaping stage (i.e., the reshaping stage must preserve the input signal pulse width). Then the desired filter bandwidth is given by

$$BW_{\text{off1}} = a \frac{2 \ln 2 \lambda^2}{\pi c T_{FWHM}}, \quad (2.48)$$

where a is an adjustment factor. There are trade-offs in choosing the value of a . If a is small ($a < 1$), the filter slices only the polarization-independent region and the SOP dependence can be reduced. However, the output power within passband of the offset filter is also reduced. Moreover, the output pulse width gets wider which is disadvantageous for the reshaping stage. If a is large ($a > 1$), output pulse width gets narrower which is desirable to increase the SPM efficiency in the reshaping stage but the SOP dependency increases. We experimentally found that good performance can be achieved when $a \approx 3$.

Example 3

10 Gb/s signal

If the pulse width of the 10 Gb/s input data signal is 40 ps (FWHM), the corresponding spectral width is $\Delta\lambda_{FWHM} = 0.087$ nm. Then with the adjustment factor of $a=3$, the desired bandwidth of the offset filter is $BW_{\text{off1}} = 0.261$ nm for the retiming stage.

40 Gb/s signal

For a 40 Gb/s signal with 11 ps pulse width (FWHM), the corresponding spectral width is $\Delta\lambda_{FWHM} = 0.319$ nm. Then using the same adjustment factor, the desired bandwidth of the offset filter is $BW_{\text{off1}} = 0.957$ nm for the retiming stage.

Filter offset

The optimum filter offset depends on the XPM induced spectral broadening on the data signal and can be predicted from (2.29). In the retiming stage, it is desired to align the offset filter with the frequency chirp around the center of the data pulse (i.e., $\tau = 0$). Then the output power of the offset filter is maximized. By substituting $\tau = 0$ into (2.29), the XPM induced chirp at the center of the pulse is given by

$$\begin{aligned} \Delta\lambda_1(L, \tau_d, \tau, b)|_{\tau=0} &= \Delta\lambda_1(L, \tau_d, 0, b) \\ &= -b \cdot \text{sgn}(\delta) \Delta v_{max} \left(\exp[-\tau_d^2] - \exp[-(\tau_d + \delta)^2] \right) \frac{\lambda^2}{c}, \end{aligned} \quad (2.49)$$

where Δv_{max} is defined in (2.27) and τ_d is the normalized time delay as defined in (2.24). Since $\frac{1}{3} \leq b \leq 1$, the SOP of the pump and probe signals can change the amount of chirp by a factor of 3. Fig. 2.13 shows qualitatively the optical spectra of the pump and probe signals (a) before the XPM-HNLF and (b) after the XPM-HNLF. After the signals propagate along the XPM-HNLF, the XPM induced chirp of the copolarized probe signal ($\Delta\lambda_1(L, \tau_d, 0, 1)$) is 3 times larger than that of the orthogonally polarized probe signal ($\Delta\lambda_1(L, \tau_d, 0, \frac{1}{3})$). If the spectral crossing occurs at a wavelength shift of $\Delta\lambda_0$,

$$\Delta\lambda_1\left(L, \tau_d, 0, \frac{1}{3}\right) < \Delta\lambda_0 < \Delta\lambda_1\left(L, \tau_d, 0, 1\right), \quad \text{if } \Delta\lambda_0 > 0, \quad (2.50)$$

$$\Delta\lambda_1\left(L, \tau_d, 0, 1\right) < \Delta\lambda_0 < \Delta\lambda_1\left(L, \tau_d, 0, \frac{1}{3}\right), \quad \text{if } \Delta\lambda_0 < 0. \quad (2.51)$$

Although the exact spectral crossing point has not been found, it is approximately in the middle of the two wavelength shifts of the spectral peaks between copolarized and orthogonally-polarized signals. Then the offset filter position for the retiming stage is

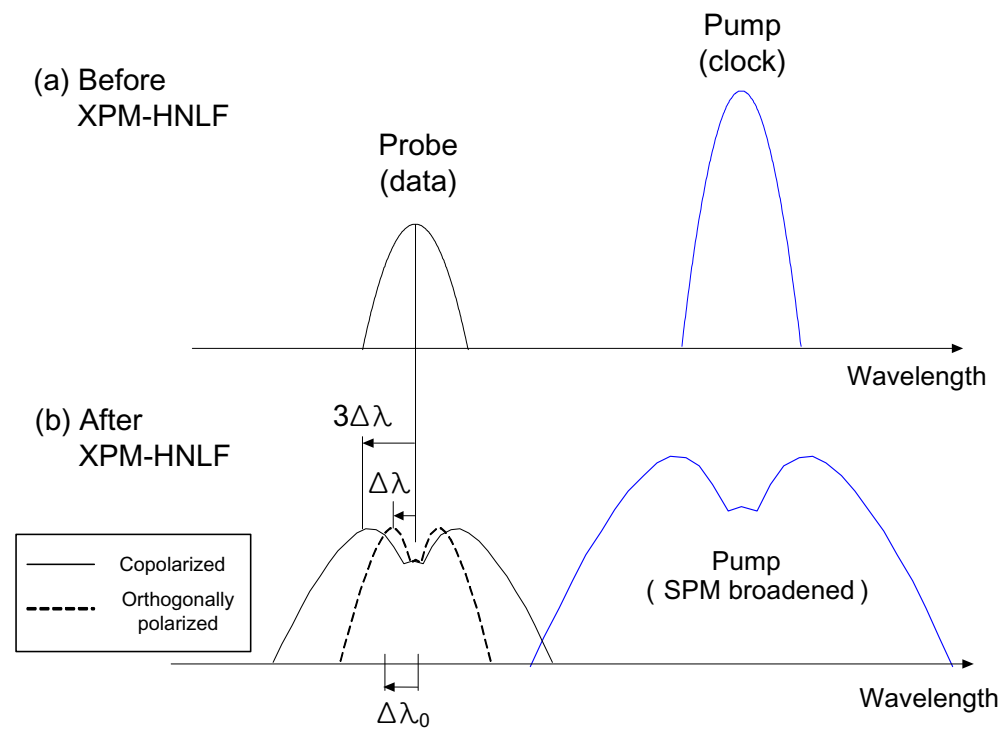


Figure 2.13: Schematic illustration of the optical spectra of the pump and probe signals (a) before XPM-HNLF and (b) after XPM-HNLF. The XPM induced chirp of the copolarized probe signal is 3 times larger than the orthogonally polarized probe signal.

approximately given by

$$\Delta\lambda_{\text{off1}} \approx \frac{1}{2} \left[\Delta\lambda_1 \left(L, \tau_d, 0, 1 \right) + \Delta\lambda_1 \left(L, \tau_d, 0, \frac{1}{3} \right) \right] \quad (2.52)$$

$$\approx 2\Delta\lambda_1 \left(L, \tau_d, 0, \frac{1}{3} \right) \quad (2.53)$$

Example 4

10 Gb/s signal

In Example 2, the time delay (T_d) that maximizes the XPM induced chirp is found to be 14 ps. If the parameter values used in examples 1 and 2 are applied to (2.50), we can obtain the range of the spectral peaks relative to the center wavelength of the data signal given by

$$0.196 \text{ nm} < \Delta\lambda_0 < 0.590 \text{ nm}$$

or the range is 0.39 nm between the peak chirps for the two cases ($b = 1, 1/3$). Using (2.53) and (2.48), if we place the filter at an offset of $\Delta\lambda_{\text{off1}} = 0.39 \text{ nm}$ with a bandwidth of 0.261 nm (as in Example 3), the filter bandwidth is narrower than the range of the spectral peaks. Fig. 2.14(a) illustrates optical spectra for a 10 Gb/s signal. The center wavelength of the optical filter is positioned in the middle of the two spectral peaks. For a 10 Gb/s signal, the filter bandwidth is narrower than the range of the spectral peaks due to the SOP change. Thus the SOP dependency is expected to be smaller.

40 Gb/s signal

For a 40 Gb/s signal, the maximum chirp is obtained when $T_d = 2 \text{ ps}$. Then the range of the spectral peaks is given by

$$0.41 \text{ nm} < \Delta\lambda_0 < 1.23 \text{ nm},$$

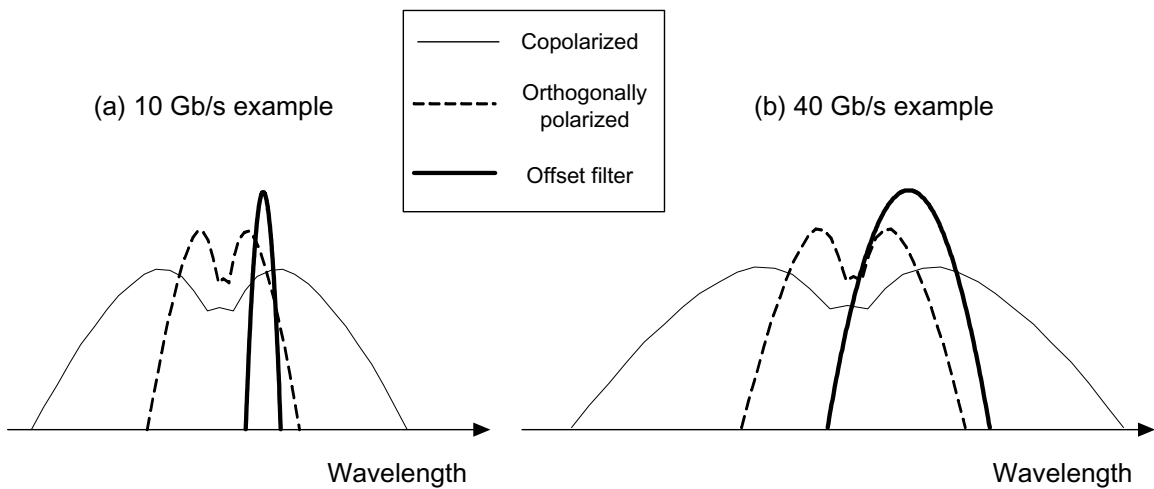


Figure 2.14: Schematic illustration of the Example 4.

or the range is 0.82 nm between the peak chirps for the two cases. If an offset filter with a bandwidth of 0.957 nm is used ($\Delta\lambda_{\text{off}2} = 0.82$ nm), the filter bandwidth is larger than the range of the two peak chirps. Fig. 2.14(b) illustrates optical spectra for a 40 Gb/s signal. The filter bandwidth is wider than the range of the spectral peaks due to the SOP change. In this example, since most of the signal power is contained in the spectral peaks which fall within the passband of the filter, the output power of the offset filter is expected to be larger than that for a 10 Gb/s signal. The tradeoff of choosing the bandwidth of the offset filter has been previously discussed.

2.2.5 Polarization-insensitive retiming

When the offset filter is located in one of the polarization-independent regions, the retiming stage is insensitive to the SOP of the input signal [87, 122]. In the first demonstration of the regenerator, the filter offset was 0.16 nm for the retiming stage

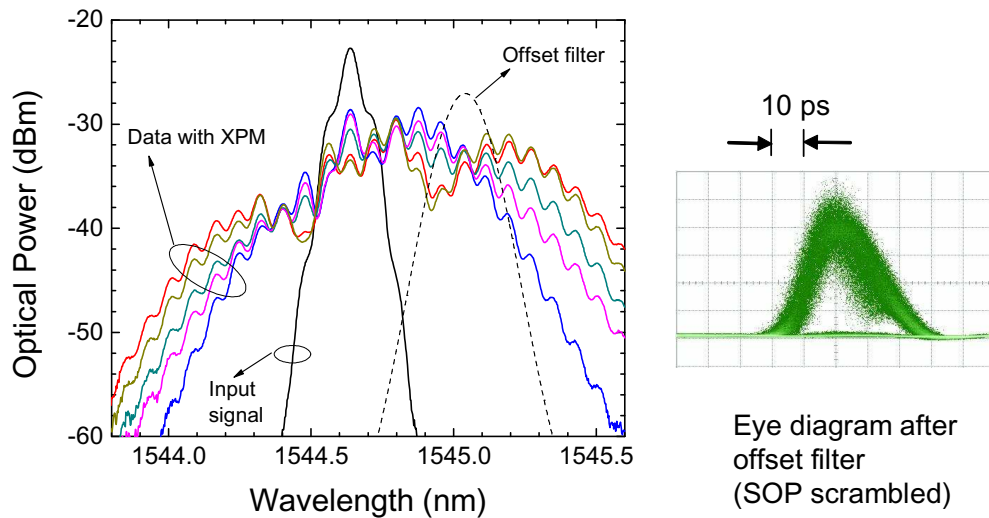


Figure 2.15: Measured XPM broadened spectrum with EDFA only.

and -0.8 nm for the reshaping stage [65]. As shown in Fig. 2.12, when the polarization-independent wavelength is close to the center wavelength (± 0.16 nm), the spectral shapes with different input SOPs can be similar to each other around the polarization-independent region.

In order to preserve the wavelength, the offset must be chosen carefully so that both stages have good performance. In the reshaping stage, the filter offset must be large enough to regenerate zeros in the bit sequence (i.e., the power passed by the offset filter in the absence of SPM is minimal) [64]. In the retiming stage, it is more difficult to achieve polarization-insensitive operation as the offset increases. The XPM broadened spectra become more varied about the polarization-independent wavelength region and the output signal from the offset filter exhibits an increased dependence on the input signal SOP. Fig. 2.15 shows an example of the XPM broadened spectra (with a resolution bandwidth of 0.06 nm) for a 10 Gb/s RZ-OOK signal with 5 different

SOPs of the input data signal (the SOP was fixed for each measurement). The SOP of the clock signal was fixed. The input signal was spectrally broadened by XPM using the clock signal as the pump. To position the spectral crossing point to a target offset (e.g., center wavelength of the offset filter), an EDFA was used to adjust the launch power of the clock signal and fixed while changing the SOP of the data signal. The relative delay between the clock and data signal was adjusted so that the power within the passband of the offset filter was maximized. For an input clock signal launch power of 24.5 dBm, the regions that are independent of the SOP are offsets from the signal wavelength by -0.26 nm and 0.4 nm. The power fluctuation of the filtered signal is minimized for an offset of 0.4 nm. However, the bandwidth of the offset filter (e.g., 0.261 nm) for a 10 Gb/s pulse is wider than the polarization-independent region. Thus the variation in the spectral profiles within the filter passband yields different pulse shapes which results in SOP dependent timing jitter. The eye diagram after the offset filter is also shown in the figure with a scrambled SOP for the input data signal. The asymmetric pulse shape is due to different spectral shapes within the passband of the offset filter with different input SOPs, which causes different output pulse shapes.

2.2.6 Raman amplification

Since the dependence on the SOP of the data signal increases as the filter offset is moved away from the center wavelength, it is difficult to achieve the wavelength-preserving polarization-insensitive regeneration. Introducing Raman amplification to the retiming stage increases the XPM efficiency and provides several benefits. First,

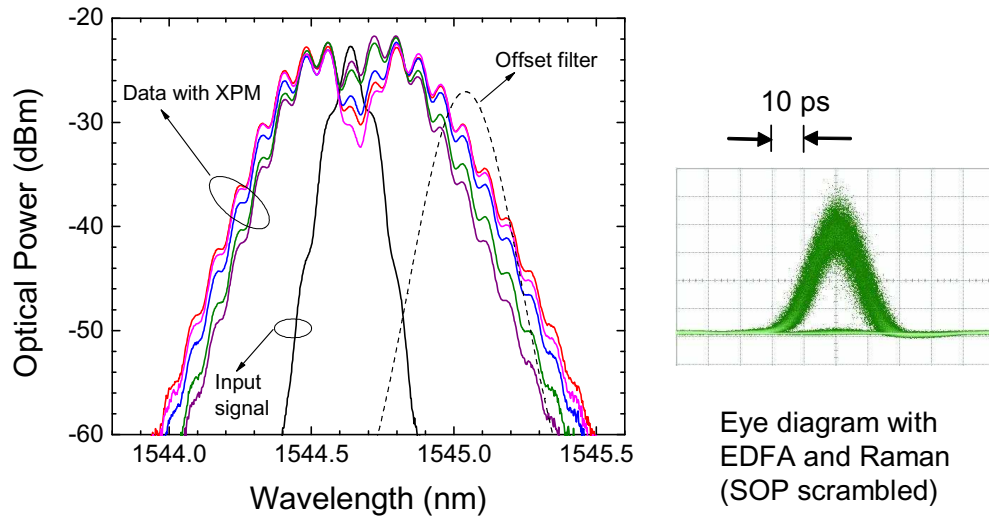


Figure 2.16: Measured XPM broadened spectrum with EDFA and Raman amplification.

the Raman pump signal is counter propagated in the XPM-HNLF which allows for low noise amplification [123]. Second, the counter propagating scheme provides more gain toward the end of the fiber and compensates for the fiber loss. Thus the XPM-HNLF acts as a lossless fiber or a fiber with negative attenuation. Third, since the data signal is also amplified, the output power increases after the offset filter. Last, with the combination of the EDFA and Raman gains, it is possible to reduce the SOP dependency of the spectra within the passband of the offset filter. Fig. 2.16 shows broadened spectra with Raman amplification counter propagating in the XPM-HNLF. The launch power of the clock signal was 17 dBm and the launch power of the Raman pump signal was 27.6 dBm at 1425 nm. Within the filter passband, the broadened spectra exhibit the similar spectral shape but with different power levels. By using the Raman amplification, improved performance can actually be achieved by

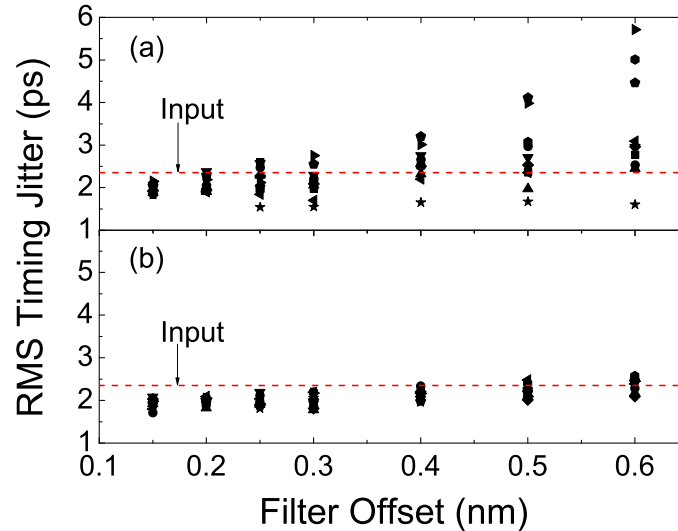


Figure 2.17: Measured filter offset versus timing jitter with (a) EDFA only and (b) EDFA and Raman amplification. Timing jitter is measured for both rising and falling edges with 5 different SOPs of the input data signal.

using a filter offset that slices the outer portion of the XPM broadened spectrum. As shown in the figure, within the filter passband, the broadened spectra exhibit similar spectral shapes but with different power levels. After the offset filter, SOP dependent power fluctuations are transferred into amplitude fluctuations but not into timing jitter. The slowly varying amplitude fluctuation due to the SOP change of the data signal can be reduced in the reshaping stage. The eye diagram with Raman amplification shows an improvement with balanced timing jitter on both the rising and falling edges. Fig. 2.17 shows the dependence of the root mean squared (RMS) timing jitter for the retimed signal on the filter offset after the retiming stage. The optical signal to noise ratio (OSNR) (noise bandwidth of 0.1 nm) and RMS timing jitter of the input signal

were 9 dB and 2.35 ps, respectively. Note that, the input OSNR was intentionally degraded more than a normal operating condition in order to generate the input RMS timing jitter larger than the intrinsic jitter of the recovered clock signal (1.6 ps). This will not have a negative effect on the retiming stage since the RMS timing jitter of the clock signal is still below 2 ps for an OSNR of 9 dB [124]. The RMS timing jitter of the rising and falling edges is given for 5 different SOPs. Other regenerator parameters such as the data and clock powers and the optical delay are separately optimized while the SOP of the input signal was scrambled. Without Raman amplification, as seen in Fig. 2.17(a) the variation of the timing jitter due to the SOP change of the input signal increases with the filter offset. Fig. 2.17(b) shows that with Raman amplification, the retimed signal is much less sensitive to the SOP change of the input signal as the filter offset increases. Compared to the timing jitter of the input signal, timing jitter improvement is observed for all SOPs when the offset is less than 0.4 nm.

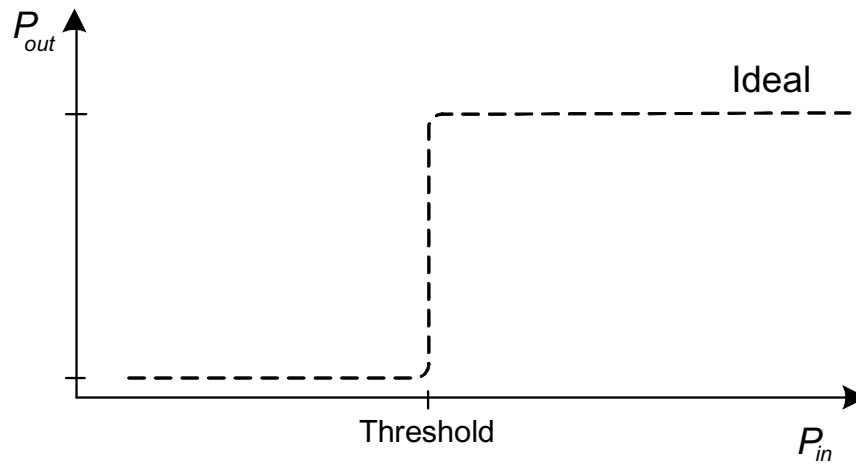


Figure 2.18: Schematic illustration of the ideal power transfer function for reshaping.

2.3 Reshaping stage

The goal of the reshaping stage is to obtain a step-like power transfer function to suppress amplitude noise in the one and zero levels. Fig. 2.18 shows the ideal power transfer function for the reshaping stage. In the reshaping stage, SPM induced spectral broadening and offset filtering is used. For the suppression of the one level, the data signal is amplified so that SPM induced spectral broadening of the signal is large enough for the spectrum to extend over the passband of the offset filter. Fig. 2.19 shows a diagram to explain the operating principle of the reshaping stage. When the pulses with one level enter the SPM highly nonlinear fiber (SPM-HNLF) in the presence of the amplitude noise, different amounts of SPM induced chirp occur. In the wavelength domain, intensity dependent different amounts of spectral broadening occur. By properly placing an offset filter, the power fluctuation can be minimized within the passband of the filter. When the pulses with zero level enter the SPM-HNLF, the spectral broadening is small and the noise in the zero level does not pass

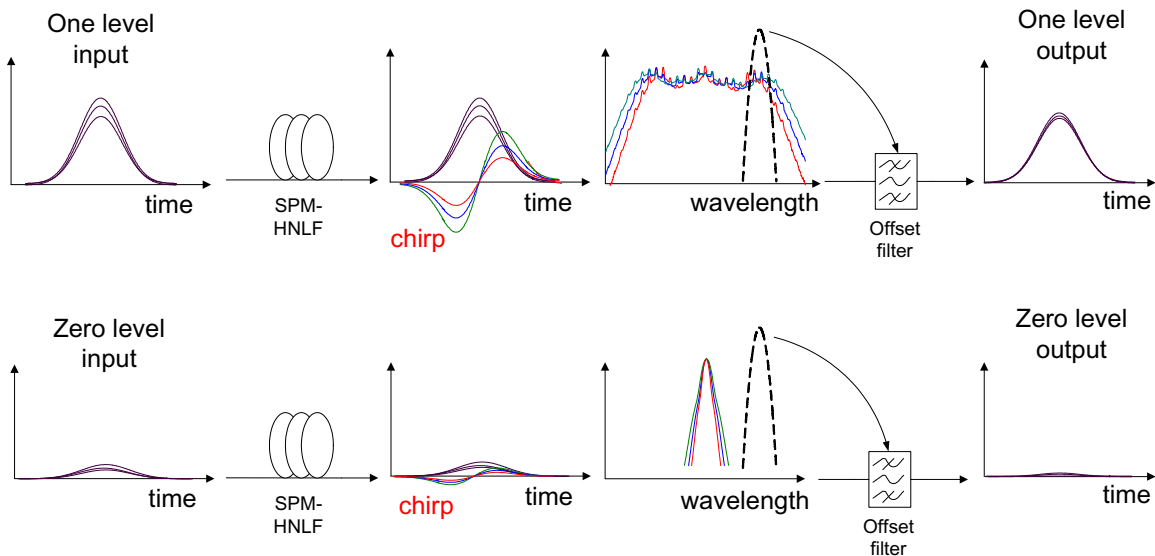


Figure 2.19: Schematic illustration of the operating principle for the reshaping stage.

through the offset filter. Thus, the amplitude noise in the one and zero levels can be suppressed.

2.3.1 Input power and fiber parameters

For the optimum performance of the reshaping stage, the quality of the SPM induced spectral broadening is very important. The broadened spectrum is desired to be as flat as possible to effectively suppress amplitude noise in the one level [64]. Noise suppression for the zero level can be achieved with a large enough filter offset. Design rules for achieving optimum spectral broadening have been investigated in the context of super continuum source generation [125]. The properties of the super continuum source depend on the fiber dispersion, nonlinear processes (e.g., SPM and four-wave mixing), and interplay between them. It has been shown that super continuum generation in the normal dispersion regime (i.e., $D < 0$) allows flatter spectral broadening [59, 126]

which is of the same interest for the reshaping stage. If SPM and GVD are considered, the fiber and data signal parameters can be described with two dimensionless quantities [125]

$$N = \sqrt{L_D/L_{NL}}, \quad (2.54)$$

$$\xi = z/L_D, \quad (2.55)$$

where N and ξ are defined as the soliton order and normalized propagation length at a distance z , respectively. L_D is given by (2.12) and the nonlinear length is defined as $L_{NL} = 1/\gamma P_0$. In order to provide design rules, the fitting of two equations to the results of numerical simulations yielded the maximum spectral magnification factor M_{max} and the corresponding optimum fiber length ξ_{max} as [94]

$$M_{max} \approx c_1 N \quad (2.56)$$

$$\xi_{max} \approx \frac{c_2}{N}, \quad (2.57)$$

where $c_1 \approx 1.1$ and $c_2 \approx 2.1$ were found for the Gaussian shaped seed pulse in the context of super continuum generation. The magnification factor in (2.56) is a ratio between output versus input spectral width (FWHM), and the SPM broadened output spectral width can be given by

$$\frac{\Delta\lambda_{SPM}}{\Delta\lambda_{in}} \approx c_1 N \quad (2.58)$$

$$\Delta\lambda_{SPM} \approx c_1 N \Delta\lambda_{in}, \quad (2.59)$$

where $\Delta\lambda_{in}$ is the spectral width of the input signal. Equation (2.59) implies that the output spectral width due to SPM increases linearly with the soliton order N .

For the reshaping stage, normally dispersive fiber is assumed because it allows flat spectral broadening in the presence of noise [126]. As the signal pulse propagates along

the fiber, the temporal pulse width increases due to the interplay between dispersion and SPM. The pulse width at the output of the SPM-HNLF can be expressed as [94]

$$T_{FWHM,out} \approx 1.2 \frac{L}{L_D} N T_{FWHM,in} < T_{\text{period}}, \quad (2.60)$$

where T_{period} is a bit period. As the pulse width increases over the bit period, interpulse interference degrades the output signal. Thus the output broadened pulse width should be less than the bit period T_{period} [94]. Then we can obtain the available N as

$$\begin{aligned} N_{\text{avail.}} &< \frac{T_{\text{period}} L_D}{1.2 L T_{FWHM,in}} \\ &= \frac{T_{\text{period}} L_D}{2.4 \sqrt{\ln 2} L T_{0,in}} \\ &= \frac{T_{\text{period}} T_{0,in}}{2.4 \sqrt{\ln 2} L |\beta_2|}, \end{aligned} \quad (2.61)$$

where $T_{FWHM,in} = 2\sqrt{\ln 2} T_{0,in}$ is used assuming a Gaussian pulse. Using the relations $N = \sqrt{L_D/L_{NL}}$, $L_{NL} = 1/(\gamma P_0)$, and $L_D = T_{0,in}^2/|\beta_2|$ we can express (2.61) in terms of the peak power. Then the available peak power $P_{0,\text{avail.}}$ is given by

$$P_{0,\text{avail.}} < \frac{T_{\text{period}}^2}{(2.4 \sqrt{\ln 2} L)^2 \gamma |\beta_2|}. \quad (2.62)$$

Equation (2.62) shows that the available peak power is limited by fiber parameters such as length (L), nonlinearity (γ), and GVD (β_2).

Example 5

10 Gb/s signal

Let us assume the output pulse width of the retiming stage is 33 ps (FWHM) with a Gaussian shape. (The pulse width at the output of the retiming stage is shorter than that of the input signal if we set the adjustment factor to be $a = 3$.) If parameters for a

3 km SPM-HNLF are $D = -8$ ps/nm-km and $\gamma = 10.6$ W⁻¹km⁻¹, the dispersion length is obtained to be $L_D = 38.8$ km. Then the available soliton order is $N_{\text{avail.}} < 32.64$ and the available peak power is $P_{0,\text{avail.}} < 2.59$ W.

40 Gb/s signal

If the output pulse width of the retiming stage is 8.25 ps (FWHM) for a 40 Gb/s signal and the same fiber parameters for the 10 Gb/s signal are used, then the dispersion length is $L_D = 2.42$ km. Then the available soliton order is $N_{\text{avail.}} < 2.03$ and the available peak power is $P_{0,\text{avail.}} < 0.162$ W. The available soliton order and peak power for a 40 Gb/s signal is significantly lower than the 10 Gb/s case and they are not acceptable. This is because the short dispersion length causes the 40 Gb/s pulse to broaden too quickly. Thus for a 40 Gb/s signal the amount of fiber dispersion should be reduced. In order to properly scale the dispersion value for a 40 Gb/s signal, the value of $N_{\text{avail.}}$ should be similar to each other [127]. Since the value of $N_{\text{avail.}}$ for a 40 Gb/s signal is nearly 16 times smaller than that for a 10 Gb/s signal, by looking at (2.61), the GVD parameter $|\beta_2|$ should be decreased by a factor of 16 to maintain the same value of $N_{\text{avail.}}$. If the dispersion of the XPM-HNLF is modified to -0.5 ps/nm/km, the available soliton order is $N_{\text{avail.}} < 32.59$ and the available peak power is $P_{0,\text{avail.}} < 2.59$ W.

2.3.2 SPM induced spectral broadening

In order to describe the SPM induced spectral broadening, the slowly varying pulse amplitude is introduced as

$$A(z, T) = \sqrt{P_0} \exp(-\alpha z/2) U(z, T), \quad (2.63)$$

where $U(z, T)$ is defined as a normalized amplitude. If we ignore the dispersion effect ($D = 0$), the pulse propagation equation for the normalized amplitude is given by [128]

$$\frac{\partial U}{\partial z} = \frac{i e^{-\alpha z}}{L_{NL}} |U|^2 U. \quad (2.64)$$

Then (2.64) can be solved and the normalized amplitude after a fiber length of L is given by

$$U(L, T) = U(0, T) \exp[i\phi_{NL}(L, T)], \quad (2.65)$$

where

$$\phi_{NL}(L, T) = |U(0, T)|^2 \frac{L_{eff}}{L_{NL}}. \quad (2.66)$$

$L_{eff} = [1 - \exp(-\alpha L)]/\alpha$ denotes the effective length that takes into account fiber loss. In (2.65), intensity dependent nonlinear phase shift is caused by SPM. If $U(z, T)$ is normalized such that $|U(0, 0)| = 1$, the maximum phase shift occurs at the center (i.e., peak) of the pulse ($T = 0$) and is given by

$$\phi_{max} = \frac{L_{eff}}{L_{NL}} = \gamma P_0 L_{eff}. \quad (2.67)$$

The time variation of the phase across the pulse implies that the instantaneous optical frequency (i.e., chirp) changes across the pulse from its central wavelength. The SPM induced frequency chirp is

$$\Delta\omega(T) = -\frac{\partial\phi_{NL}}{\partial T} \quad (2.68)$$

$$= -\frac{L_{eff}}{L_{NL}} \frac{\partial}{\partial T} |U(0, T)|^2 \quad (2.69)$$

If a Gaussian pulse is considered

$$U(0, T) = \exp\left(-\frac{T^2}{2T_0^2}\right), \quad (2.70)$$

the SPM induced chirp is given by

$$\Delta\omega(T) = \frac{2}{T_0^2} \frac{L_{eff}}{L_{NL}} T \exp\left(-\frac{T^2}{T_0^2}\right). \quad (2.71)$$

2.3.3 Offset filtering

For the suppression of the zero level, we utilize the fact that spectral broadening of the noise in the zero level is negligible compared to that in the one level. Thus by choosing an offset large enough from the data signal wavelength, noise cannot pass through the offset filter thereby suppressing noise in the zero level [64]. For the suppression of amplitude noise in the one level, the SPM induced spectral broadening should be large enough and exhibit a flat region so that power fluctuation is reduced within the passband of the offset filter. For the design of the offset filter, the filter offset and bandwidth are considered to optimize the performance.

Filter offset

By maximizing $\Delta\omega$ in (2.71), the maximum induced chirp is given by [59, Sec. 4.1.2]

$$\Delta\omega_{max} = \frac{0.86}{T_0} \phi_{max}. \quad (2.72)$$

In order to achieve the best performance for reshaping, the SPM induced spectral broadening should exhibit a spectral region that has small power fluctuation [65].

The performance of the reshaping stage is found to be good when the offset filter coincides with the outermost peak in the spectrum. The outermost peak is related to

the maximum chirp of the signal and the corresponding offset is given by

$$|\Delta\omega_{\text{off2}}| = \frac{0.86}{T_0} \phi_{\text{max}}, \quad (2.73)$$

$$|\Delta f_{\text{off2}}| = \frac{0.86}{2\pi T_0} \phi_{\text{max}}, \quad (2.74)$$

or in the wavelength domain,

$$|\Delta\lambda_{\text{off2}}| = \frac{0.86\lambda^2}{2\pi c T_0} \phi_{\text{max}}, \quad (2.75)$$

$$= \frac{0.86\lambda^2}{2\pi c T_0} \gamma P_0 L_{\text{eff}}. \quad (2.76)$$

Moreover, the required peak power to broaden the spectrum so that the outermost peak coincide with the offset filter ($\Delta\lambda_{\text{off2}}$) is

$$P_0 = \frac{2\pi c T_0}{0.86\lambda^2 \gamma L_{\text{eff}}} |\Delta\lambda_{\text{off2}}|. \quad (2.77)$$

The above equation is valid when fiber dispersion is zero. In fact, a small amount of negative dispersion is found to help obtain flat spectral broadening. When there is negative dispersion, the interplay between GVD and SPM causes the spectrum to broaden less than the zero dispersion case [70]. Then, the required peak power is larger than the right hand side of (2.77) given by

$$P_{0,\text{req.}} > \frac{2\pi c T_0}{0.86\lambda^2 \gamma L_{\text{eff}}} |\Delta\lambda_{\text{off2}}|. \quad (2.78)$$

The estimated required peak power from (2.78) is closer to the true value when the dispersion length is much larger than the fiber length ($L_D \gg L$). If the dispersion length is comparable to the fiber length, more power is needed to achieve the desired amount of spectral broadening.

Filter bandwidth

The bandwidth of the offset filter for the reshaping stage described in Sec. 2.2.4 can also be used for the reshaping stage. The bandwidth of the offset filter is determined by the desired pulse width at the output of the offset filter and is given by

$$\begin{aligned}\Delta\lambda_{FWHM} &= \frac{\lambda^2}{c} \Delta f_{FWHM} \\ &= \frac{2 \ln 2 \lambda^2}{\pi c T_{out,FWHM}},\end{aligned}\quad (2.79)$$

where $T_{out,FWHM}$ is the desired pulse width of the output signal.

Example 6

10 Gb/s signal

If we assume the output pulse width of the retiming stage is 33 ps (FWHM) and the length of the SPM-HNLF is 3 km (attenuation of 0.76 dB/km, dispersion of -8 ps/nm-km), the minimum required peak power to broaden the spectrum for $\Delta\lambda_{off2} = 0.3$ nm offset filtering is $P_{0,req.} = 0.221$ W (an average power of 18.6 dBm). The filter bandwidth that produces the output pulse width of 40 ps is 0.088 nm. Using the parameters above, the corresponding dispersion and nonlinear length are $L_D = 38.8$ km and $L_{NL} = 420$ m, respectively ($N = 9.61$).

40 Gb/s signal

For a 40 Gb/s signal with a pulse width of 8.25 ps (FWHM) and a 3 km SPM-HNLF (attenuation of 0.76 dB/km, dispersion of -0.5 ps/nm-km), the minimum required peak power to broaden the outer most peak to -0.7 nm is $P_{0,req.} = 0.129$ W (an average power of 16.3 dBm). The filter bandwidth that produces the output pulse

width of 10 ps is 0.35 nm. The corresponding dispersion and nonlinear length are $L_D = 38.7$ km and $L_{NL} = 730$ m, respectively ($N = 7.28$).

2.4 Performance measures and methodology

In order to evaluate the performance of the regenerator, accurate performance measures need to be developed. In this section, performance measures used to characterize the regenerator are described.

2.4.1 Performance Measures

Extinction ratio

One simple measure to assess the signal quality is the extinction ratio (ER), which takes the ratio of the power in the one level μ_1 to that in the zero level μ_0 within a time window

$$ER_{dB} = 10 \log_{10} \left(\frac{\mu_1}{\mu_0} \right). \quad (2.80)$$

The optical power levels are typically measured on an oscilloscope as the mean value of pulse height. ER affects the power penalty or transmission distance over which an optical signal can be reliably transmitted [129].

Power Transfer Function

The power transfer function (PTF) has been widely used in assessing the performance of a regenerator [64, 96, 130]. To obtain the PTF, the peak power of the output pulse is measured as the peak power of an input pulse is stepped over the range of

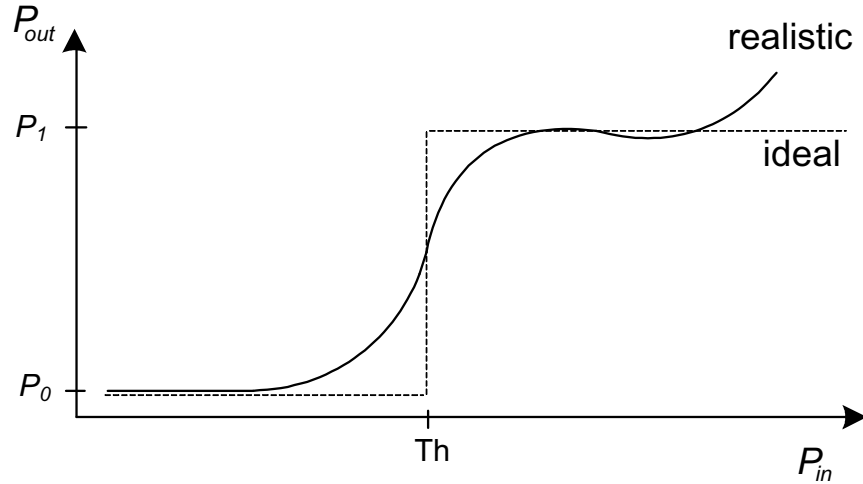


Figure 2.20: Schematic illustration of the ideal and realistic peak power transfer functions.

interest. Fig. 2.20 shows an example of ideal and realistic PTFs. The PTF indicates the effectiveness of a regenerator. An ideal regenerator has a step-like PTF so that fluctuations in the one and zero levels due to noise and signal distortion are suppressed. Although the PTF is quite useful, it does not characterize the reshaping properties of a regenerator as fully as the BER performance in a recirculating loop experiment. This is because noise is not considered when obtaining the PTF, and the signal and noise can have different PTFs [96]. In order to incorporate the impact of noise into the performance measure, the Q-factor can be used.

Q-factor

The Q-factor in dB is defined as

$$Q_{dB} = 20 \log_{10} \left(\frac{\mu_1 - \mu_0}{\sigma_1 + \sigma_0} \right), \quad (2.81)$$

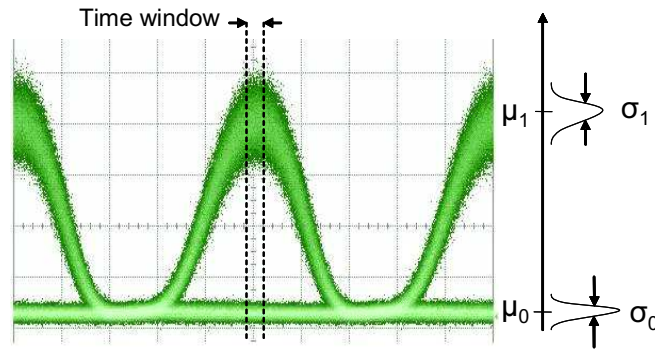


Figure 2.21: Eye diagram and power level distributions.

where μ_1 and μ_0 are the average intensities of the one and zero levels of the output optical signal, respectively. σ_1 and σ_0 are the standard deviations of the one and zero levels, respectively. Mean and standard deviation of the one and zero levels are measured over a time window located at the center of the pulse. Fig. 2.21 shows an example of eye diagram and some measures of signal qualities. The optical intensity levels are measured on an oscilloscope as the mean value of pulse height. For the measurement, the oscilloscope had an optical bandwidth of 65 GHz and an electrical bandwidth of 55 GHz.

Estimation of the BER from parameters like the Q-factor can be performed if the eye closure is due to Gaussian noise. However, for the regenerator, the Q-factor can not be used to estimate BER. Although the input noise may have a Gaussian distribution, the output noise is not Gaussian distributed due to the nonlinear transfer characteristic of the regenerator. In other words, the higher Q-factor in the regenerator may not correspond to the lower BER. Thus a more relevant performance measure is needed.

Relative standard deviation

For the regenerators based on SPM and offset filtering as reported in [64, 130], the noise in the one and zero levels have different characteristics [96]. Thus it is more accurate to separate the noise processes of the one and zero levels rather than combining them (e.g., Q-factor). In this case, relative standard deviation (RSD) can be used to isolate the noise in the one and zero levels [131]

$$RSD_1 = \sigma_1/\mu_1 \quad (2.82)$$

$$RSD_0 = \sigma_0/\mu_1. \quad (2.83)$$

After regeneration, each RSD value should be less than that of input signal to show an improvement.

Timing jitter

Timing jitter is a short term variation of the signal pulse from its ideal position. For the timing jitter measurement, an oscilloscope equipped with a precision timebase module is used to measure the RMS timing jitter. The precision timebase module provides very low intrinsic jitter which allows to measure the timing jitter as low as 200 fs. When measuring the timing jitter, the values for the rising and falling edges are averaged. From the oscilloscope, the timing jitter is typically measured as the variation of the rising edge at half maximum point in intensity. If there is amplitude fluctuation, variation of the rising edge occurs and it is included in the timing jitter measurement. Thus the amplitude noise can be interpreted as timing jitter by the oscilloscope measurement.

The other method to measure timing jitter is to use a radio frequency (RF) spectrum analyzer to measure phase noise. However, this is only possible when the input signal has a periodic pulse train (e.g., a clock signal).

Bit error ratio

One of the ultimate performance measures to assess the regenerator performance is bit error ratio (BER) given by [129]

$$BER = \frac{E(t)}{N(t)}, \quad (2.84)$$

where $E(t)$ is the number of errors that occurred over time t and $N(t)$ is the total number of bits counted in time t . BER is a statistical parameter and the reliability depends on the measurement time or the total number of bits measured. Typically, 50 to 100 error counts are acceptable but it can be time consuming for low BER measurements (e.g., a BER below 10^{-12} for single regeneration or a BER below 10^{-10} in a recirculating loop experiment).

Optical signal to noise ratio (OSNR)

Amplified spontaneous emission noise due to optical amplification is added to an optical signal as it propagates in a system. In optical communications, optical signal to noise ratio (OSNR) quantifies the degree of impairment and is defined as the ratio of a signal power to a noise power

$$OSNR_{dB} = 10 \log_{10} \frac{S}{N}, \quad (2.85)$$

where S and N are the signal power and the noise power respectively. In this thesis, the OSNR was measured with an optical spectrum analyzer (OSA) using a noise

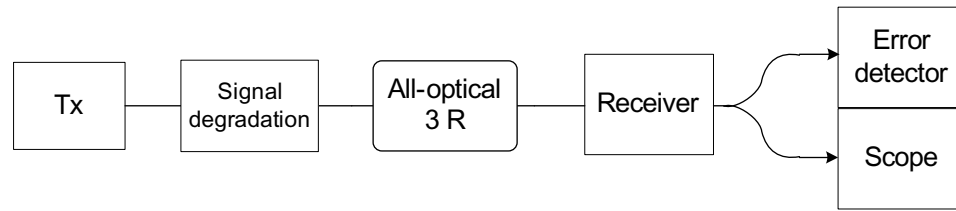


Figure 2.22: Simple block diagram of the experimental setup.

bandwidth of 0.1 nm.

2.4.2 Methodology

To experimentally evaluate the performance of the regenerator, an optical transmission system needs to be established. Fig. 2.22 shows a simple block diagram of the system setup which consists of the block of the transmitter, signal degradation, all-optical 3R, receiver, and measurement equipment. In the following, each block used for the experiment is briefly described.

Transmitter

Fig. 2.23 shows a block diagram of the transmitter. A CW laser signal is modulated by two sets of a polarization controller and a Mach-Zehnder (MZ) modulator; one for pulse carving and the other for data modulation. The first MZ modulator carves the CW signal using the electrical clock signal from a pulse pattern generator, and the second MZ modulator modulates the data bit stream using a pseudo-random bit sequence (PRBS) pattern. DC bias signals adjust the extinction ratio and duty cycle of the RZ-OOK signal. An EDFA and optical bandpass filter (OBPF) are used to

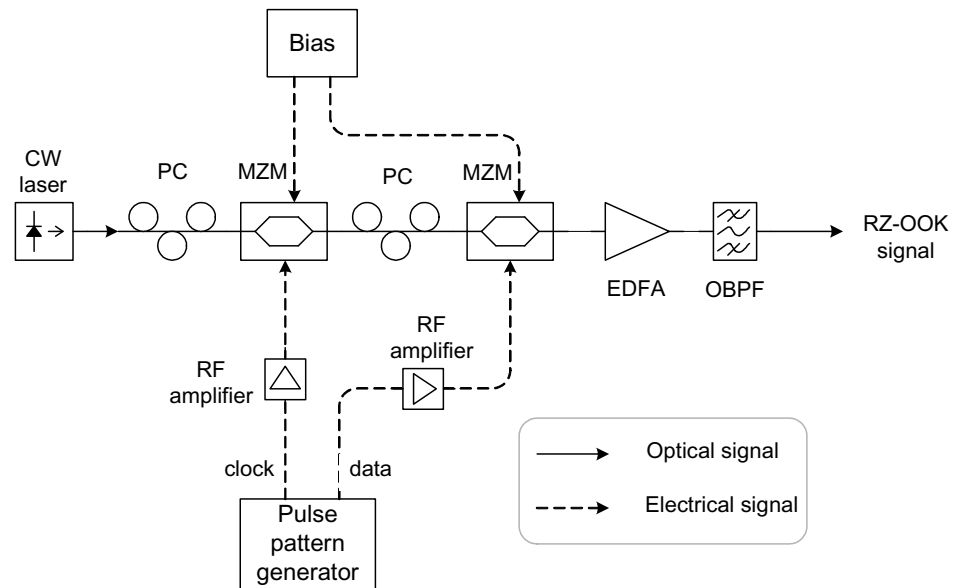


Figure 2.23: Block diagram of the transmitter; CW: continuous wave signal, PC: polarization controller, MZM: Mach-Zehnder modulator, OBPF: optical bandpass filter, RZ-OOK: return to zero on-off keyed.

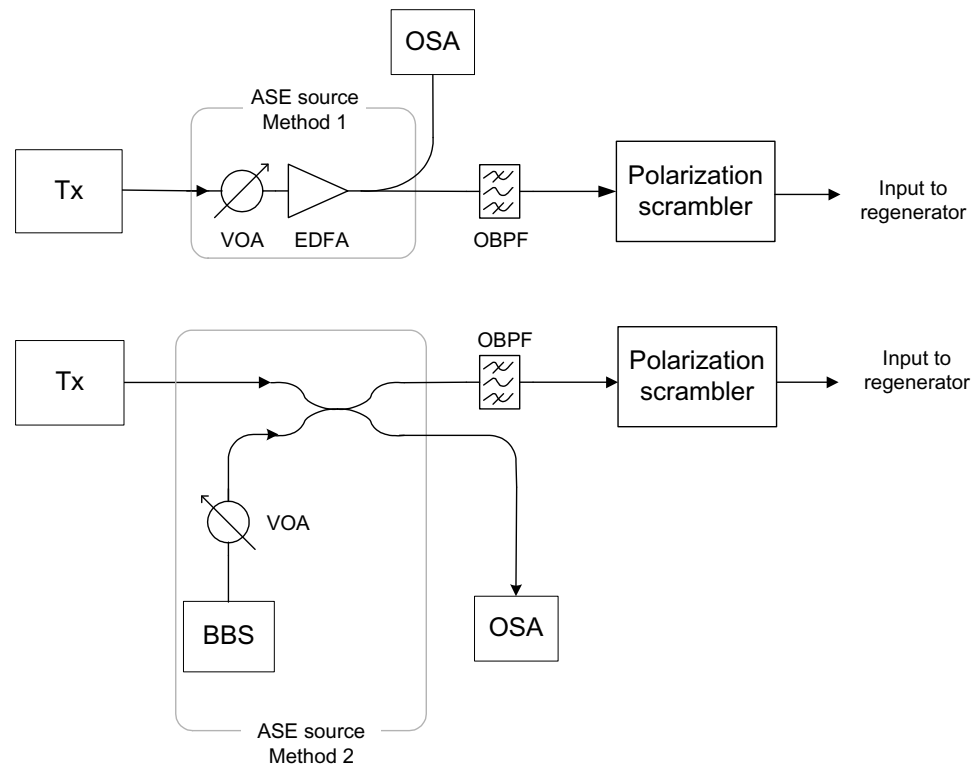


Figure 2.24: Block diagram of the signal degradation; VOA: variable optical attenuator, OBPF: optical bandpass filter, BBS: broad band source, OSA: optical spectrum analyzer.

compensate for the insertion loss caused by the optical components.

Degradation of the optical signal

Since the regenerator is designed to operate in an intermediate node of a transmission link, the input signal to the regenerator will be degraded by various impairments such as ASE noise, residual dispersion, polarization mode dispersion (PMD), etc. In order to properly evaluate the regenerator performance, the input signal should be intentionally degraded. Fig. 2.24 shows a block diagram to degrade an optical signal. There are

two ways to add ASE noise. First, a transmitted signal is attenuated by a variable optical attenuator (VOA). Then a subsequent EDFA amplifies the signal back to the same power level. Depending on the input signal power to the EDFA, OSNR is adjusted by adding different amount of ASE noise to the data signal. Although this is a simple and effective method, the output signal power tends to decrease as the attenuation of the VOA increases. Another way to add ASE noise is to employ a broad band source (BBS). A BBS can generate wideband white-noise (e.g., entire C band). Using a VOA and an optical coupler, generated noise is coupled into the clean data signal. After adding ASE noise, a portion of the signal is tapped off to monitor the OSNR using an OSA. In order to assess the dependence of the regenerator performance on the SOP of the data signal, the SOP of the data signal is scrambled by the polarization scrambler.

Pre-amplified receiver

After regeneration, a pre-amplified receiver is used to convert the received optical signal to an electrical signal. Fig. 2.25 shows a block diagram of the pre-amplified receiver. The received optical power (ROP) is adjusted by a VOA. A small portion of the signal is tapped off to monitor the ROP and the power input to the receiver. The error detector or the oscilloscope measures the various signal qualities.

Recirculating loop

The ultimate performance measure for the regenerator is the BER measurement using a recirculating loop. Fig. 2.26 shows a typical recirculating loop setup. A computer outputs control signals to control two arbitrary waveform generators (AWGs). AWG1

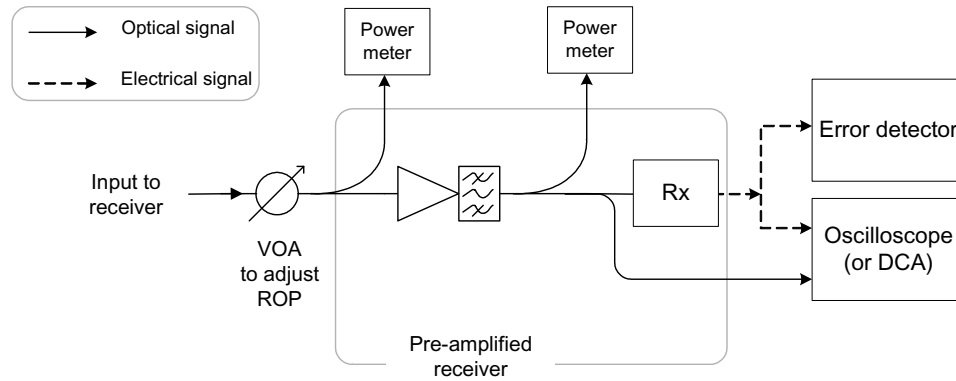


Figure 2.25: Block diagram of the pre-amplified receiver; ROP: received optical power, VOA: variable optical attenuator, Rx: receiver, DCA: digital communication analyzer.

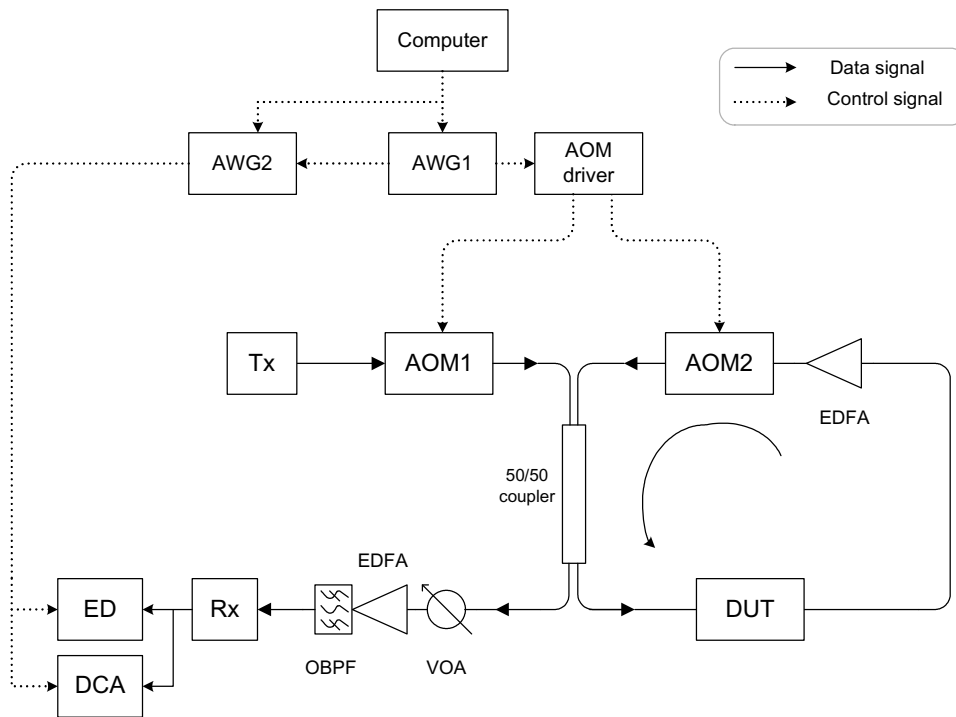


Figure 2.26: Block diagram of the recirculating loop; AWG: arbitrary waveform generator, AOM: acousto-optic modulator, DUT: device under test, Rx: receiver, ED: error detector, DCA: digital communication analyzer.

opens and closes acousto-optic modulators (AOMs) to control the loop. AWG2 is used to generate a gating signal for the instrument such as an error detector (ED) and digital communication analyzer (DCA). Loop control signals for AOMs operate as follows. To begin with, AOM1 is open to gate the transmitted signal into the loop. While AOM1 is open, AOM2 is closed until the loop is filled with the data signal. Once the loop is filled with the data signal, AOM1 is closed and at the same time, AOM2 is open. Then the data signal recirculates inside the loop. An EDFA placed in the loop compensates for the loss so that output powers of the two AOMs are same. As the signal circulates in the loop, half of the signal is split and goes into the receiver. Thus the receiver sees the data signal for all number of loops coming sequentially. AWG2 generates a gating window for the instruments to perform measurements after a desired number of loops.

2.5 Summary

In this chapter, the operating principle of an all-optical 3R regenerator has been discussed. The regenerator consists of retiming and reshaping stages which must be carefully co-designed to achieve polarization-insensitive wavelength-preserving operation. The retiming stage uses XPM induced spectral broadening and offset filtering. Polarization-insensitive retiming can be achieved by placing an offset filter in the wavelength region where the SOP dependency is minimal. Raman amplification allows polarization-insensitive retiming to be obtained with a large offset so that wavelength-preserving regeneration is possible. The reshaping stage is based on SPM induced spectral broadening and offset filtering that suppresses amplitude noise in the one and zero levels. For the evaluation of the regenerator, performance measures and methodology have been discussed.

Chapter 3

The Regenerator for a 10 Gb/s Signal

Optical regeneration is one of the key technologies to increase the reach of long-haul transmission systems. In this chapter, a wavelength-preserving polarization-insensitive all-optical 3R regenerator is demonstrated that consists of a self pulsating-distributed feedback (SP-DFB) laser for clock recovery, cross-phase modulation (XPM) in a highly nonlinear fiber (HNLF) and offset filtering for retiming, and self-phase modulation (SPM) in a HNLF and offset filtering for reshaping [132]. Under appropriate conditions, there exist wavelength regions for which an XPM broadened spectrum is polarization-insensitive [81, 133]. The retiming stage is insensitive to the state of polarization (SOP) of the input signal when the offset filter coincides with this region [65,81]. The first demonstration of this regenerator was not wavelength-preserving as the filter offsets for the retiming and reshaping stages were separately optimized. In order to preserve the wavelength, the filter offsets for the retiming and reshaping stages should be $\Delta\lambda$ and $-\Delta\lambda$, respectively. In this case, the offset $\Delta\lambda$ must be chosen carefully so that both stages yield good performance. In the reshaping stage, the

filter offset must be large enough to provide a good extinction ratio [64], and yet for the retiming stage, it is more difficult to achieve polarization-insensitive operation for a large filter offset. In addressing this, we demonstrate that the addition of Raman amplification to the retiming stage can be used to achieve polarization-insensitive re-timing with a large enough offset to permit wavelength-preserving regeneration [133]. The performance of this regenerator is assessed by degrading the quality of the input signal to a single regenerator [132]. In addition, a recirculating loop experiment is performed to demonstrate the cascadability of the regenerator [134].

In this chapter, the performance of the all-optical 3R regenerator is assessed at 10 Gb/s using a SP-DFB laser to recover the clock signal for retiming. In section 3.1, the experimental setup to evaluate the regenerator is discussed. In section 3.2, the regenerator is characterized for a 10 Gb/s signal. In section 3.3, performance of the 3R regenerator is assessed for single and cascaded regeneration, and a summary is given in section 3.4.

3.1 Experimental setup

Fig. 3.1 shows the block diagram of the regenerator for a 10 Gb/s RZ-OOK signal. In the retiming stage, a clock signal is recovered from a SP-DFB laser at 1538 nm and used as the pump signal to induce XPM on the data signal in 2 km of HNLF (nonlinearity of $10.6 \text{ W}^{-1}\text{km}^{-1}$, attenuation of 0.76 dB/km, dispersion of -0.05 ps/nm/km at 1550 nm, and dispersion slope of $0.017 \text{ ps/nm}^2/\text{km}$). The input power of the clock and data signals to the XPM-HNLF was 15.8 dBm and 13.5 dBm, respectively. By using the recovered clock signal as the pump signal, the same amount of XPM was

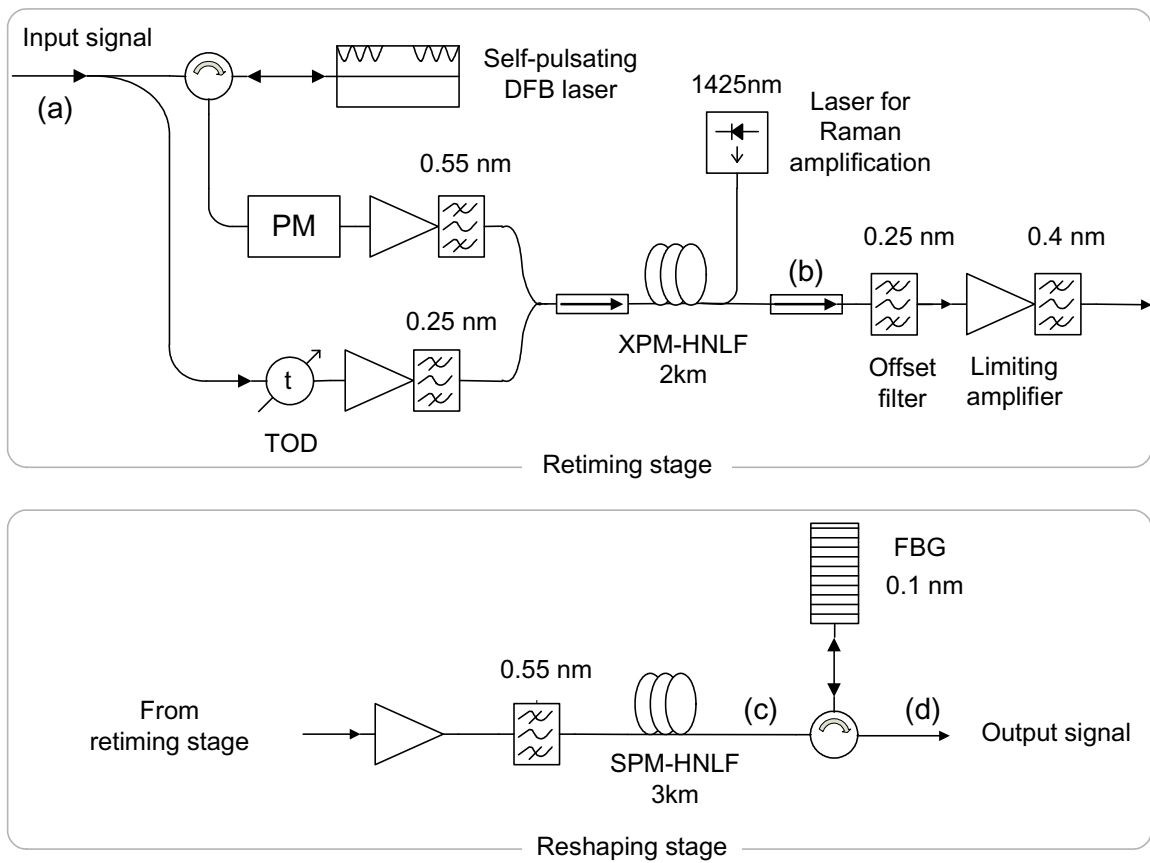


Figure 3.1: 3R regenerator setup for a 10 Gb/s signal; PM: phase modulator, TOD: tunable optical delay, XPM-HNLF: XPM inducing highly nonlinear fiber, SPM-HNLF: SPM inducing highly nonlinear fiber, FBG: fiber Bragg grating.

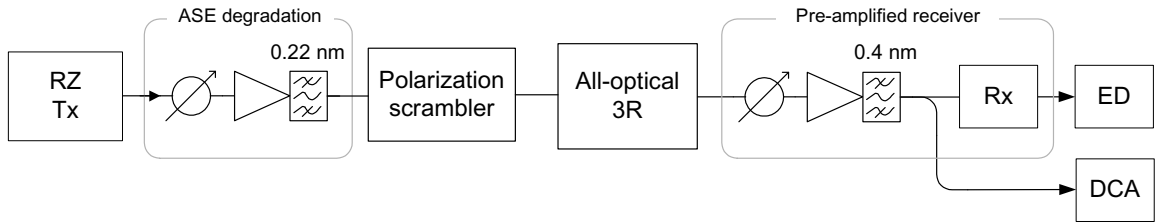


Figure 3.2: Experimental setup for a 10 Gb/s signal; RZ-Tx: RZ transmitter, Rx: receiver, ED: error detector, DCA: digital communication analyzer.

induced on input pulses of varying amplitude. A tunable optical delay (TOD) adjusts the relative time delay (~ 0 ps) between the clock and data pulses thereby balancing the timing jitter of the rising and falling edges of the retimed signal. A phase modulator driven by a 1 GHz sinusoidal signal reduces SBS of the clock signal. To increase the XPM-induced spectral broadening and achieve low-noise Raman amplification, a depolarized Raman pump signal (27.1 dBm) at 1425 nm was counter propagated in the XPM-HNLF [133]. At the output of the offset filter (0.25 nm bandwidth), a gain-saturated EDFA provided some amount of compensation for slow amplitude fluctuations due to changes in the SOP. In the reshaping stage, the retimed signal spectrum was broadened by SPM (launch power of 19.1 dBm) in 3 km of HNLF (non-linearity of $10.6 \text{ W}^{-1}\text{km}^{-1}$, attenuation of 0.76 dB/km, dispersion of -8 ps/nm/km at 1550 nm, and dispersion slope of $0.017 \text{ ps/nm}^2/\text{km}$). A fiber Bragg grating filter (0.1 nm bandwidth) centered at 1544 nm produced an output signal with the same wavelength and pulse width as the input signal.

Fig. 3.2 shows the experimental setup of the regenerator for a 10 Gb/s RZ-OOK signal ($2^{31} - 1$ PRBS) with a pulse width of 43 ps and a wavelength of 1544 nm. The OSNR of the input signal to the regenerator was adjusted by a VOA, EDFA, and OBPF. The degraded signal was applied to a polarization scrambler. At the output

of the regenerator, a pre-amplified receiver was used to convert the optical signal to an electrical signal for an ED and DCA. Table 3.1 summarizes the parameters for the regenerator.

Table 3.1: Regenerator parameters for a 10 Gb/s signal.

Retiming stage	Parameter	Value
Data signal	Wavelength	1544 nm
	Input power to XPM-HNLF	13.5 dBm
	Pulse width	43 ps (FWHM)
	PRBS pattern length	$2^{31} - 1$
Clock signal	Wavelength	1538 nm
	Input power to XPM-HNLF	15.8 dBm
Raman pump signal	Wavelength	1425 nm
	Pump power	27.1 dBm
XPM-HNLF	Length	2 km
	Nonlinearity	$10.6 \text{ W}^{-1}\text{km}^{-1}$
	Dispersion	-0.05 ps/nm/km
	Dispersion slope	$0.017 \text{ ps/nm}^2/\text{km}$
Offset filter	Offset ($\Delta\lambda_{\text{off1}}$)	-0.3 nm
	Bandwidth	0.25 nm
Reshaping stage	Parameter	Value
Data signal	Wavelength	1543.7 nm
	Input power to SPM-HNLF	19.1 dBm
SPM-HNLF	Length	3km
	Nonlinearity	$10.6 \text{ W}^{-1}\text{km}^{-1}$
	Dispersion	-8 ps/nm/km
	Dispersion slope	$0.017 \text{ ps/nm}^2/\text{km}$
Offset filter	Offset ($\Delta\lambda_{\text{off2}}$)	0.3 nm
	Bandwidth	0.1 nm

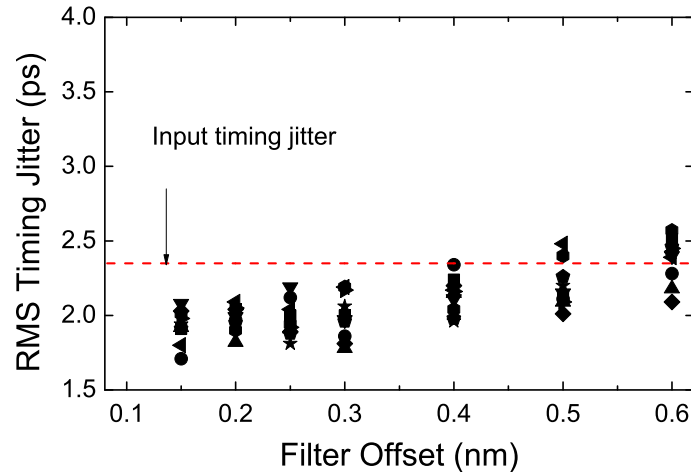


Figure 3.3: Measured filter offset versus timing jitter for the retiming stage only.

3.2 Characterization of the regenerator

To illustrate the optimum filter offset when only the retiming stage is considered, Fig. 2.17 is revisited which plots the timing jitter of both the rising and falling edges with 5 different SOPs. As shown in Fig. 3.3, the optimum filter offset is in the range of 0.15 - 0.2 nm where the timing jitter is minimum for all SOPs. As the filter offset is increased, the timing jitter starts to increase. For filter offsets larger than 0.4 nm, there exist some SOPs for which the output signal timing jitter is worse than the input signal timing jitter.

Fig. 3.4 shows the dependence of the output peak power on the input peak power to the SPM-HNLF in the reshaping stage with different filter offsets. These results can be considered as the power transfer function (PTF) of the reshaping stage only. As the filter offset was varied from 0.3 nm to 0.6 nm, the PTF exhibits different shapes.

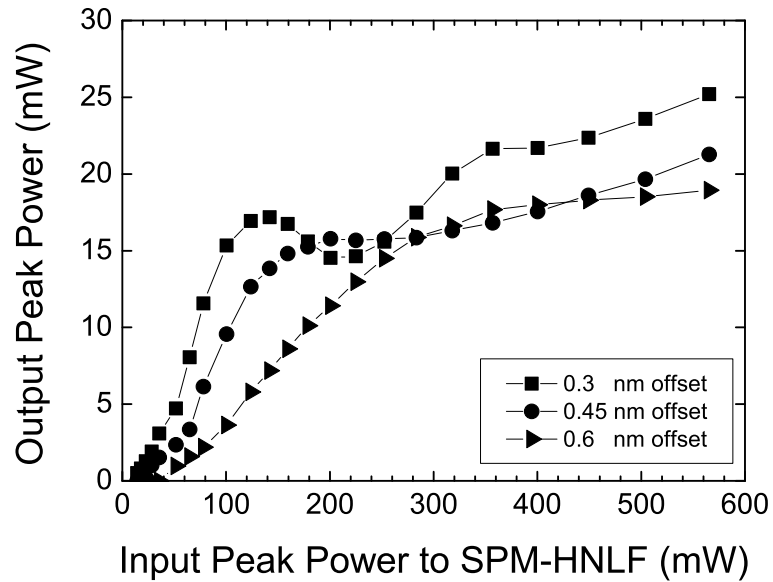


Figure 3.4: Power transfer function of the reshaping stage.

In general, as the filter offset is increased, the noise in the zero level is more effectively suppressed. However the PTFs with different offsets exhibit different shapes for the one level. If only the reshaping stage is used (i.e., 2R), based on the PTF, a 0.45 nm offset seems to be a good choice as the corresponding PTF is closest to the ideal step-like PTF.

Reasoning from Figs. 3.3 and 3.4, it can be concluded that the optimum filter offsets for the retiming and reshaping stages are not identical. Therefore, in order to achieve wavelength-preserving regeneration, the retiming and reshaping stages need to be carefully co-designed so that both stages perform well. In general, the retiming stage is more difficult to obtain a good performance.

In order to find an optimum offset for wavelength-preserving operation, the dependence of the BER on the threshold level in the ED is measured for the regenerated signal with different filter offsets in the retiming stage ($\Delta\lambda_{\text{off}1} = -0.2, -0.3$ and -0.4

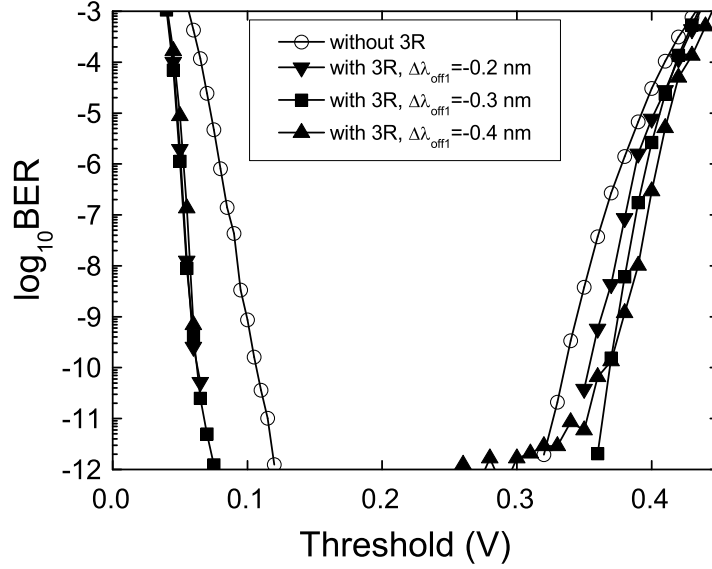


Figure 3.5: BER versus threshold with different filter offsets.

nm). The corresponding filter offset in the reshaping stage was $\Delta\lambda_{\text{off}2} = -\Delta\lambda_{\text{off}1}$. Fig. 3.5 shows the result with a ROP of -15 dBm. The ROP was chosen so that the receiver noise had a negligible effect. The input signal to the regenerator had an OSNR of 23 dB (a noise bandwidth of 0.1 nm) and a scrambled SOP (a scan rate of 285 deg/sec). The noise in the zero level is suppressed for all offsets while an offset of $\Delta\lambda_{\text{off}1} = -0.3$ nm most effectively suppresses noise for the one level. The offset $\Delta\lambda_{\text{off}1} = -0.3$ nm in the retiming stage was used to obtain the results that follow.

Fig. 3.6 shows optical spectra at several locations in the regenerator with a resolution bandwidth of 0.06 nm (refer to Fig. 3.1). When the optical spectrum was measured, a clean input signal was used (OSNR of 37 dB/0.1 nm). Fig. 3.6(a) shows the spectrum of the input data signal and Fig. 3.6(b) shows the XPM broadened data signal spectra for different SOPs of the input signal. After the XPM-HNLF, a

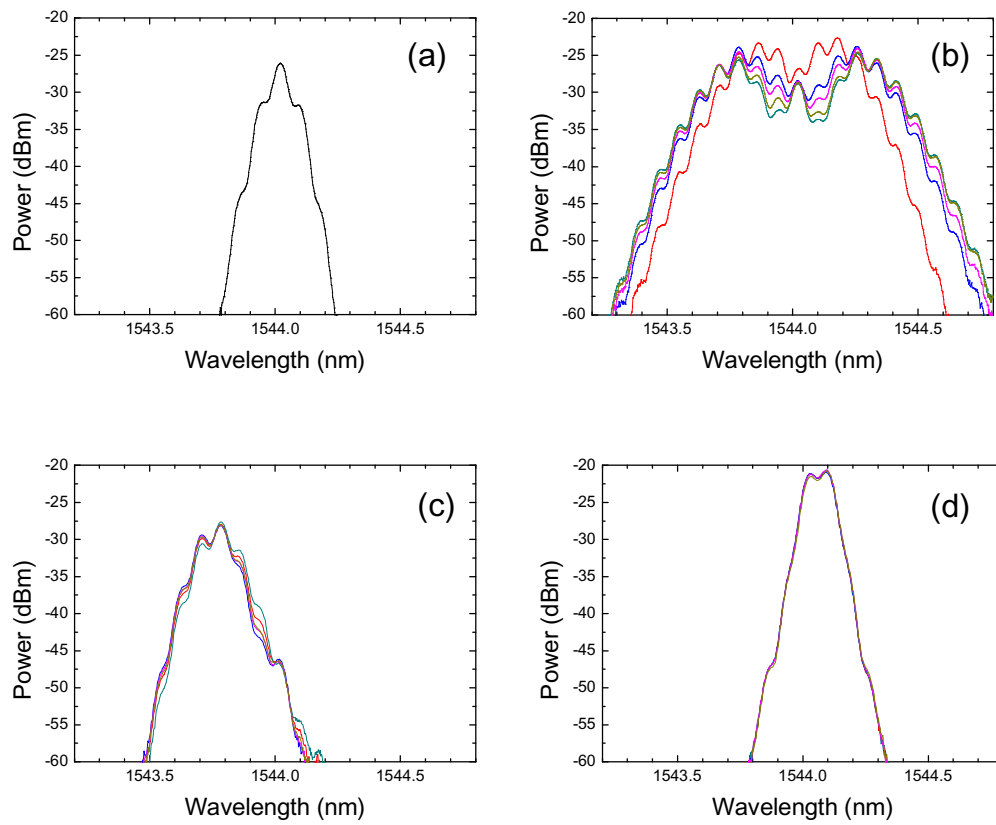


Figure 3.6: Optical spectra at several locations in the regenerator; (a) input signal, (b) after XPM-HNLF, (c) after retiming, (d) after reshaping.

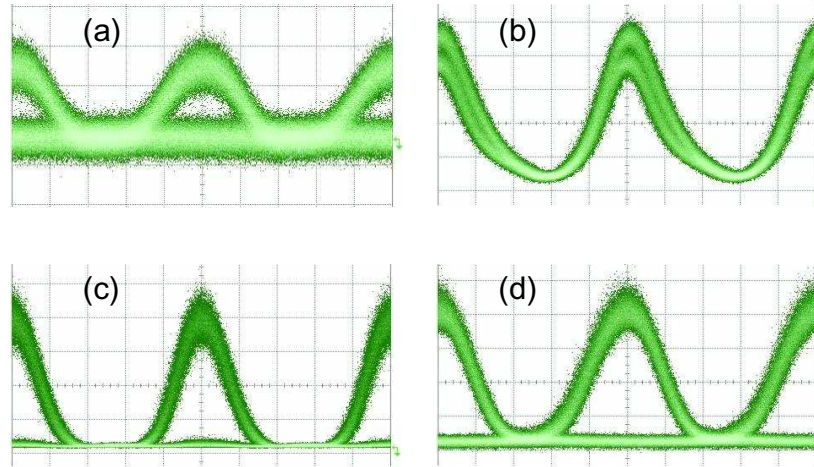


Figure 3.7: Eye diagrams at several locations in the regenerator; (a) input signal, (b) after XPM-HNLF, (c) after retiming, (d) after reshaping (time base = 20 ps/div).

large dependence of the data signal spectra on the input signal SOP is observed. The polarization independent wavelength can be found at ± 0.2 nm offset. Fig. 3.6(c) shows the data signal spectra after the retiming stage with a filter offset of -0.3 nm. The dependence on the input signal SOP is reduced after the offset filter. Fig. 3.6(d) shows the spectra after the reshaping stage. The output wavelength is the same as the input wavelength and the dependence on the input signal SOP is significantly reduced. Fig. 3.7 shows the eye diagrams for an input signal OSNR of 16 dB. As will be shown later (in Fig. 3.12), the input signal OSNR needs to be over 16 dB in order for the regenerator to operate in the error free region ($\text{BER} < 10^{-12}$).

Fig. 3.8 shows the RMS timing jitter after the retiming and reshaping stages. When the input signal timing jitter is larger than 2.3 ps, the regenerator reduces the output signal timing jitter. It is notable that when the input signal timing jitter is larger than 3 ps, the timing jitter of the signal after the reshaping stage is smaller

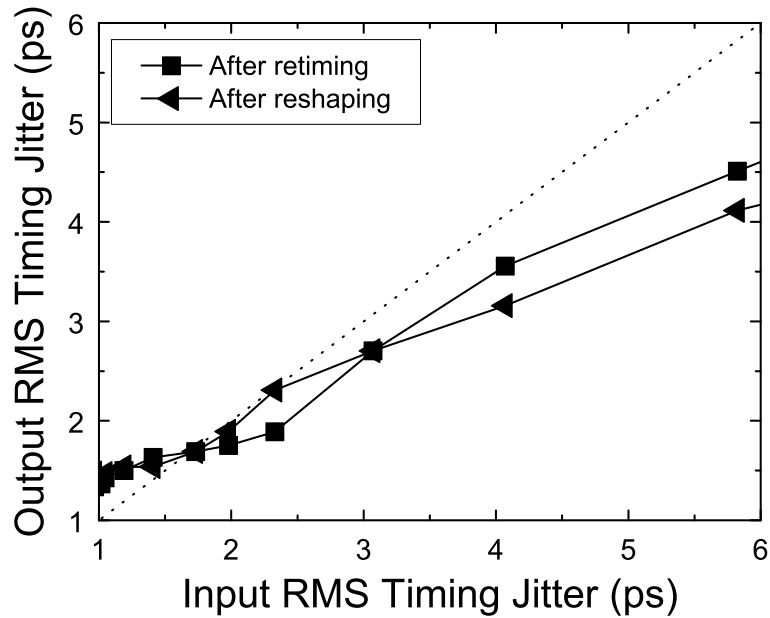


Figure 3.8: Output versus input RMS timing jitter after retiming and reshaping with SOP scrambling.

than that after the retiming stage. In general, the reshaping stage does not reduce timing jitter. The measured timing jitter from the oscilloscope is a combined effect of both the timing jitter and amplitude noise. Since there exists amplitude noise after the retiming stage, the measured timing jitter includes the impact of the amplitude noise as well. (Although it is not the real timing jitter, the oscilloscope can not separate them.) Therefore, after the reshaping stage has suppressed the amplitude noise, the measured timing jitter is lower than that of the retiming stage.

Fig. 3.9 shows the dependence of the BER on the threshold level in the error detector for the output signal after the retiming and reshaping stages. The offset for the retiming stage $\Delta\lambda_{\text{off}1}$ and the ROP were -0.3 nm and -15 dBm, respectively. The input signal to the regenerator had an OSNR of 23 dB (a noise bandwidth of 0.1 nm) and a scrambled SOP. For the purpose of illustration, the OSNR value is

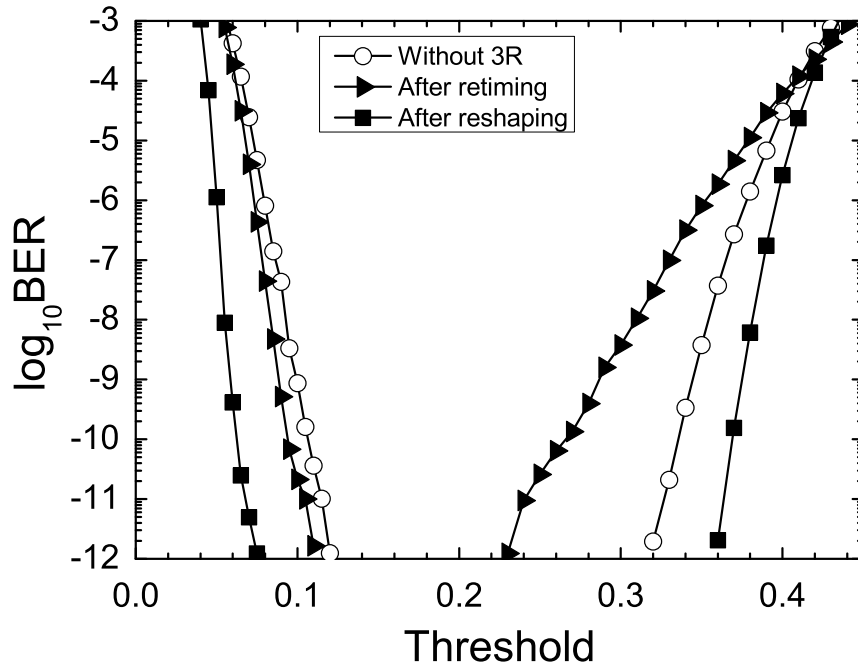


Figure 3.9: BER versus threshold with $\Delta\lambda_{\text{off1}} = -0.3\text{nm}$.

chosen so that the input signal has some amount of noise to show the improvement obtained by the regenerator. (If there is too little noise, the regenerator does not improve the performance or if there is too much noise, an error floor will occur.) The amplitude noise in the zero level is slightly reduced after the retiming stage and is further suppressed after the reshaping stage. The amplitude noise in the one level is increased after the retiming stage due to the SOP dependent slow power fluctuation. However, it is small enough for the reshaping stage to effectively suppress the amplitude noise and the overall BER curve is improved.

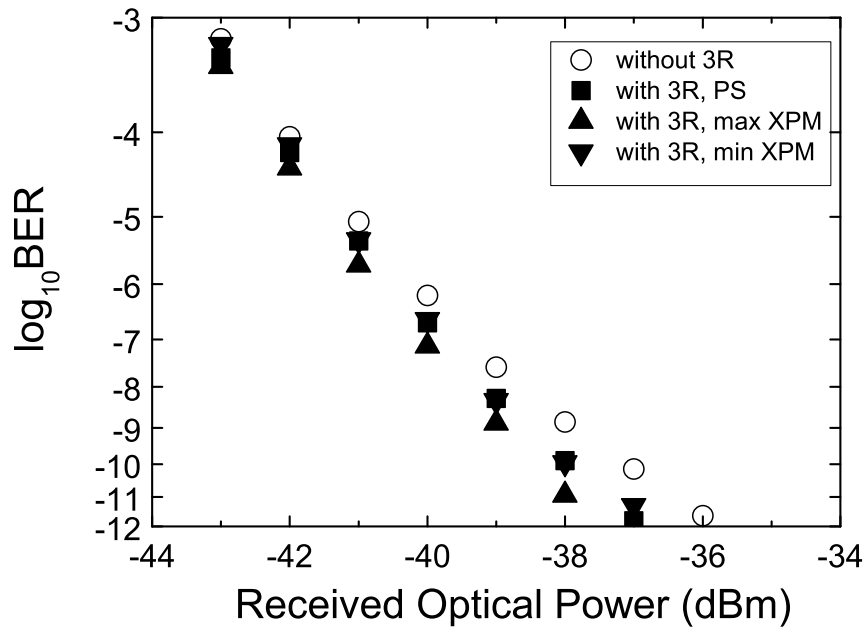


Figure 3.10: Dependence of the BER on the ROP at input signal OSNR = 20 dB.

3.3 Performance of the 3R regenerator

In this section the performance of the 3R regenerator is investigated. Throughout the experiment, the offset for the retiming stage was $\Delta\lambda_{\text{off}1} = -0.3$ nm and the SOP of the input signal was scrambled (at a scan rate of 280 deg/sec). The performance of the regenerator was evaluated for single regeneration and cascaded regeneration using a recirculating loop.

3.3.1 Single regeneration

The dependence of the BER on the ROP for an input signal OSNR of 20 dB is shown in Fig. 3.10. For comparison, BER curves for two different fixed SOPs are also shown; SOPs with maximum and minimum spectral broadening after the XPM-HNLF.

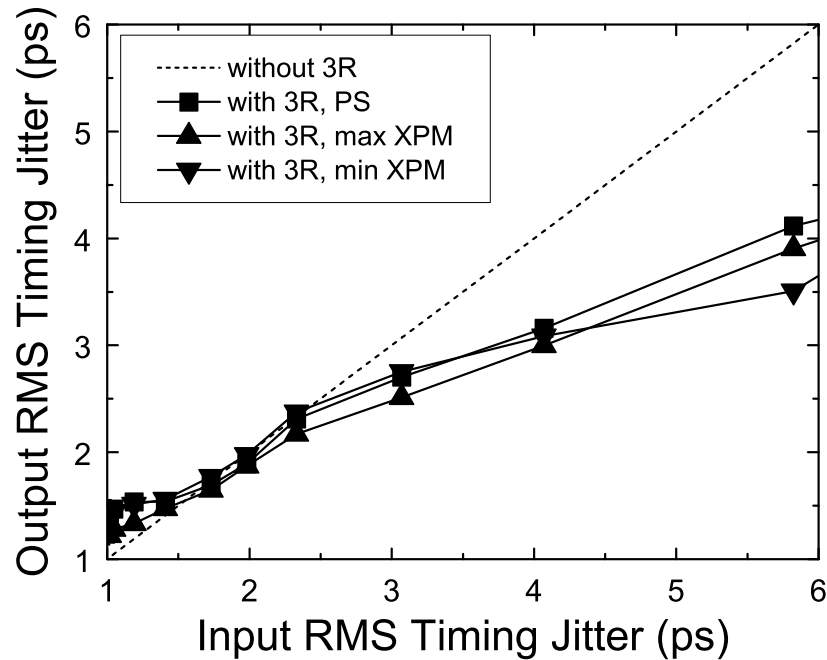


Figure 3.11: Output versus input timing jitter with a scrambled SOP and two fixed SOPs.

When the spectral broadening is minimum, it corresponds to the SOP with the worst BER. As shown in Fig. 3.10, the regenerator is seen to be polarization insensitive with the scrambled SOP. A slight improvement in the BER was observed with the regenerator compared to without regeneration. In general, the regenerator does not correct previously occurred bit errors. One reason to observe the improved BER is that the output signal from the regenerator has a different pulse shape which could be better matched to the receiver characteristics. Another reason is due to the low ROP used to measure the BER. Since the ROP is very low, receiver noise is subsequently added to the received signal. Since the regenerator has cleaned up noise, the regenerated signal is more resilient to the subsequent noise and shows improvement.

Fig. 3.11 shows the output versus input signal RMS timing jitter for a scrambled

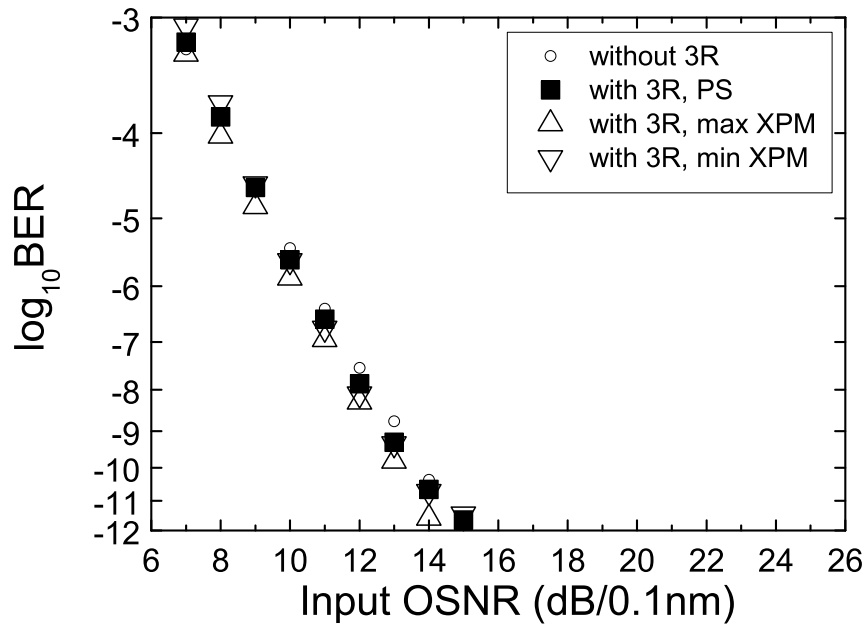


Figure 3.12: Dependence of the BER on the input signal OSNR (ROP=-15dBm).

SOP and two fixed SOPs. The timing jitter was measured using a sampling oscilloscope with a precision timebase. The regenerator is seen to be polarization-insensitive and reduces the timing jitter when the input timing jitter is larger than 2.3 ps.

Fig. 3.12 shows the dependence of the BER on the input signal OSNR with a ROP of -15 dBm. For the ROP of -15 dBm, the impact of the receiver noise on the BER is negligible and the BER performance is dominated by the properties of the regenerator. For comparison, results for two fixed SOPs are also shown corresponding to maximum and minimum spectral broadening in the retiming stage. The regenerator is seen to be polarization insensitive. Compared to the result without regeneration, it can be concluded that the regenerator does not cause a BER penalty while it suppresses amplitude noise and timing jitter.

Although Fig. 3.12 shows that the regenerator does not cause a BER penalty, it is

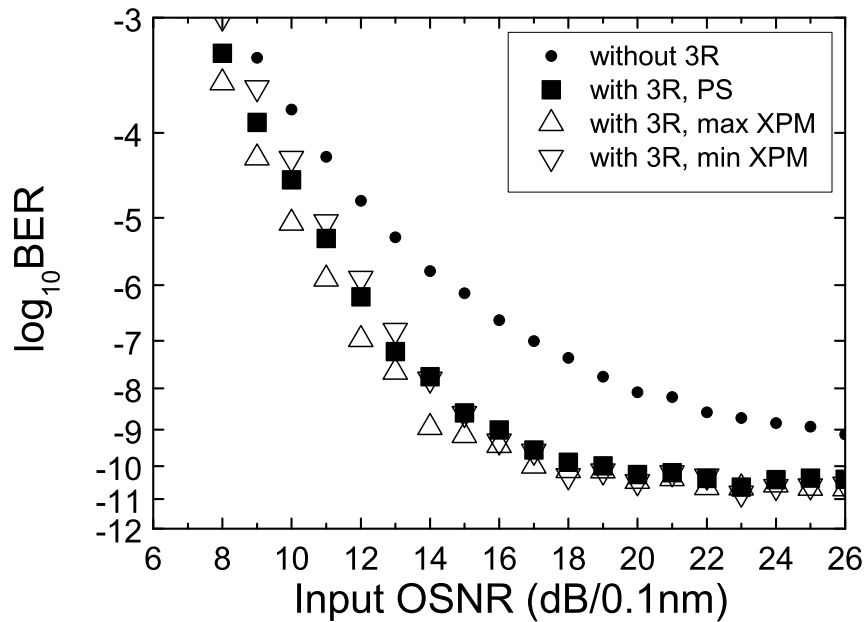


Figure 3.13: Dependence of the BER on the input signal OSNR (ROP=-38dBm).

not clear how much improvement it can offer. In order to show this, subsequent noise or distortion can be added after regeneration. This will emulate further signal degradation as if the regenerator was operated in an intermediate node in the transmission link. (This is where the regenerator is designed to operate in a practical system.) One way to add subsequent noise after regeneration is to intentionally reduce the ROP to the pre-amplified receiver. Then the ASE noise will be added by the pre-amplifier. Fig. 3.13 shows the BER curves with a ROP of -38 dBm. In this case, the receiver noise affects the performance and emulates further signal degradation that a regenerated signal would incur in a practical system. Since the regenerator has cleaned up noise in the previously degraded signal, the regenerated signal is more resilient against the subsequent noise. The transformation of the noise by the regenerator yields an improvement in the BER when the subsequent noise is not negligible. The bit error

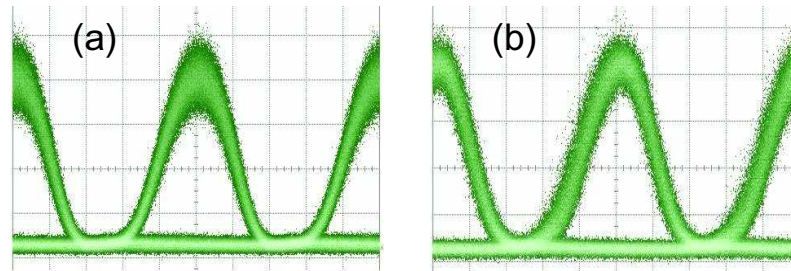


Figure 3.14: Eye diagrams for input signal OSNR of 18 dB and a scrambled SOP; (a) without 3R, (b) with 3R (time base = 20 ps/div).

floors are due to the weak input signal to the receiver. Fig. 3.14 shows sample eye diagrams with and without the regenerator for an input signal OSNR of 18 dB with a scrambled SOP.

3.3.2 Recirculating loop experiment

Since a regenerator is designed to operate on a span to reduce the impact of noise, residual dispersion, and distortion that accumulate from repeated amplification and dispersion compensation, it should be cascable to operate in a long haul transmission system. The best way to test this requirement in the lab is to perform a recirculating loop experiment. In this section, we investigate the performance of the regenerator utilizing a recirculating loop to evaluate the cascability of the regenerator.

Regenerator in the recirculating loop

Fig. 3.15 shows the experimental setup for a recirculating loop. The 10 Gb/s RZ-OOK signal ($2^{31} - 1$ PRBS) with a pulse width of 43 ps and a wavelength of 1544 nm was

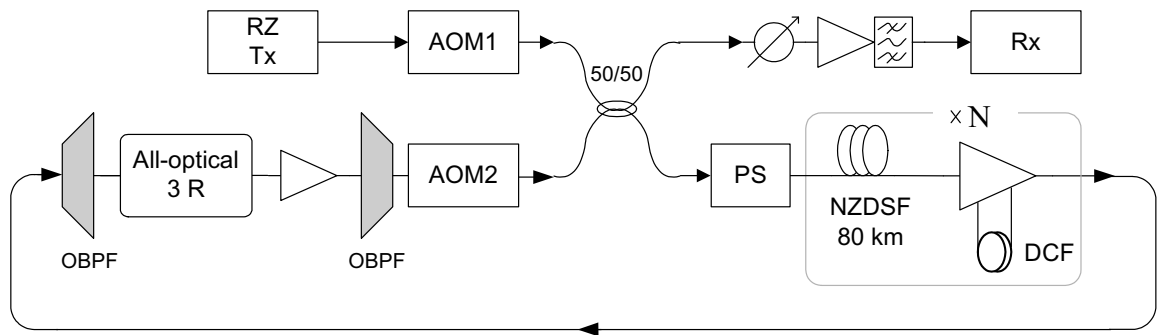


Figure 3.15: Experimental setup of the recirculating loop; RZ Tx: RZ transmitter, AOM: acousto-optic modulator, PS: polarization scrambler, NZDSF: non-zero dispersion shifted fiber, DCF: dispersion compensating fiber, OBPF: optical bandpass filter.

gated into a recirculating loop via an AOM1. In the recirculating loop, a polarization scrambler was used to scramble the SOP of the data signal. The dispersion managed transmission span consisted of 80 km of non-zero dispersion-shifted fiber (NZDSF) (attenuation of 0.2 dB/km and dispersion of 4.4 ps/nm/km at 1550 nm), dispersion compensating fiber (DCF) (total loss of 2.95 dB and total dispersion of -364 ps/nm at 1550 nm), and a 2-stage EDFA. The dispersion map was not optimized. The input power to the NZDSF was 1 dBm. This transmission span was repeated N times ($N = 1, 2, \text{ and } 3$) in the loop to evaluate the performance for regenerator spacings of 80 km, 160 km, and 240 km, respectively. The residual dispersions of the transmission span were 3.84, -5.84, and -21.54 ps/nm for 80 km, 160, and 240 km regenerator spacings, respectively. At the input to the regenerator, an OBPF replaced a demultiplexer that would be used in a practical WDM system to select a desired channel and reduce out-of-band noise. After regeneration, an additional EDFA and OBPF compensated for the loss of the AOM2 and 50/50 coupler. A pre-amplified receiver was employed to receive the signal for the ED and DCA. Table 3.2 summarizes the parameters for

Table 3.2: Parameters for the recirculating loop experiment for a 10 Gb/s signal.

Component	Parameter	Value
Non-zero dispersion shifted fiber	Length	80 km
	Attenuation	0.2 dB/km
	Dispersion	4.4 ps/nm/km at 1550 nm
Dispersion compensating fiber	Total loss	2.95 dB
	Total dispersion	-363 ps/nm at 1550 nm
EDFA	Launch power	1 dBm
Polarization scrambler	scan rate	580 deg/sec
Optical filter	Center wavelength	1544 nm
	Bandwidth	0.4 nm

the recirculating loop experiment.

Fig. 3.16 shows the Q-factor (measured with a sampling oscilloscope) as a function of distance for regenerator spacings of 80, 160 and 240 km. Without the retiming and reshaping stages (1R), the Q-factor degrades quickly (below 15 dB after 1000 km). With 3R regeneration, the Q-factor was maintained over 20 dB for up to 1 million km transmission for all three regenerator spacings. However, for such long distances, the time required to measure the Q-factor limits the number of sample points and leads to a large variation in repeated measurements (~ 2 dB).

Fig. 3.17 shows the eye diagrams for 1R regeneration with the regenerator spacings of 80 km, 160 km, and 240 km. For a 10 Gb/s signal, the degradation is due to pulse distortion and ASE noise accumulation. The pulse broadening is caused by residual dispersion. Slightly different eye diagrams between different regenerator spacings are seen in the figure (e.g., 10 loops for 80 km regenerator spacing and 5 loops for 160 km regenerator spacing). It is mainly because actual NZDSFs and DCFs used for

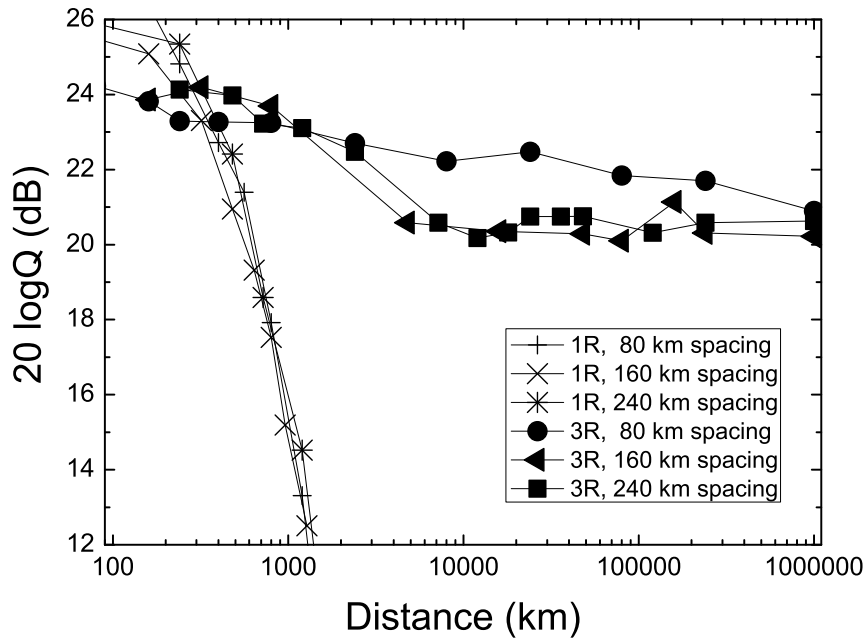


Figure 3.16: Dependence of the Q-factor on the transmission distance with different regenerator spacings.

different regenerator spacings have slightly different properties (i.e., the length of the NZDSF and total dispersion of the DCF are slightly different for each span).

Fig. 3.18 shows the dependence of the BER on the ROP for a regenerator spacing of 80 km. With 1R regeneration after 8 loops (640 km), a power penalty of 5 dB for a BER of 10^{-9} is obtained as compared to the back-to-back case. The penalty is due to the residual dispersion induced signal distortion and ASE noise accumulation. With 3R regeneration after 1,000 loops (80,000 km), a power penalty of about 1.8 dB is obtained as compared to the back-to-back case. When the signal propagates more than 3,000 loops (240,000 km), a BER floor is observed. The bit error floor is $2 \cdot 10^{-8}$ for the transmission of 1 million km. We attribute these error floors to the retiming stage as the SP-DFB laser becomes unstable for a large number of loops due

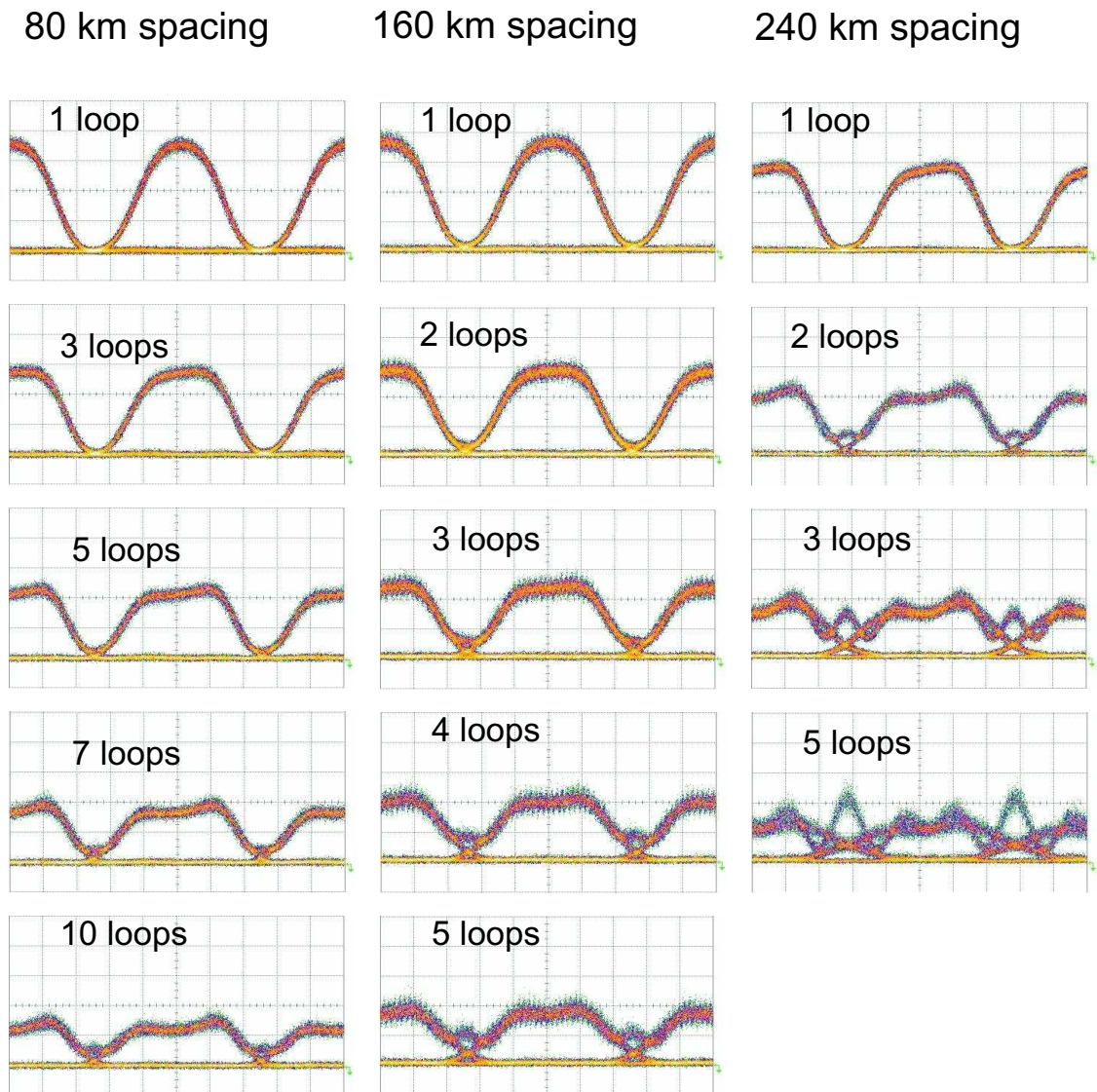


Figure 3.17: Eye diagrams for 1R regeneration with different regenerator spacings (time base = 20 ps/div).

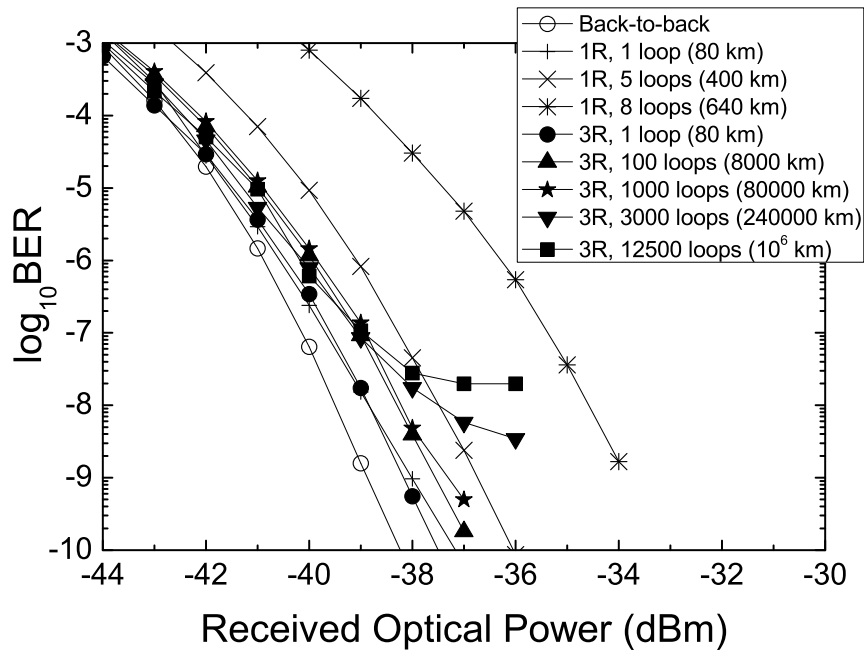


Figure 3.18: Dependence of the BER on the ROP with 80 km regenerator spacing.

to transient regions at the beginning of each loop. For long distances, the results for the Q-factor and BER are not consistent.

Fig. 3.19 shows the BER as a function of the ROP for a regenerator spacing of 160 km. With 1R regeneration after 5 loops (800 km), a power penalty of 4.5 dB is obtained. With 3R regeneration after 100 loops (16,000 km), the power penalty is about 0.6 dB compared to the back-to-back case for a BER of 10^{-9} . A BER floor occurs after 500 loops (80,000 km). One might note that with 3R regeneration, the results with 160 km regenerator spacing are slightly better than that with 80 km regenerator spacing. This is believed to be due to measurement errors. If the exactly same conditions are maintained, the regenerator performance will degrade with the increase of the regenerator spacing as will be shown in the later result (refer to Fig. 3.27).

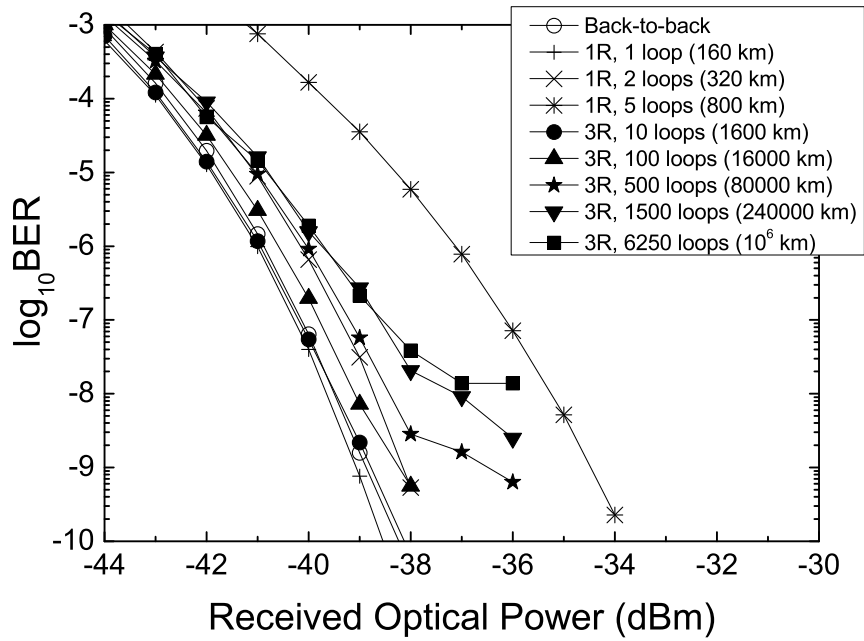


Figure 3.19: Dependence of the BER on the ROP with 160 km regenerator spacing.

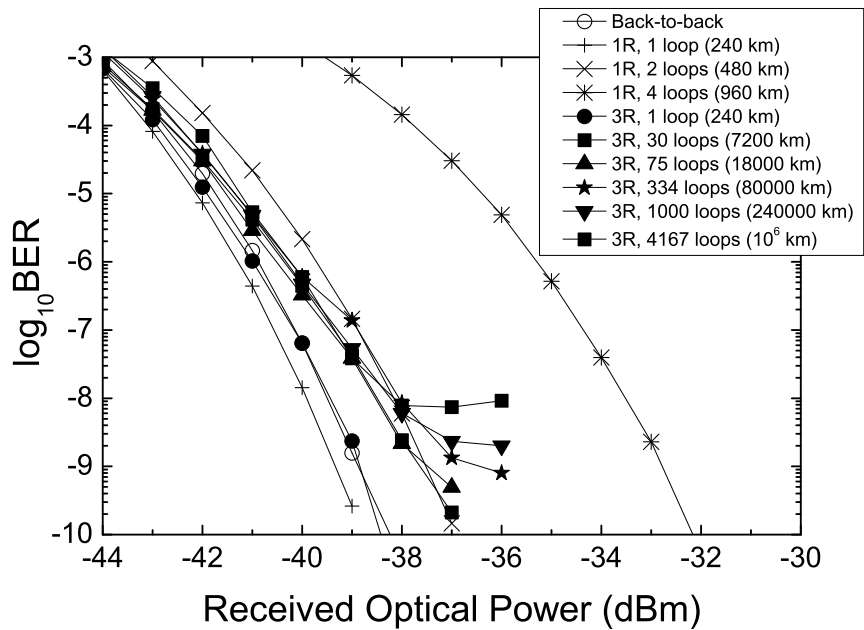


Figure 3.20: Dependence of the BER on the ROP with 240 km regenerator spacing.

Similarly, Fig. 3.20 shows the dependence of the BER on the ROP for a regenerator spacing of 240 km. With 1R regeneration after 4 loops (960 km), a power penalty of 6 dB is obtained. It is notable that, with 1R regeneration, a negative power penalty is observed for 1 loop due to the pulse broadening caused by residual dispersion. With 3R regeneration after 75 loops (18,000 km), the power penalty is about 1.6 dB compared to the back-to-back case for a BER of 10^{-9} .

Fig. 3.21 shows the eye diagrams for 3R regeneration with the regenerator spacings of 80 km, 160 km, and 240 km. For a large number of loops, the acquired sample points are limited due to the large amount of time needed to capture the eye diagram (e.g., it took around 4 hours to obtain the eye diagrams for 1 million km).

Fig. 3.22 and Fig. 3.23 show the dependence of the BER on the ROP with different regenerator spacings over 7,200 km and 80,000 km, respectively. After 7,200 km transmission as shown in Fig. 3.22, the BER curves with all three regenerator spacings do not show any sign of a BER floor. After 80,000 km transmission, as shown in Fig. 3.23, the sign of BER floors are observed for 160 km and 240 km spacings. This suggests that if the transmission distance is within a range of practical interest (8,000 - 10,000 km), the regenerator spacing can be longer than 240 km. However we were not able to perform experiments with a larger spacing due to limitations in the available equipment.

Regenerator outside the loop

From a practical point of view, it is desired to operate the regenerator with the regenerator spacing longer than 320 km (4 spans). In order to estimate how far the signal may be transmitted before regeneration, we placed the regenerator outside the loop

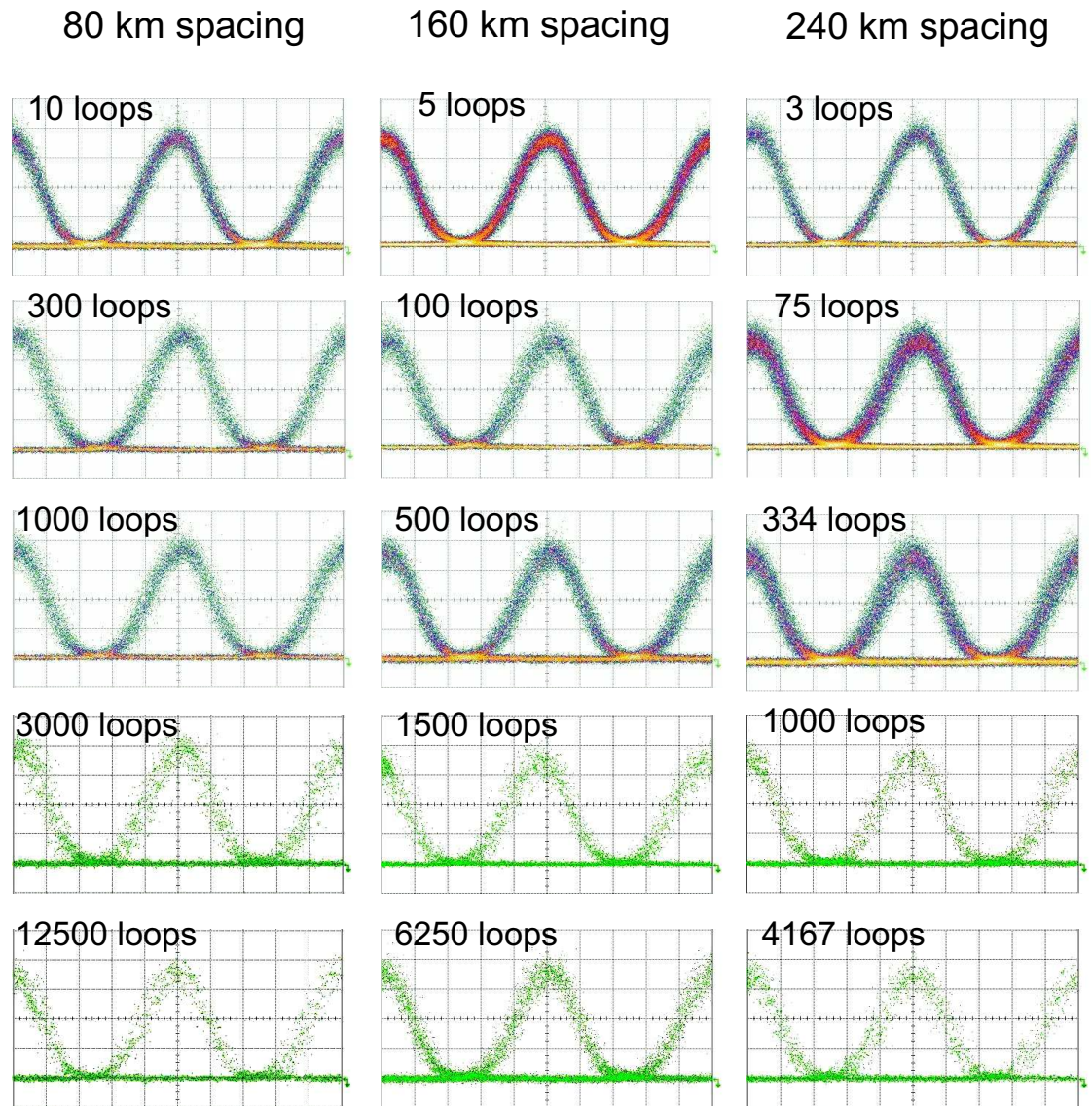


Figure 3.21: Eye diagrams for 3R regeneration with different regenerator spacings (time base = 20 ps/div).

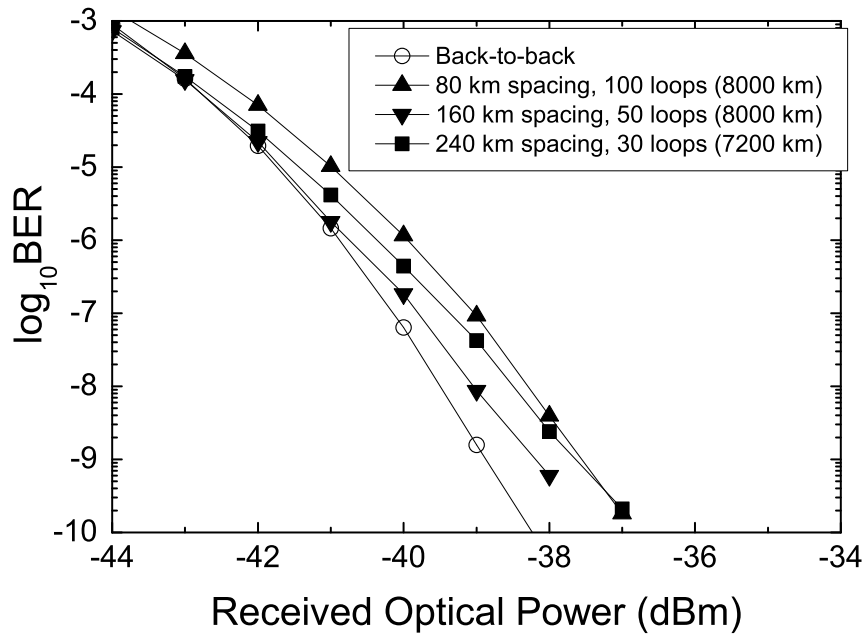


Figure 3.22: Dependence of the BER on the ROP after 7,200 km transmission with different regenerator spacings.

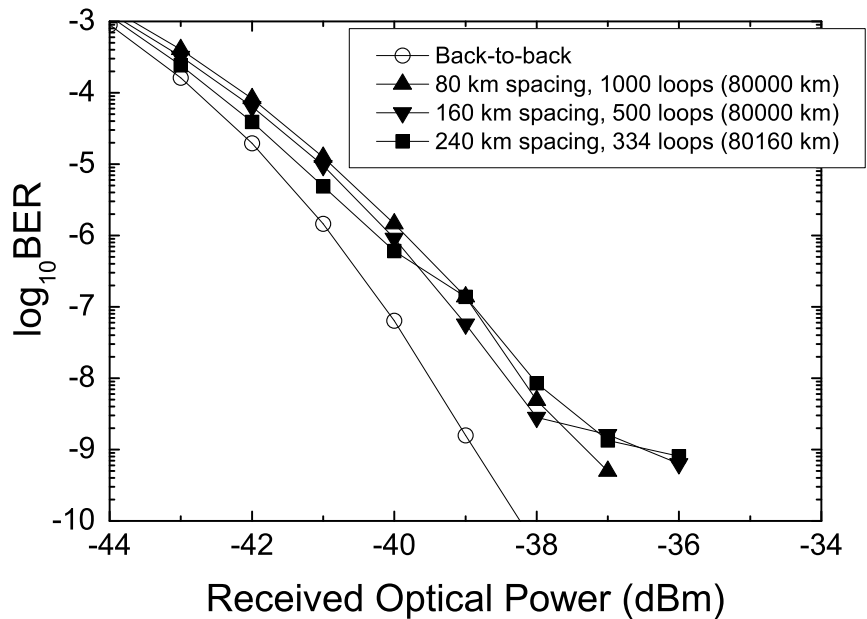


Figure 3.23: Dependence of the BER on the ROP after 80,000 km transmission with different regenerator spacings.

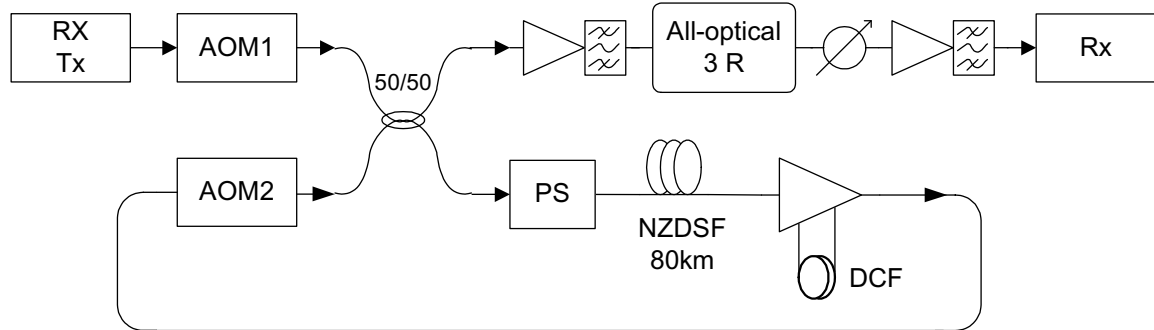


Figure 3.24: Experimental setup with the regenerator outside the loop.

and regenerated the signal just before the receiver. In this way, we could transmit the signal an arbitrarily long distance before the signal is regenerated.

Fig. 3.24 shows the setup to further investigate the transmission length before regeneration. The loop consists of a polarization scrambler, 80 km of NZDSF, EDFA, and DCF. The regenerator is placed right before the pre-amplified receiver. Thus the signal was first transmitted a number of loops and then applied to the regenerator.

Fig. 3.25 shows the dependence of the Q-factor on the transmission distance before the signal is regenerated. (Q-factor is measured from a sampling oscilloscope.) The Q-factor is plotted with and without the regenerator. When the regenerator was not used, the Q-factor constantly reduced as the transmission distance increased. With the regenerator, the Q-factor improvement is obtained for all the distances except for 80 km (1 loop). With the regenerator for up to 6 loops (480 km), the Q-factor is over 21.5 dB and it starts to degrade quickly beyond 6 loops.

Fig. 3.26 shows the dependence of the RMS timing jitter on the transmission distance before regeneration. (Timing jitter is measured from the sampling oscilloscope.) For comparison, the timing jitter of the recovered clock signal is also shown. The timing jitter of the regenerated signal is below 2.7 ps for up to 6 loops and starts

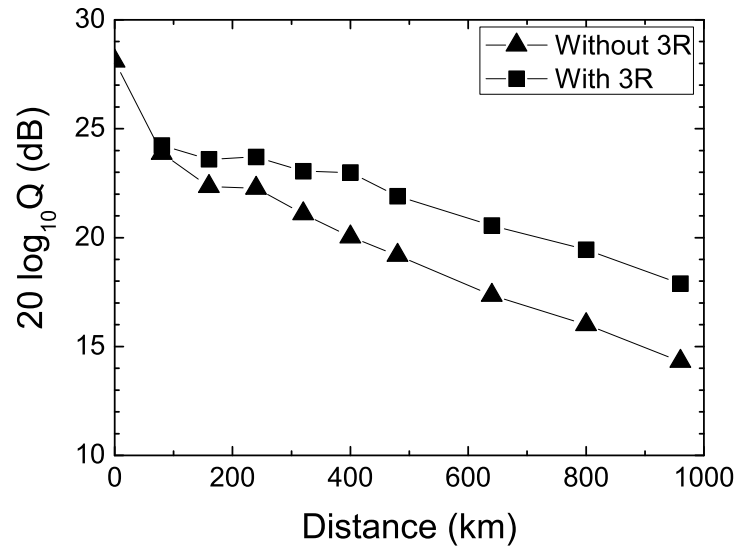


Figure 3.25: Dependence of the Q-factor on the transmission distance with the regenerator outside a loop.

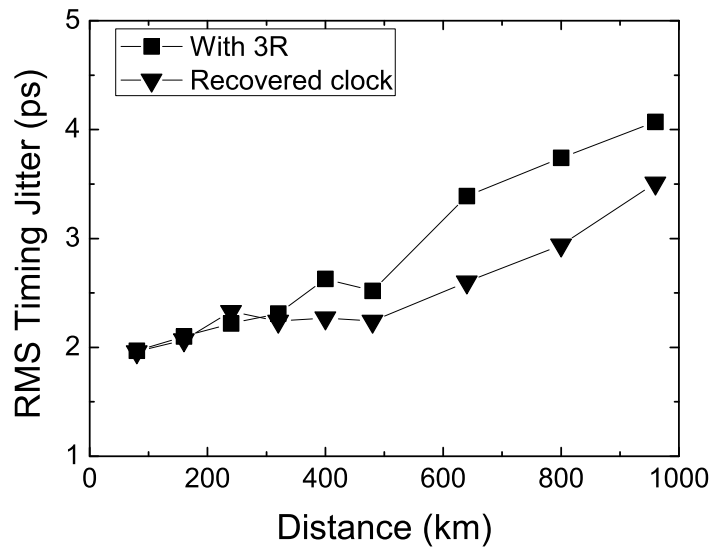


Figure 3.26: Dependence of the timing jitter on the transmission distance with the regenerator outside a loop.

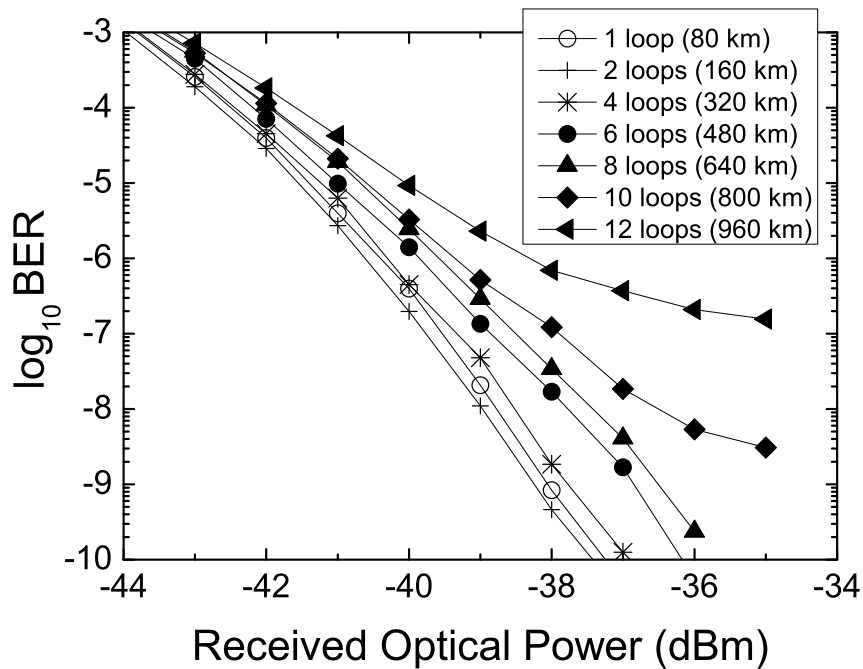


Figure 3.27: Dependence of the BER on the ROP with the regenerator outside a loop.

to increase quickly after 6 loops.

Fig. 3.27 shows the dependence of the BER on the received optical power for different numbers of loops. For up to 4 loops, the BER curves are very similar and show little power penalty compared to one loop. Therefore, based on results shown in Figs. 3.25 - 3.27, it is likely that the regenerator can be used every 320 - 480 km (4 - 6 loops) with a low power penalty. As the number of loops is increased further, BER floors are observed after 10 loops. This implies that the maximum regenerator spacing would be less than 800 km (10 loops).

3.4 Summary

A polarization-insensitive all-optical 3R regenerator that preserves the input signal wavelength has been characterized for a 10 Gb/s RZ-OOK signal. The use of Raman amplification allows a large filter offset ($\Delta\lambda_{\text{off1}} = -0.3$ nm) to be used in the retiming stage, which is compatible with the filter offset requirement for the reshaping stage. The regenerator is able to suppress amplitude noise and timing jitter while it does not cause a power penalty. For a recirculating loop experiment, with a regenerator spacing of 240 km, a 10 Gb/s RZ-OOK signal was transmitted over 18,000 km of fiber (75 regenerators) with a power penalty of 1.6 dB at a BER of 10^{-9} .

Chapter 4

The Regenerator for a 40 Gb/s signal

As the demand for higher data rates is increasing, regenerators also need to operate at bit rates from 40 to 160 Gb/s. Since the regenerator considered here is based on the femto-second SPM and XPM processes, the regeneration scheme is applicable to a bit rate of 40 Gb/s, and possibly bit rates of 100 - 160 Gb/s provided a low-jitter self-pulsating laser is available and the retiming and reshaping stages can be co-designed for wavelength-preserving operation. In this chapter, the regenerator is investigated for a bit rate of 40 Gb/s using a phase controlled mode beating three section laser with self-pulsating frequency at 40 GHz. In order to increase the bit rate, the regenerator parameters needed to be redesigned.

In section 4.1, important parameters are discussed for a 40 Gb/s regenerator. In section 4.2, the regenerator is characterized for the case of single regeneration. In section 4.3, the cascability is evaluated using a recirculating loop, and a summary is given in section 4.4.

4.1 Redesign of the regenerator for 40 Gb/s

Although the operating principle of the regenerator is based on fast processes, the regenerator is not bit rate transparent. Thus the regenerator parameters need to be redesigned as the bit rate is increased from 10 to 40 Gb/s. In this section, important parameters are discussed to operate the regenerator for a 40 Gb/s signal.

4.1.1 Self-pulsating laser

To increase the bit rate from 10 to 40 Gb/s, one of the most important components to modify is the self-pulsating (SP) laser since the SP-DFB laser used at 10 Gb/s is not applicable to a 40 Gb/s system. For clock recovery at 40 Gb/s, a phase-controlled mode-beating three section laser is used that self-pulsates around 39.813 GHz [27]. The laser has two distributed feedback (DFB) sections that are in lasing condition with center wavelengths that are slightly detuned from each other (~ 40 GHz apart). The SP frequency can be tuned by adjusting the injection current of the DFB sections. To obtain self-pulsation near 39.813 GHz, the injection current for the one lasing section was 200.00 mA with a longer wavelength and the other section was 117.89 mA with a shorter wavelength. The injection current of the phase tuning section was 0.0 mA. Fig. 4.1 shows a block diagram of the setup to test the SP laser and the clock recovery module. A RZ-OOK signal at 40 Gb/s ($2^{31} - 1$ PRBS) is degraded using a broad band source (BBS) and a variable optical attenuator (VOA) to adjust the OSNR of the input signal. The input data signal is applied to the SP laser via the optical circulator, and the optical bandpass filter centered at 1567 nm removes any reflection of the data signal from the SP laser. The recovered clock signal is

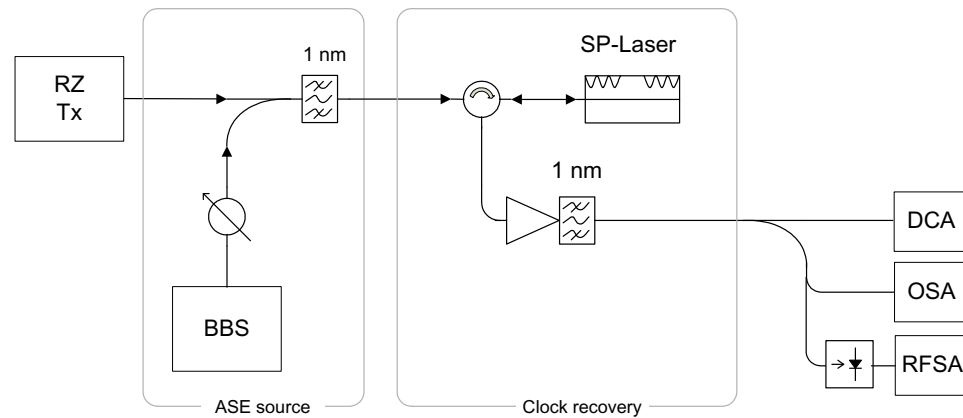


Figure 4.1: Block diagram of the clock recovery and the test setup; RZ-Tx: RZ transmitter, BBS: broad band source, DCA: digital communication analyzer, OSA: optical spectrum analyzer, RFSA: RF spectrum analyzer.

then amplified and various signal properties are measured. Fig. 4.2 shows the optical spectrum of the SP laser centered at 1567 nm. The laser has two lasing modes that beat with each other to generate self-pulsation. Fig. 4.3 shows the RF spectrum of the detected optical signal from the laser with and without a data signal injected into the laser. The locking range is about ± 100 MHz. Fig. 4.4 shows the dependence of the RMS timing jitter of the data and recovered clock signals on the input signal OSNR (a noise bandwidth of 0.1 nm). Timing jitter was measured from a sampling oscilloscope as the OSNR of the input data signal was varied and averaged for both rising and falling edges. When the input signal OSNR is below 25 dB, the timing jitter of the recovered clock signal is smaller than that of the input data signal. When the input signal OSNR is higher than 9 dB, the timing jitter is maintained below 500 fs. Fig. 4.5 shows the eye diagram of the recovered clock signal for an input signal OSNR of 30 dB.

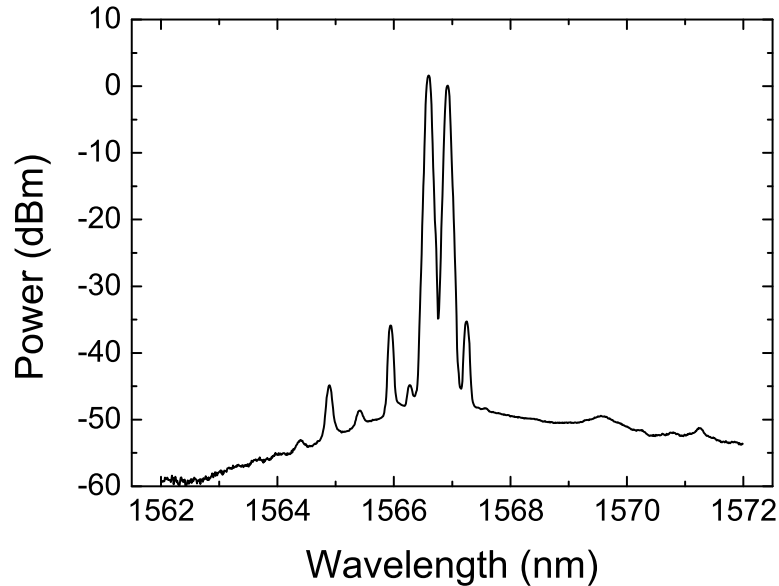


Figure 4.2: Optical spectrum of the self-pulsating laser at 40 GHz (resolution bandwidth of 0.1 nm).

4.1.2 Raman amplification

The change of the center wavelength of the SP laser has an impact on the Raman gain for the retiming stage. The main purpose of using Raman amplification is to increase the XPM efficiency by providing a large gain for the pump signal (i.e., the clock signal). As shown in chapter 3, the SP laser for a 10 Gb/s signal had a center wavelength at 1538 nm and the Raman laser was operated at 1425 nm. It provided gains for both the clock (1538 nm) and data (1544 nm) signals. On the other hand, the SP laser for a 40 Gb/s signal is centered at 1567 nm and the Raman pump signal at 1425 nm does not provide an enough gain. Thus dual Raman pump signals at 1425 and 1453 nm were used to provide gains for both the data and clock signals, respectively. However, the Raman laser is designed for the C-band and it provides

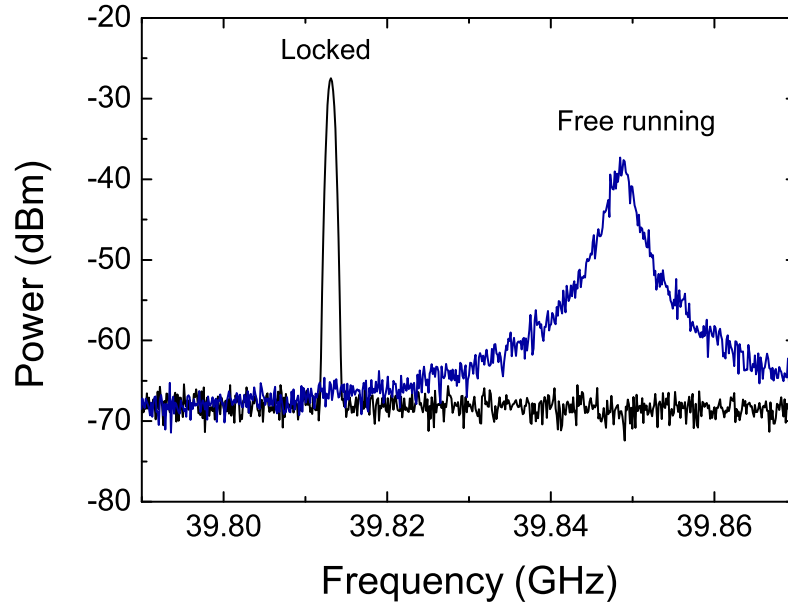


Figure 4.3: RF spectrum of the detected signal from the self-pulsating laser at 40 GHz (resolution bandwidth of 750 kHz).

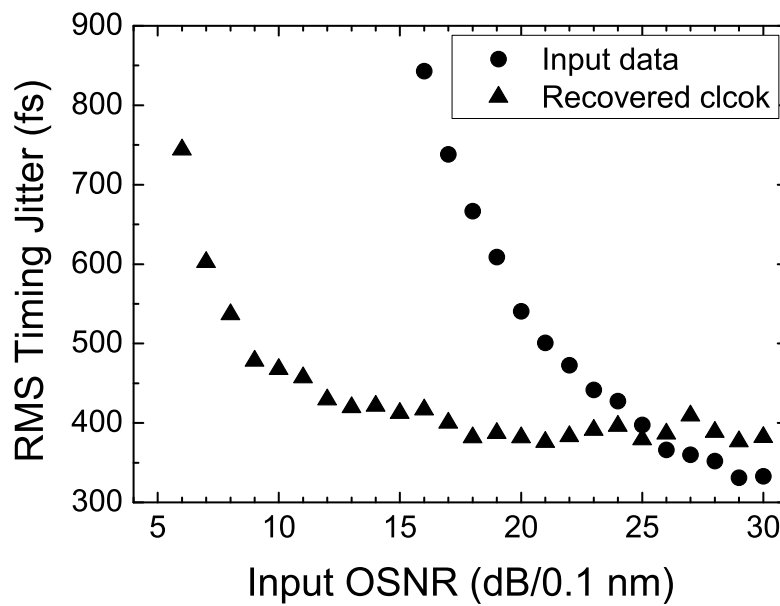


Figure 4.4: Dependence of the RMS timing jitter on the input signal OSNR.

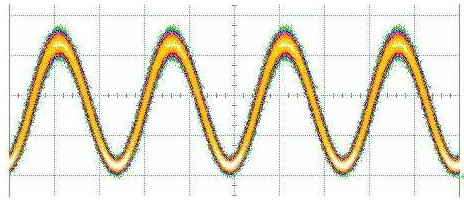


Figure 4.5: Eye diagram of the recovered clock signal for an input signal OSNR of 30 dB (time base = 10 ps/div).

approximately 4 dB less gain for the clock signal at 1567 nm than the clock signal at 1538 nm. Therefore other parameters need to be modified in order to compensate for the lower Raman gain.

4.1.3 Highly nonlinear fiber

Highly nonlinear fibers are used to obtain nonlinear phase modulation (XPM and SPM). As the bit rate is increased from 10 to 40 Gb/s, the pulse width of the data signal is reduced from 43 ps to 11 ps (FWHM). This has an impact on the nonlinear phase modulation, pulse broadening, and walk-off length. These require modification of HNLF parameters to operate at 40 Gb/s.

4.1.4 Retiming stage

In an ideal case, the data and clock signals should propagate with the same group velocity and be aligned in time to maximize the XPM efficiency. However in reality, the data and clock signals travel at slightly different speeds due to wavelength dependent group index in a fiber which causes group velocity mismatch. Once the data and clock signals are completely misaligned, no XPM induced spectral broadening occurs. Fig.

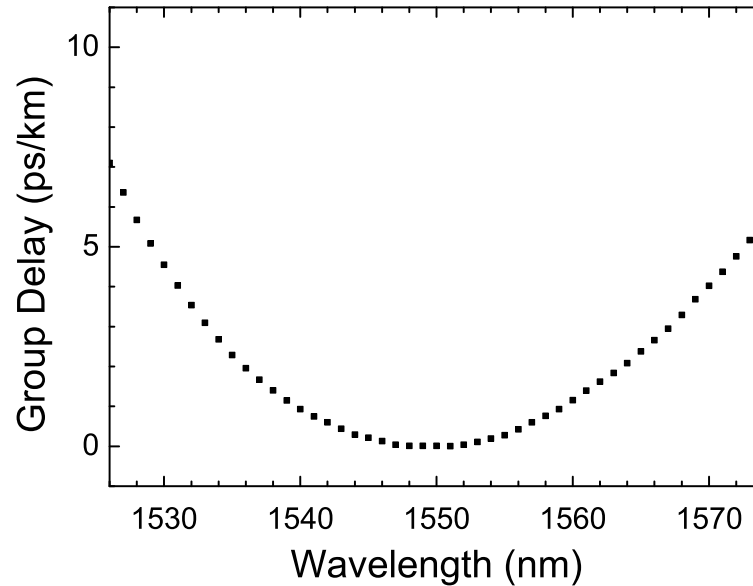


Figure 4.6: Measured relative group delay for 1 km of the XPM-HNLF.

4.6 shows the group delay for 1 km of XPM-HNLF. This group delay is measured using an optical dispersion analyzer and the measured value is relative to the group delay at 1550 nm (not the absolute group delay). For a 10 Gb/s signal, 2 km of XPM-HNLF was used in the retiming stage. If we use the same length of the XPM-HNLF, assuming the data and clock signal wavelengths are 1545 nm and 1567 nm, respectively, these two signals will walk-off by 5.5 ps after propagating 2 km of XPM-HNLF. This signal walk-off reduces XPM efficiency.

Because of the group velocity mismatch and the lower gain of the Raman amplification, the length of the XPM-HNLF needs to be increased to provide more XPM for the retiming stage. To find a fiber length that maximizes XPM, we can calculate the

walk-off length (L_w) using the following relation,

$$L_w = \frac{T_0}{|d|}, \quad (4.1)$$

where d and T_0 are the walk-off parameter and pulse width as defined in (2.10) and (2.14), respectively. Using the fact that the group velocity can be obtained from the measured group delay (τ_g) and using the relation $\tau_g = L/v_g$, we obtain a walk-off length of 2.88 km for a signal with a pulse width of 11 ps (FWHM). If the length of the XPM-HNLF is increased to 3 km, the amount of the signal walk-off between the data and clock signals is 8.3 ps at the output of the XPM-HNLF. For a 40 Gb/s signal, the impact of the group delay mismatch is not negligible. (This was not significant for a 10 Gb/s signal with 43 ps pulse width.)

Considering the walk-off length, it may seem desirable to shorten the length of the HNLF to reduce the total signal walk-off between the data and the clock signals. However, 3 km of HNLF was still chosen for two reasons. First, since the Raman amplification provided 4 dB less gain for the clock signal at 1567 nm, a longer length of the HNLF is needed to maximize the XPM. Second, relative delay can slowly vary over time due to environmental change such as temperature. The signal walk-off will average some amount of the induced XPM on the data signal even if the data and clock signals are slightly misaligned in time.

4.1.5 Offset filter

The offset filters also need to be redesigned as the bit rate changes. The most important factors to be considered are the filter bandwidth and the offset of the center wavelength.

Filter bandwidth

The bandwidth of the offset filter affects the pulse width of the filtered signal for both retiming and reshaping stages. If we assume the spectral shape of the filtered signal is Gaussian, the corresponding waveform is also Gaussian shaped. In this case, the spectral width determines the pulse width and the relation is given by

$$\Delta f_{FWHM} = \frac{2 \ln 2}{\pi T_{FWHM,out}} \quad (4.2)$$

or in terms of wavelength

$$\Delta \lambda_{FWHM} = \frac{2 \ln 2 \lambda^2}{\pi c T_{FWHM,out}}. \quad (4.3)$$

In order to obtain an output signal with 10 ps pulse width (FWHM), the theoretical bandwidth of the offset filter should be 0.35 nm. In order to keep the pulse widths of the input and output signals similar, a bandwidth of 0.55 nm was used for the offset filter in the reshaping stage.

For the retiming stage, as shown in Fig. 3.6(b) for a 10 Gb/s signal, the polarization independent XPM is observed in a small region. In theory, to achieve the polarization-insensitive retiming, the bandwidth of the offset filter should be narrow enough so that it only passes the region that is polarization independent. However, although a large bandwidth increases the dependence on the input signal SOP in the retiming stage, a slightly wider bandwidth is preferred due to several reasons. First, an offset filter with a large bandwidth produces an output signal with a higher power. Second, a narrow pulse width can provide more SPM in the reshaping stage for the same input average power. Third, if the dispersion of the SPM-HNLF causes pulse broadening, a narrow input pulse width can reduce the interference with adjacent

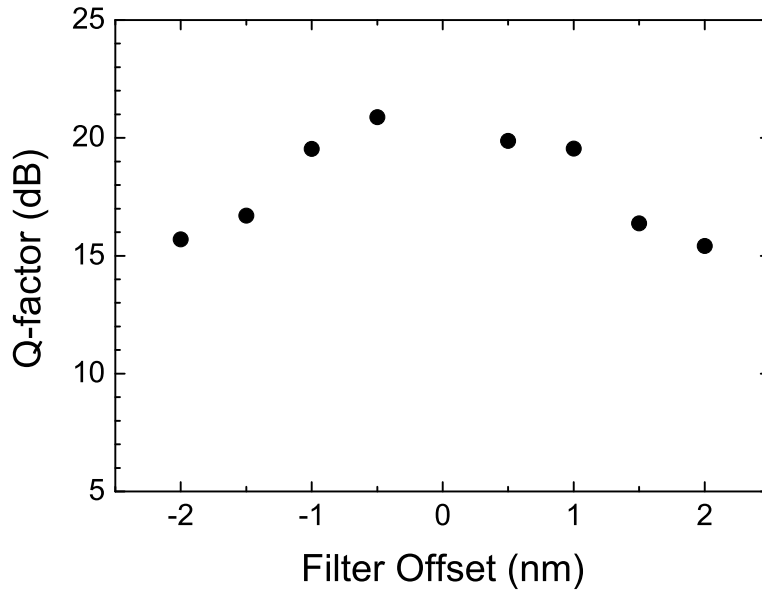


Figure 4.7: Dependence of the Q-factor in the retiming stage on the filter offset.

pulses. Last, if carefully designed, the SOP dependence can be transferred to an amplitude fluctuation which can be reduced in the reshaping stage. For these reasons, an offset filter with a 1 nm bandwidth is used in the retiming stage.

Filter offset

In the first demonstration of the regenerator for the 10 Gb/s signal [65], the optimal filter offset for the retiming stage was found close to the center wavelength (0.16 nm offset) and the largest attainable offset was limited. This restriction continues at 40 Gb/s. Fig. 4.7 shows the dependence of the Q-factor after the retiming stage on the filter offset. The input signal at 1545 nm was not degraded. The dual Raman pump signals at 1425 nm and 1453 nm had launch powers of 25.0 dBm and 23.7 dBm, respectively. The data and clock signal powers to the XPM-HNLF were separately

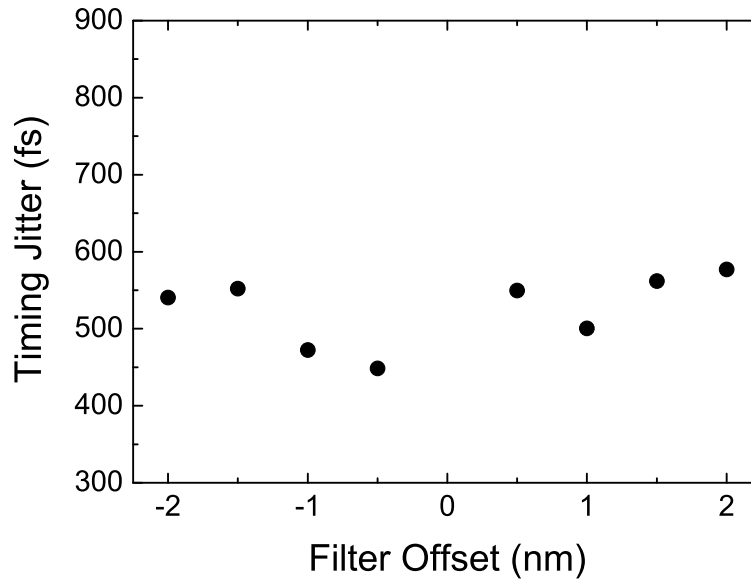


Figure 4.8: Dependence of the RMS timing jitter after the retiming stage on the filter offset.

optimized for each measurement. The Q-factor decreases as the offset moves away from the center wavelength and the highest Q-factor is obtained at the offset of -0.5 nm. Fig. 4.8 shows the dependence of the timing jitter after the retiming stage on the filter offset. The parameters for the retiming stage are the same as those for Fig. 4.7. The timing jitter also tends to increase as the filter offset increases and the lowest timing jitter is found at -0.5 nm of offset. Based on Fig. 4.7 and 4.8 one can conclude that a -0.5 nm offset is optimum if only the retiming stage is considered.

Fig. 4.9 shows the dependence of the Q-factor on the filter offset when only the reshaping stage is considered. For this measurement, the retiming stage was bypassed and the input signal to the regenerator was directly used to assess the reshaping stage. The highest Q-factor is obtained when the offset is -1.5 nm for the negative offset or

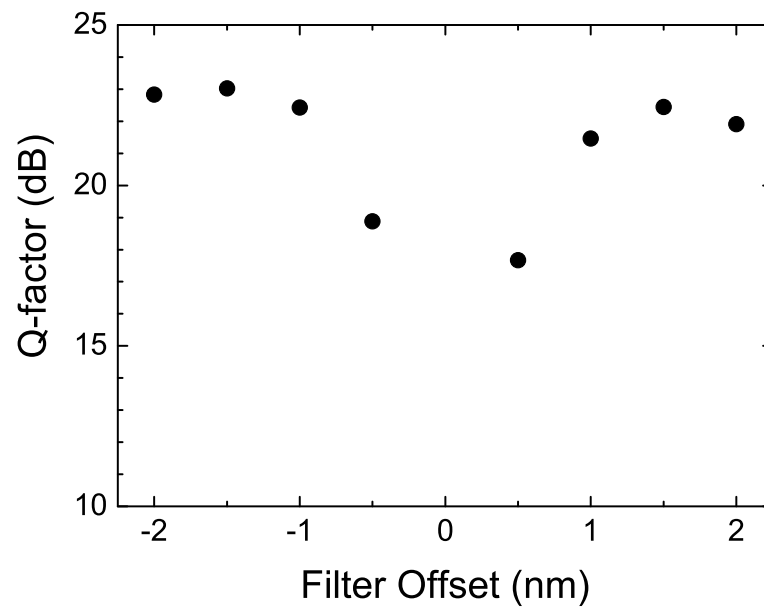


Figure 4.9: Dependence of the Q-factor on the filter offset in the reshaping stage only.

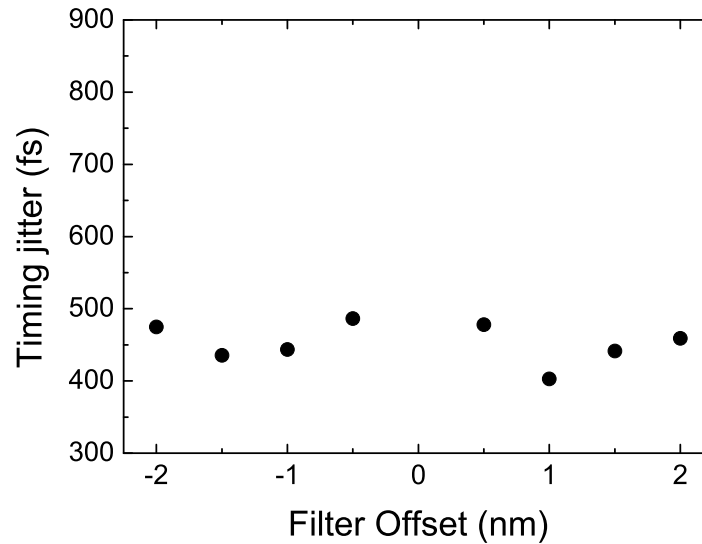


Figure 4.10: Dependence of the RMS timing jitter on the filter offset in the reshaping stage only.

1.5 nm for the positive offset. Fig. 4.10 shows the corresponding timing jitter when only the reshaping stage is considered. The minimum timing jitter is found when the offset is -1.5 nm for the negative offset and 1 nm for the positive offset. Thus, one can conclude that if only the reshaping stage is considered, the optimum offsets are approximately -1.5 nm and 1.5 nm.

To summarize, the optimum offsets for the retiming and reshaping stages do not coincide with each other. Therefore, the offsets for both stages have to be chosen carefully to achieve wavelength-preserving regeneration. As will be described later, the filter offset for the retiming stage was -0.5 nm and for the reshaping stage was 0.5 nm. This implies that the selection of the filter offset is more strongly determined by the retiming stage.

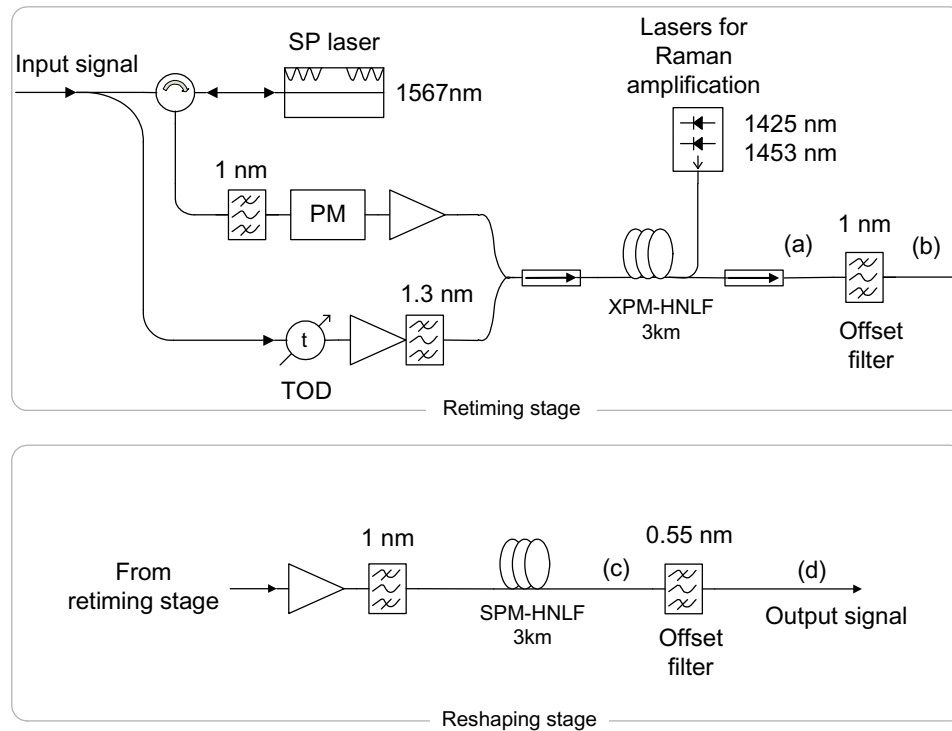


Figure 4.11: Regenerator setup for a 40 Gb/s signal; SP laser: self-pulsating laser, PM: phase modulator, TOD: tunable optical delay, XPM-HNLF: XPM inducing highly nonlinear fiber, SPM-HNLF: SPM inducing highly nonlinear fiber.

4.2 Performance of the regenerator

Fig. 4.11 illustrates the regenerator block diagram for a 40 Gb/s RZ-OOK signal. In the retiming stage, a clock signal was recovered from the self-pulsating laser (1567 nm) and used as the pump signal to induce XPM on the data signal in 3 km of XPM-HNLF (nonlinearity of $10.6 \text{ W}^{-1}\text{km}^{-1}$, attenuation of 0.76 dB/km, dispersion of -0.05 ps/nm/km at 1550 nm, and dispersion slope of $0.017 \text{ ps/nm}^2/\text{km}$). Launch powers of the clock and data signals to the XPM-HNLF were 14.8 dBm and 5.8 dBm, respectively. A TOD was used to adjust the relative time delay between the clock and data pulses thereby balancing the timing jitter of the rising and falling edges of

the retimed signal. A phase modulator driven by a 1 GHz sinusoidal signal increased the spectral width of the clock signal to reduce SBS of the clock signal [135, 136]. For low-noise Raman amplification, depolarized dual pump signals at 1425 and 1453 nm were counter propagated in the XPM-HNLF with powers of 25.0 dBm and 23.7 dBm, respectively. After the XPM-HNLF, an offset filter (1 nm bandwidth) sliced a portion of spectrum centered at -0.5 nm offset from the data signal wavelength. In the reshaping stage, the retimed signal spectrum was broadened by SPM in 3 km of SPM-HNLF (nonlinearity of $10.6 \text{ W}^{-1}\text{km}^{-1}$, attenuation of 0.76 dB/km, and dispersion of -0.26 ps/nm-km at 1550 nm). The launch power to the SPM-HNLF was 19.2 dBm. The offset filter was centered at 1545 nm which is the same wavelength as the input signal, and had a bandwidth of 0.55 nm. This produced an output signal with a pulse width of 10 ps and the same wavelength as the input signal. Table 4.1 summarizes the parameters used for the regenerator.

Table 4.1: Regenerator parameters for a 40 Gb/s signal.

Retiming stage	Parameter	Value
Data signal	Wavelength	1545 nm
	Input power to XPM-HNLF	1.0 dBm
	Pulse width	11 ps (FWHM)
	PRBS pattern length	$2^{31} - 1$
Clock signal	Wavelength	1567 nm
	Input power to XPM-HNLF	16.9 dBm
Raman pump signal 1	Wavelength	1425 nm
	Pump power	25.0 dBm
Raman pump signal 2	Wavelength	1453 nm
	Pump power	24.3 dBm
XPM-HNLF	Length	3 km
	Nonlinearity	$10.6 \text{ W}^{-1}\text{km}^{-1}$
	Dispersion	-0.05 ps/nm/km
	Dispersion slope	$0.017 \text{ ps/nm}^2/\text{km}$
Offset filter	Offset ($\Delta\lambda_{\text{off1}}$)	-0.5 nm
	Bandwidth	1.0 nm
Reshaping stage	Parameter	Value
Data signal	Wavelength	1544.5 nm
	Input power to SPM-HNLF	21.2 dBm
SPM-HNLF	Length	3 km
	Nonlinearity	$10.6 \text{ W}^{-1}\text{km}^{-1}$
	Dispersion	-0.26 ps/nm/km
	Dispersion slope	$0.017 \text{ ps/nm}^2/\text{km}$
Offset filter	Offset($\Delta\lambda_{\text{off2}}$)	0.5 nm
	Bandwidth	0.55 nm

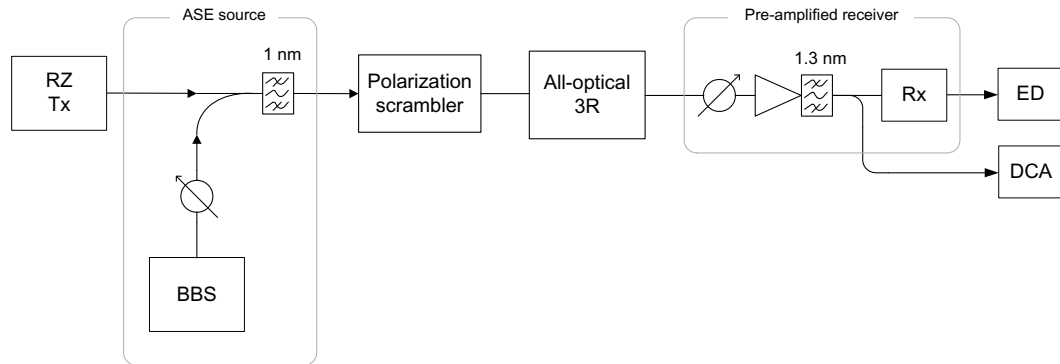


Figure 4.12: Experimental setup of the regenerator for a 40 Gb/s signal; RZ-Tx: RZ signal transmitter, BBS: broad band source, Rx: receiver, ED: error detector, DCA: digital communication analyzer.

Fig. 4.12 shows the experimental setup for a 40 Gb/s RZ-OOK signal at 1545 nm ($2^{31} - 1$ PRBS) with a pulse width of 11 ps. The optical signal-to-noise ratio (OSNR) of the input data signal was adjusted using a BBS and a VOA. The SOP of the input data signal was scrambled using a polarization scrambler at a scan rate of 280 deg/s. The degraded signal was then applied to the regenerator. At the output of the regenerator, the signal was applied to a pre-amplified receiver that consisted of a VOA, EDFA and optical receiver. Fig. 4.13 shows the optical spectra of the data signal measured with a resolution bandwidth of 0.06 nm at several locations in the regenerator (refer to Fig. 4.11). Optical spectra are measured with 5 different SOPs of the input data signal. Fig. 4.13(a) shows the data signal spectra after the XPM-HNLF. Although the optical spectra show a dependence of the XPM broadened spectrum on the SOP of the input data signal, there exist polarization independent wavelengths as indicated by the two arrows. Fig. 4.13(b) shows the spectra after the retiming stage. 4.13(c) and (d) show the spectra after the SPM-HNLF and after the reshaping stage, respectively. As the data signal passes through the regenerator from

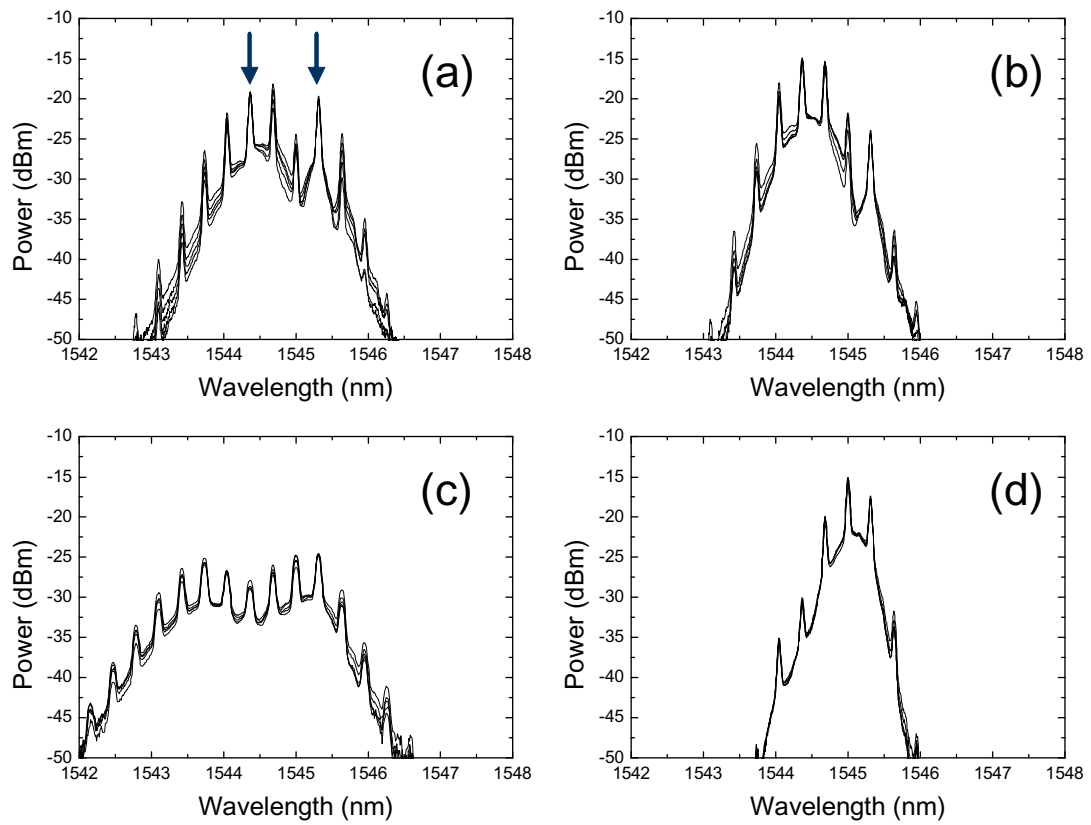


Figure 4.13: Optical spectra of the data signal at several locations in the regenerator; (a) data signal after XPM-HNLF, (b) after retiming stage, (c) after SPM-HNLF, (d) after reshaping stage.

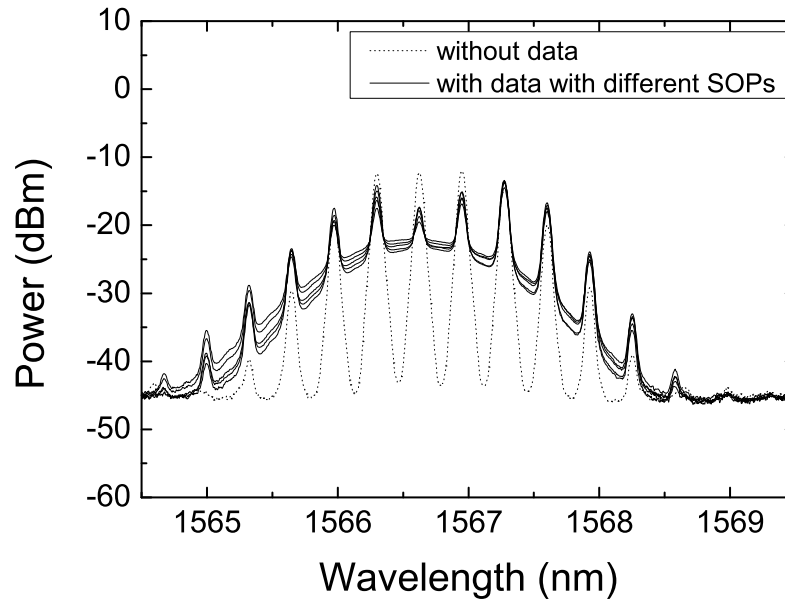


Figure 4.14: Optical spectra of the clock signal after XPM-HNLf with and without the data signal (with 5 different SOPs).

(a) to (d), the dependence of the SOP is significantly reduced.

Fig. 4.14 shows the optical spectra of the clock signal after the XPM-HNLf with different SOPs of the input data signal (resolution bandwidth of 0.06 nm). For comparison the clock signal without the data signal (no XPM) is also shown. Initially, the recovered clock signal had two modes as shown in Fig. 4.2. Due to the high input power of the clock signal and the Raman gain inside the XPM-HNLf, SPM and FWM occur and a very broad spectrum is observed at the output of the XPM-HNLf.

Fig. 4.15 shows the dependence of the Q-factor of the regenerated signal on the input signal OSNR (noise bandwidth of 0.1 nm) of the input signal to the regenerator. The Q-factor is measured from a sampling oscilloscope. For comparison, the results with fixed and scrambled SOPs are shown as well as without the regenerator. The

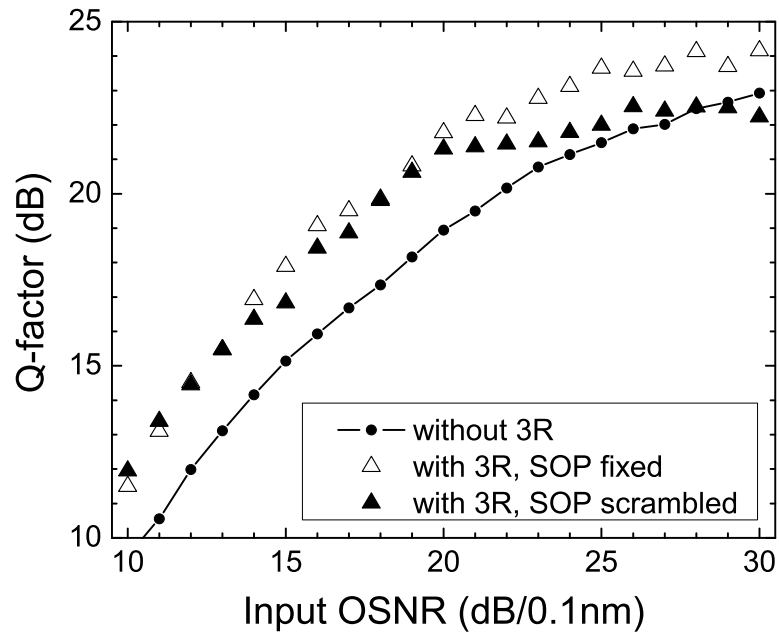


Figure 4.15: Dependence of the Q-factor on the input signal OSNR.

Q-factor is improved with the regenerator when the input signal OSNR is below 27 dB and the improvement is over 2 dB when the input signal OSNR is below 20 dB. The Q-factor improvement implies that the noise in the one and zero levels is reduced by the regenerator. For input signal OSNRs higher than 20 dB, the Q-factor with SOP scrambling is worse than that with a fixed SOP. This is due to the SOP dependent slow power fluctuation of the one level. Although the SOP dependent power fluctuation always exists to a certain extent, when the noisy signal ($\text{OSNR} \leq 20$ dB) is regenerated, the SOP dependent power fluctuation is not noticeable compared to the amplitude noise after regeneration. As will be shown later (Fig. 4.18), the required input signal OSNR to obtain the BER of 10^{-9} is 17.5 dB. Thus for the OSNR range of interest (17.5 - 22 dB), the regenerator is seen to be polarization-insensitive in terms of the Q-factor. Fig. 4.16 shows the corresponding eye diagrams with the SOP of

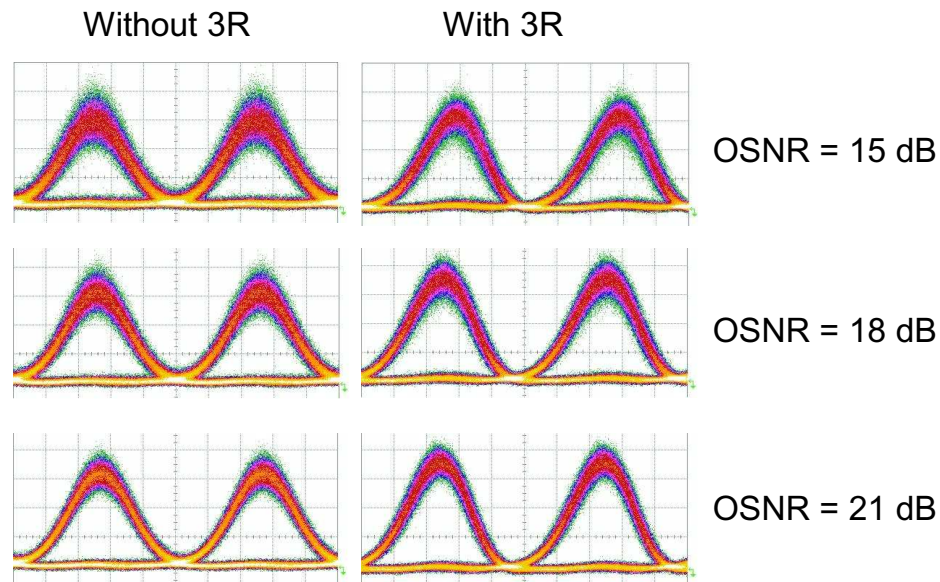


Figure 4.16: Eye diagrams without and with the 3R regenerator for input signal OSNR values of 15, 18, and 21 dB. The SOP of the input data signal is scrambled (time base = 5 ps/div).

the input data signal scrambled for three input signal OSNR values.

Fig. 4.17 shows the dependence of the output signal RMS timing jitter on the input signal RMS timing jitter. The timing jitter was measured using a sampling oscilloscope with precision timebase (intrinsic jitter of 200 fs). For comparison, the RMS timing jitter for the recovered clock signal and the regenerated signal with a fixed SOP for the input signal are also shown. The timing jitter of the clock signal is below 420 fs when the input signal timing jitter is less than 900 fs. After regeneration with a scrambled SOP, the output signal timing jitter can be reduced when the input signal timing jitter is larger than 550 fs. The output signal timing jitter with a scrambled SOP is slightly larger than that with a fixed SOP.

To further assess the 3R regenerator, the dependence of the BER on the input

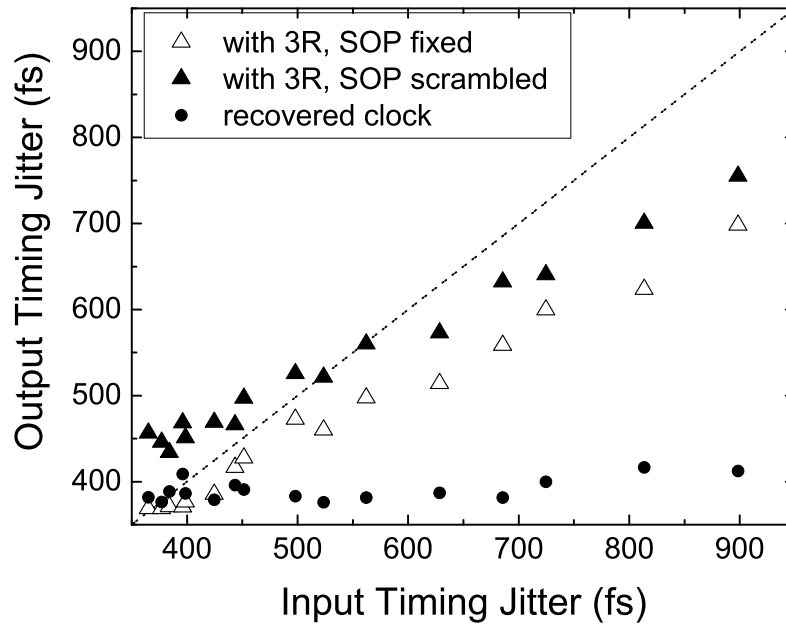


Figure 4.17: Dependence of the output signal RMS timing jitter on the input signal RMS timing jitter.

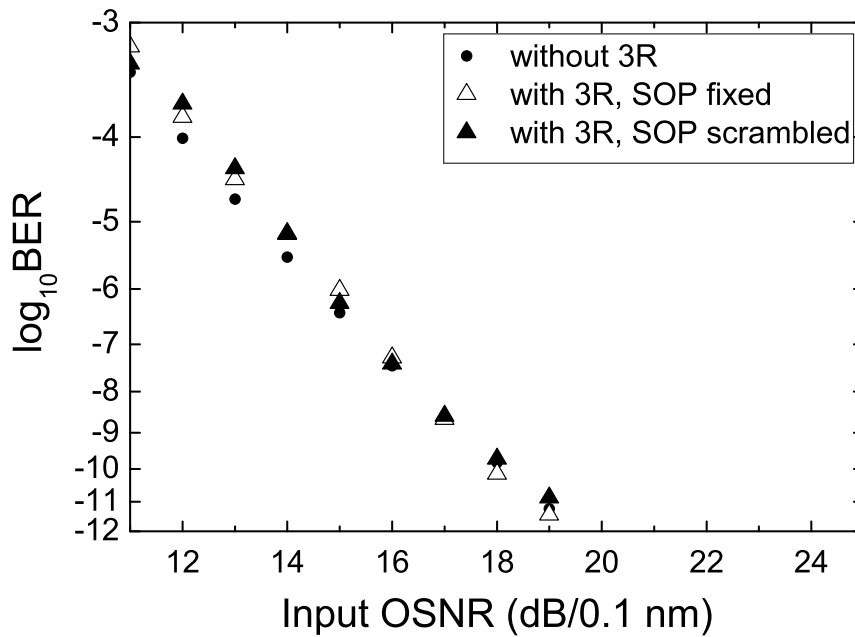


Figure 4.18: Dependence of the BER on the input signal OSNR of the regenerator with a ROP of -15 dBm.

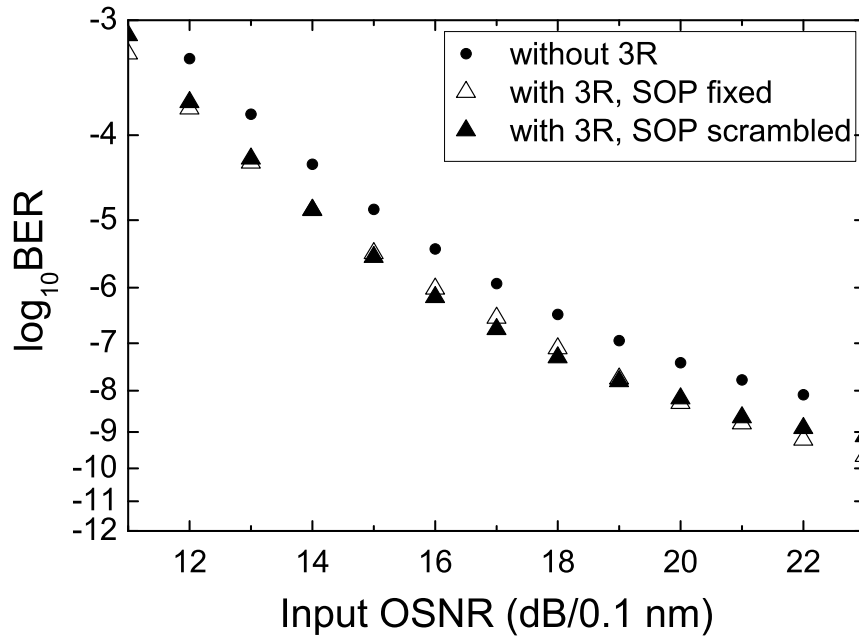


Figure 4.19: Dependence of the BER on the input signal OSNR of the regenerator with a ROP of -32 dBm.

signal OSNR is evaluated. First, the ROP was set high enough so that the impact of noise from the pre-amplified receiver was minimal. Fig. 4.18 shows the dependence of the BER on the input signal OSNR with a ROP of -15 dBm. For comparison, BER curves with a fixed SOP and without the regenerator are also shown. As can be seen, no BER penalty was induced by the 3R regenerator and BER performance is insensitive to the SOP of the input signal. Therefore the regenerator does not degrade the BER while reducing the amplitude noise and timing jitter as shown in Figs. 4.15 and 4.17. In order to keep the system BER below 10^{-9} , the input signal OSNR to the regenerator should be over 17.5 dB. In practice, the input signal OSNR of 20 - 22 dB seems to be a good choice for the regenerator.

In order to show the improvement offered by the regenerator, subsequent noise is

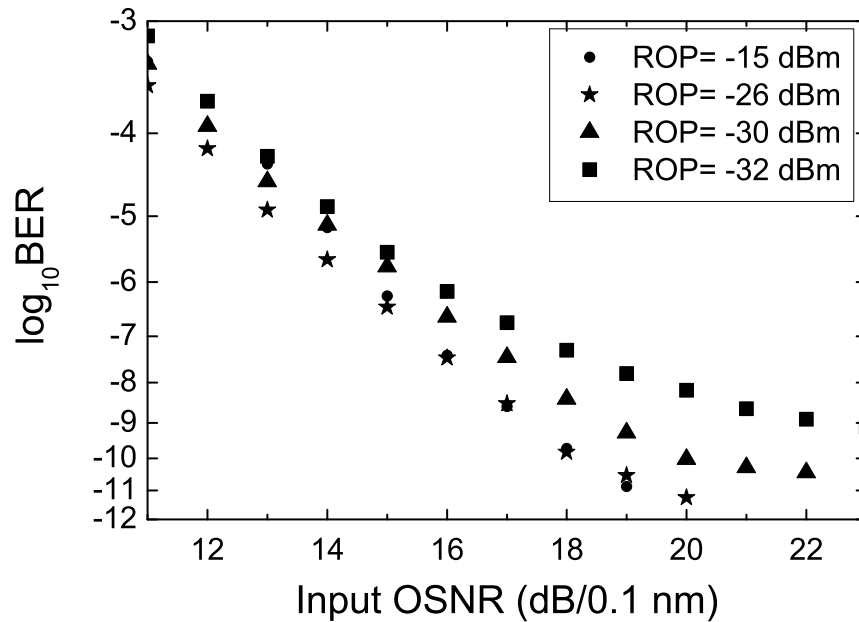


Figure 4.20: Dependence of the BER on the input signal OSNR of the regenerator with input SOP scrambled and different received optical powers.

added to the regenerated signal. This emulates further degradation of the data signal after regeneration. Since the regenerator reduces amplitude noise and timing jitter, the regenerated signal is more resilient against the subsequent noise. To add subsequent noise, the input signal power to the pre-amplifier is decreased to add receiver noise. Fig. 4.19 shows the dependence of the BER on the input signal OSNR with a ROP of -32 dBm. The BER curves with the regenerator show improvement over the case without regeneration. For a small value of the ROP, the BER floors are due to the noise added in the pre-amplified receiver. Fig. 4.20 shows the dependence of the BER on the input signal OSNR with different ROPs. The SOP of the input signal is scrambled during the measurement. For ROPs between -15 and -26 dBm, the impact of receiver noise is negligible. As the ROP is decreased to -32 dBm, the receiver noise starts to degrade the BER curves.

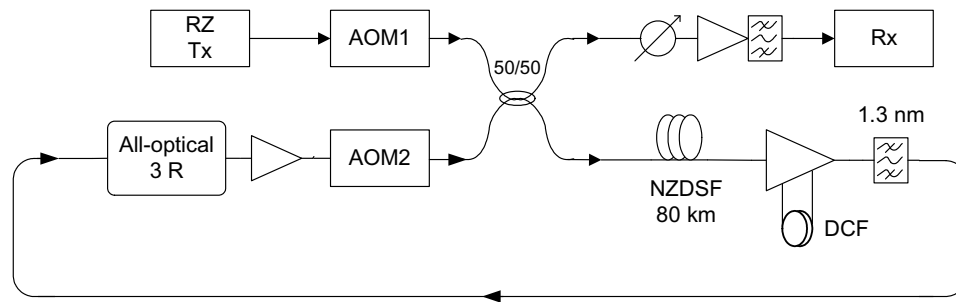


Figure 4.21: Loop experiment setup for a 40 Gb/s signal.

4.3 Recirculating loop experiment

Fig. 4.21 shows the experimental setup for the recirculating loop. The dispersion managed transmission span consisted of 80 km of non-zero dispersion-shifted fiber (NZDSF) (attenuation of 0.2 dB/km and dispersion of 4.4 ps/nm-km at 1550 nm), dispersion compensating fiber (total loss of 2.99 dB and total dispersion of -365 ps/nm at 1550 nm), and a two-stage EDFA. The residual dispersion of the transmission span was 3.8 ps/nm at 1550 nm. An optical bandpass filter was used in the loop to emulate a wavelength division demultiplexer and to suppress out-of-band noise. After regeneration, an additional EDFA compensated for the loss of the AOM2 and 50/50 coupler. A pre-amplified receiver was used to provide a signal for measuring the Q-factor and BER. Table 4.2 summarizes the parameters for the recirculating loop experiment. Although the regenerator has been shown to be polarization-insensitive in the previous section, a polarization scrambler was not used inside the loop. The operating condition of the self-pulsating laser that yields polarization-insensitive clock recovery also yields a small dynamic range for the input power (1~2 dB). Consequently, power fluctuations at the beginning of the data burst in the recirculating loop can cause the laser to not self-pulsate. This behavior has only been observed in the loop

Table 4.2: Parameters for the recirculating loop experiment for a 40 Gb/s signal.

Component	Parameter	Value
Non-zero dispersion shifted fiber	Length	80 km
	Attenuation	0.2 dB/km
	Dispersion	4.4 ps/nm/km at 1550 nm
Dispersion compensating fiber	Total loss	2.99 dB
	Total dispersion	-365 ps/nm at 1550 nm
EDFA	Launch power	1 dBm
Optical filter	Center wavelength	1545 nm
	Bandwidth	1.3 nm

experiments so we believe the regenerator can be cascaded with SOP scrambling in a straight line transmission experiment. For the recirculating loop experiment, the SP laser was biased so that it had a wide range of input power (>7 dB) but was somewhat dependent on the SOP of the input signal. In this operating condition, when the SOP of the input data signal varied, the relative delay between the data and clock signals changed in a repeatable way which affected the XPM induced spectral broadening. During the loop experiment, we found that the optimum filter offset for the retiming stage was $\Delta\lambda_{\text{off1}} = -0.7$ nm and for the reshaping stage was $\Delta\lambda_{\text{off2}} = 0.7$ nm, and these offsets were used to perform the recirculating loop experiment. Fig. 4.22 shows the dependence of the Q-factor on the transmission distance for 1R and 3R regeneration. The Q-factor was measured using a sampling oscilloscope. For 1R regeneration, the Q-factor is 12.2 dB for 15 loops (1,200 km) and with 3R regeneration, the Q-factor is 17.4 dB for 100 loops (8,000 km). Fig. 4.23 shows the dependence of the RMS timing jitter on the transmission distance. The timing jitter was measured using a sampling oscilloscope with a precision timebase module (200 fs

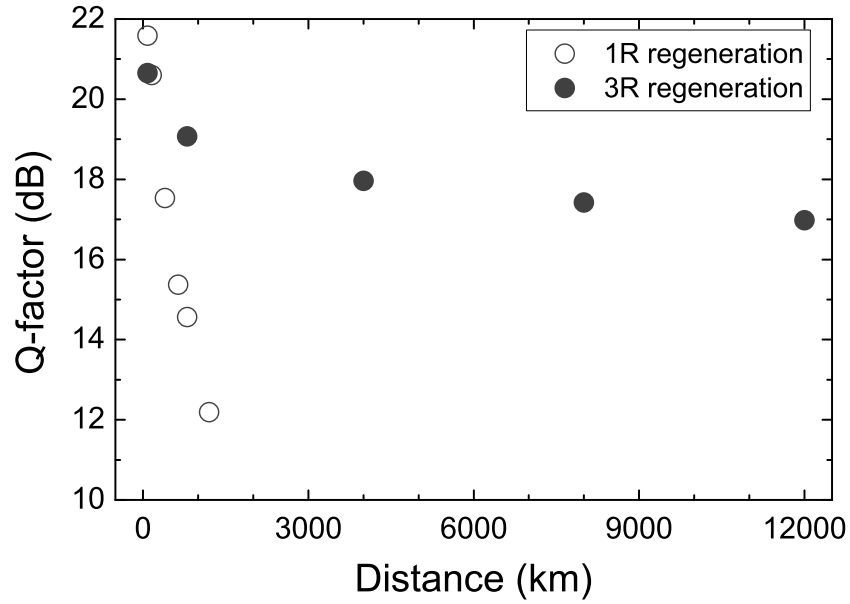


Figure 4.22: Dependence of the Q-factor on the transmission distance.

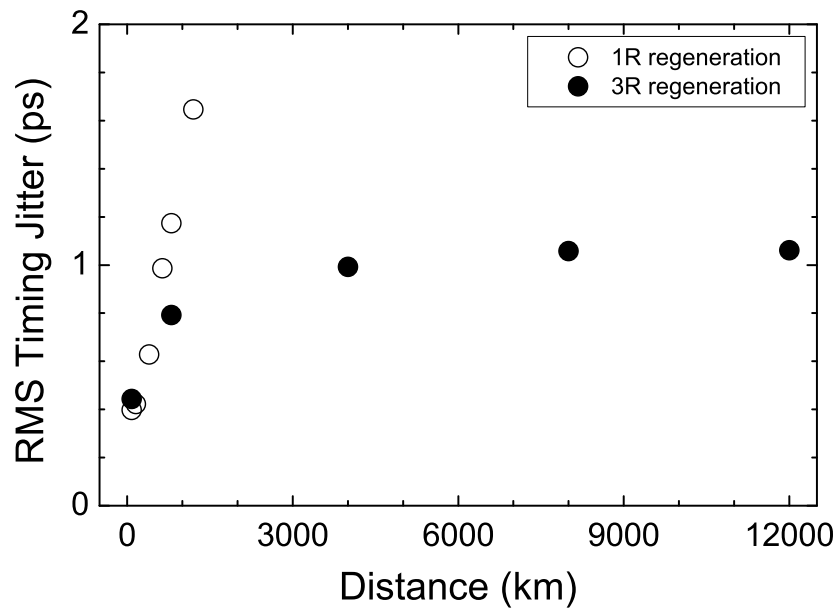


Figure 4.23: Dependence of the RMS timing jitter of the output signal on the transmission distance.

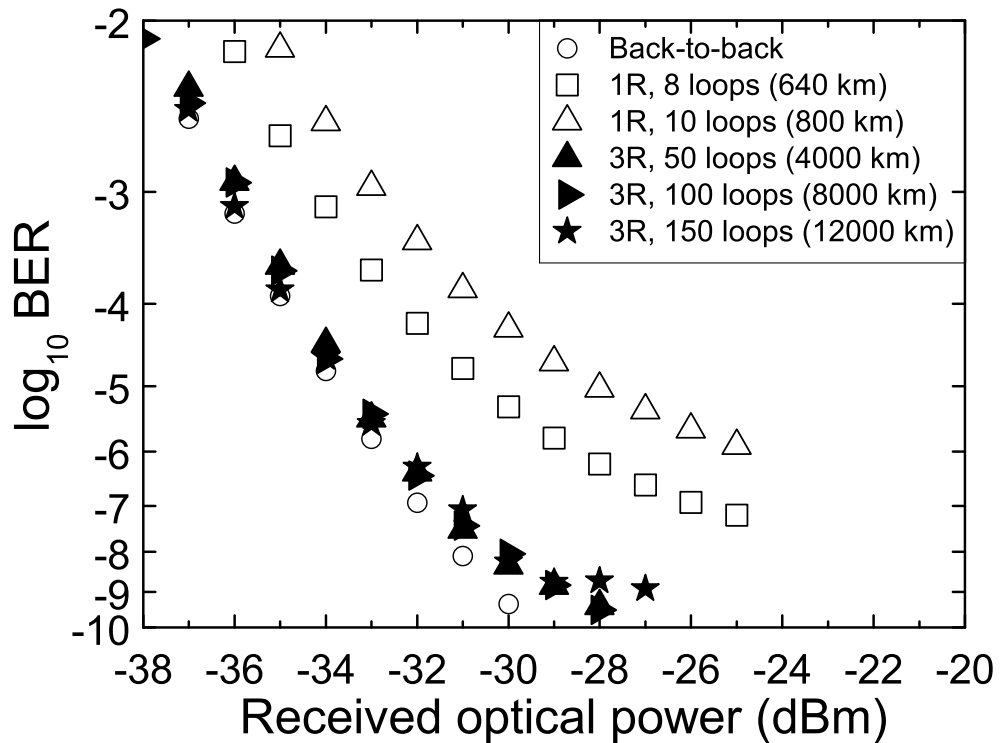


Figure 4.24: Dependence of the BER on the ROP with 80 km regenerator spacing.

intrinsic timing jitter). The timing jitter is maintained below 1.1 ps over 8,000 km.

Fig. 4.24 shows the dependence of the BER on the ROP with the 3R regenerator for 50, 100, and 150 loops. Back-to-back and 1R results are also shown for comparison. With 1R regeneration, a large power penalty is observed for 10 loops. With 3R regeneration, a power penalty of only 1.2 dB (at a BER of 10^{-9}) is obtained for 100 loops (8,000 km). Fig. 4.25 shows the eye diagrams for 1R and 3R regeneration with a different number of loops.

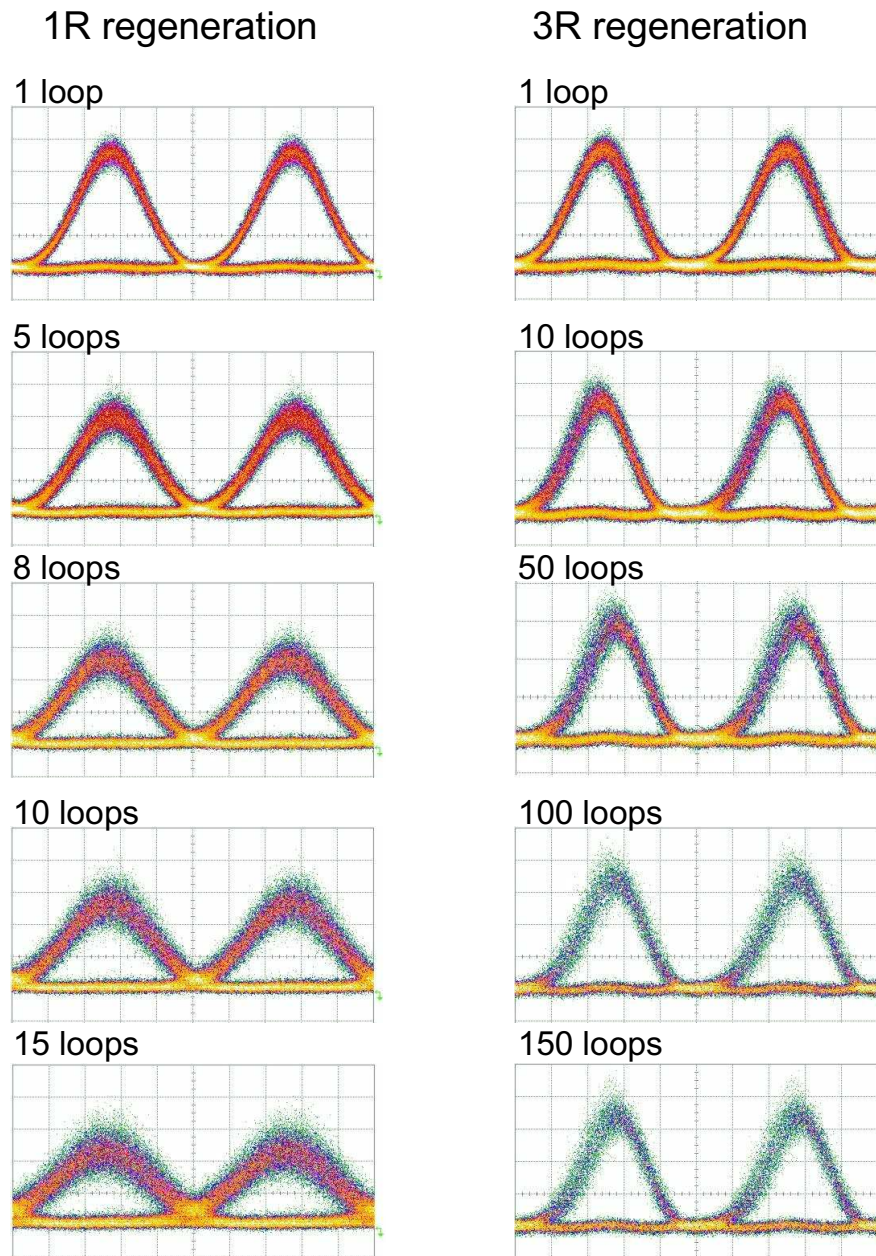


Figure 4.25: Eye diagrams for 1R and 3R regeneration with a different number of loops (time base = 5 ps/div).

4.4 Summary

Wavelength-preserving polarization-insensitive all-optical 3R regeneration has been investigated at 40 Gb/s. In order to increase the bit rate from 10 to 40 Gb/s, the regenerator parameters are redesigned and a 40 GHz self-pulsating laser is used. For a received optical power of -15 dBm, the regenerator does not exhibit a power penalty in BER while reducing the amplitude noise and timing jitter. The regenerator is shown to provide an improvement when subsequent noise is added after regeneration. In addition, the cascadability of the regenerator has been demonstrated using a re-circulating loop with 80 km regenerator spacing by transmitting a 40 Gb/s RZ-OOK signal over 100 loops (8,000 km) with a power penalty of 1.2 dB.

Chapter 5

Quantum-Dot Laser and Its Application

Recently, quantum-dot Fabry P erot (QD-FP) lasers have been drawing much interest. In comparison to either bulk or quantum-well active layer mode-locked semiconductor lasers, a QD-FP laser exhibits a much narrower beat spectrum linewidth [116, 137]. For passively mode-locked lasers, a narrow beat spectrum linewidth accounts for a small amount of intrinsic phase noise in the self-pulsating (SP) emission and strong filtering of high frequency phase noise. A significant reduction in the timing jitter of the recovered clock signal has been achieved at 40 Gb/s by using a mode-locked QD-FP laser [116]. This makes the QD-FP laser a promising candidate for all-optical clock recovery for the 3R regenerator at 40 Gb/s. However, since the emission spectrum exhibits multiple modes, the QD-FP laser cannot be used directly in a conventional 3R regenerator where the data signal is used as the pump signal for a nonlinear optical gate to modulate the recovered clock signal. The multimode spectrum would preclude

the use of wavelength division multiplexing (WDM) and limit the transmission distance due to chromatic dispersion (CD).

The regenerator considered in this thesis uses an SP laser for clock recovery and XPM in a HNLF for retiming. In the retiming stage, the recovered clock signal serves as the pump signal to induce XPM on the data signal and an offset filter is used to produce a retimed signal. In contrast to a conventional nonlinear optical gate, this scheme does not use the clock signal for transmission. Therefore, this approach can take advantage of the low timing jitter of the clock signal obtained from a QD-FP laser and accommodate the multimode spectrum of the laser.

In this chapter, the application of the QD-FP laser to all-optical 3R regeneration is briefly investigated. In section 5.1, the regenerator utilizing the QD-FP laser is described and the change in parameter values is discussed. In section 5.2 the performance of the regenerator is evaluated and a summary is given in section 5.3.

5.1 Redesign of the regenerator

5.1.1 Quantum-dot Fabry Pérot laser

The single-section QD-FP laser used in the experiment has a quantum-dot active layer on an InP substrate, with a cavity length of about $1060 \mu\text{m}$ [28]. Fig. 5.1 shows the optical spectrum for the free-running laser biased at a DC current of 180 mA. The optical spectrum is centered around 1528 nm and the laser has more than thirty modes within the 3-dB bandwidth of 9.3 nm. Due to the broad spectrum, stimulated Brillouin scattering (SBS) does not occur in the XPM-HNLF and the phase modulation

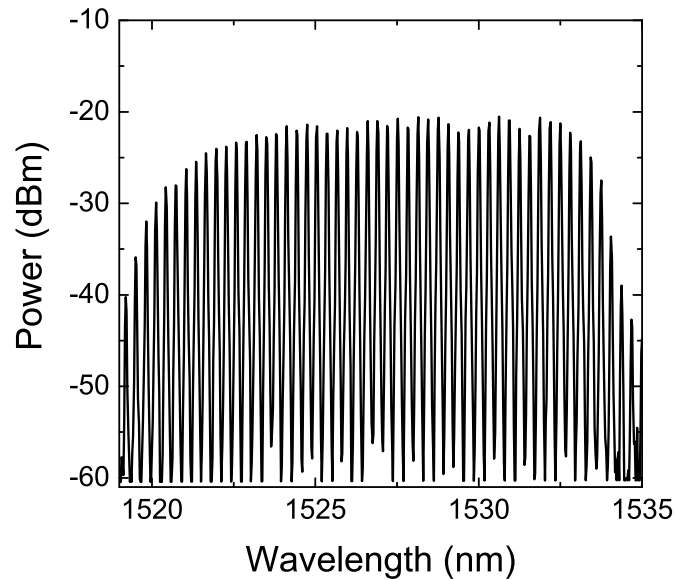


Figure 5.1: Optical spectrum of the quantum-dot laser (resolution bandwidth of 0.06 nm).

is not required to reduce SBS. Fig. 5.2 shows the RF spectrum of the free-running laser. The passive mode-locking yields a SP frequency of 39.803 GHz. The measured locking range is about 5 MHz. The narrow 3 dB RF spectrum linewidth of 80 kHz implies a strong phase correlation among the laser modes. An eye diagram of the recovered clock signal (input signal OSNR of 40 dB) is inset in the figure.

5.1.2 Retiming stage

Since the QD-FP laser replaces the previous SP laser, it is necessary to adjust a few parameters in the retiming stage. First, the length of the XPM-HNLF was reduced to 2 km due to the shorter walk-off length. As shown in Fig. 4.6, the total group delay between data (1545 nm) and clock (1528 nm) signals for 3 km of XPM-HNLF

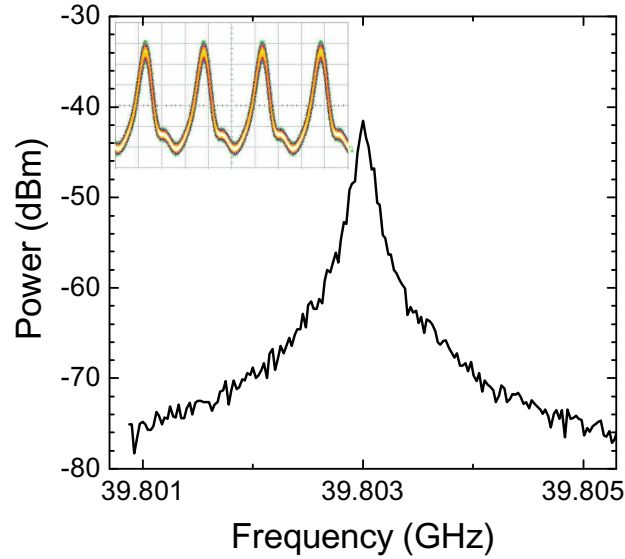


Figure 5.2: RF spectrum of the free-running quantum-dot laser (resolution bandwidth of 10 kHz). Eye diagram of the recovered clock signal is inset in the figure (time base = 5 ps/div).

is about 16 ps which is much longer than the pulse width of the data signal (10 ps). If we assume the clock pulse width is 12.5 ps (FWHM), the walk-off length is found to be 1.41 km. Thus, the length of XPM-HNLF was reduced to 2 km. The depolarized Raman pump signal at 1425 nm provided a gain large enough for the clock signal at 1528 nm and 2 km of XPM-HNLF was long enough to induce XPM on the data signal. Second, the phase modulator was removed from the retiming stage. We observed no SBS in the experiment since the QD-FP laser produced an optical clock signal with a broad bandwidth and a low spectral peak power. Thus, phase modulation of the clock signal was not necessary while it was indispensable for the previous experiments with single or dual mode lasers. Last, the filter offset ($\Delta\lambda_{\text{off}1}$) was increased to -1.0 nm for the retiming stage. The XPM induced spectral broadening was broad enough with 2

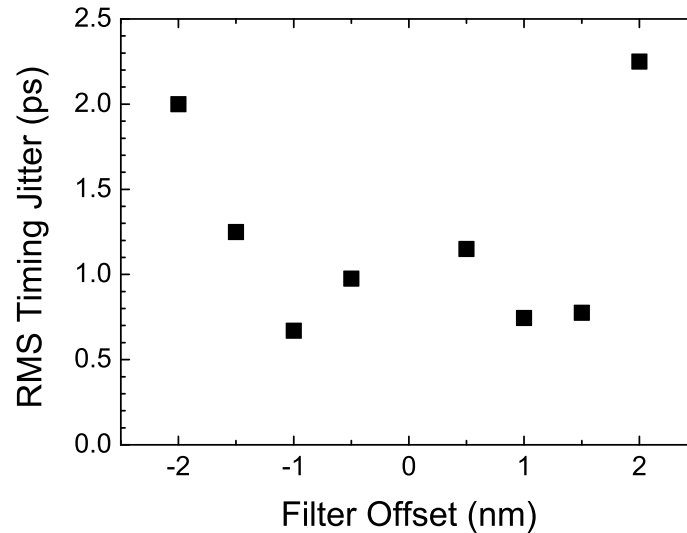


Figure 5.3: Dependence of the RMS timing jitter of the retimed signal on the filter offset.

km of the XPM-HNLF to achieve a larger offset.

Fig. 5.3 shows the dependence of the RMS timing jitter of the retimed signal on the filter offset ($\Delta\lambda_{\text{off1}}$) in the retiming stage. The timing jitter is minimum at offsets of around ± 1.0 nm. The optimum offset for the retiming stage (-1 nm) is similar to that for the reshaping stage (around ± 1.5 nm as shown in Fig. 4.9).

5.2 Performance of the regenerator

Fig. 5.4 shows the setup for 40 Gb/s all-optical 3R regeneration using the QD-FP laser. A RZ-OOK signal at 1545 nm ($2^{31} - 1$ PRBS) was generated with a pulse width of 10 ps. An optical bandpass filter (1.3 nm bandwidth) centered at 1528 nm was used after the optical circulator to eliminate the data signal reflected from the

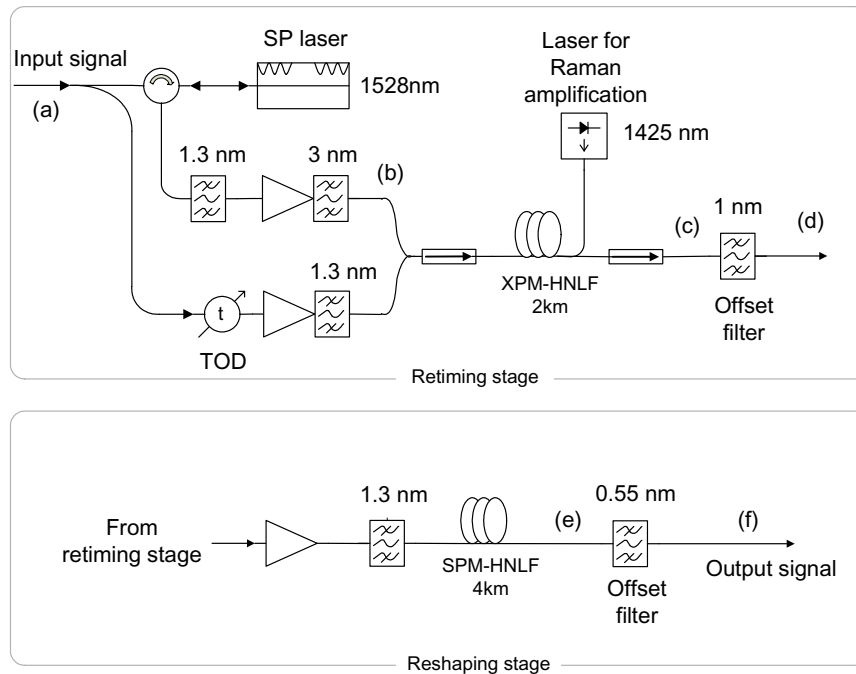


Figure 5.4: Block diagram of the regenerator using the quantum-dot laser.

QD-FP laser. The bandwidth of the optical filter should be wide enough so that the clock signal contains many modes to effectively suppress SBS. The recovered clock signal and the data signal were coupled into a 2 km XPM-HNLF (nonlinearity of $10.6 \text{ W}^{-1}\text{km}^{-1}$, attenuation of 0.76 dB/km , and dispersion of -0.05 ps/nm-km at 1550 nm). A tunable optical delay (TOD) was used to adjust the relative time delay between the clock and data pulses thereby balancing the timing jitter of the rising and falling edges of the retimed signal. The clock signal was used as a pump signal to induce XPM on the data signal. The input powers to the XPM-HNLF for the clock and data signals were 16.3 dBm and 8.9 dBm , respectively. A counter propagating Raman pump signal at 1425 nm with an input power of 26.8 dBm was employed to increase the XPM induced spectral broadening. In this case, single Raman pump signal was

good enough to provide gains for both the data and clock signals. At the output of the XPM-HNLF in the retiming stage, an offset filter (1.0 nm bandwidth) centered at 1544 nm ($\Delta\lambda_{\text{off1}} = -1$ nm) sliced a portion of the XPM broadened spectrum while eliminating the clock signal. In the reshaping stage, the retimed signal was boosted to a power of 21 dBm to cause SPM induced spectral broadening in a 4 km SPM-HNLF (nonlinearity of $10.6 \text{ W}^{-1}\text{km}^{-1}$, attenuation of 0.76 dB/km, and dispersion of -0.21 ps/nm-km at 1550 nm). For an offset filter (0.55 nm bandwidth) centered at 1545 nm, the output signal had the same wavelength as the input signal with a pulse width of 10 ps. Table 5.1 summarizes the parameters used for the regenerator.

Table 5.1: Regenerator parameters with a QD-FP laser for a 40 Gb/s signal.

Retiming stage	Parameter	Value
Data signal	Wavelength	1545 nm
	Input power to XPM-HNLF	8.9 dBm
	Pulse width	10 ps (FWHM)
	PRBS pattern length	$2^{31} - 1$
Clock signal	Wavelength	1528 nm
	Input power to XPM-HNLF	16.3 dBm
Raman pump signal	Wavelength	1425 nm
	Pump power	26.8 dBm
XPM-HNLF	Length	2 km
	Nonlinearity	$10.6 \text{ W}^{-1}\text{km}^{-1}$
	Dispersion	-0.05 ps/nm/km
	Dispersion slope	$0.017 \text{ ps/nm}^2/\text{km}$
Offset filter	Offset ($\Delta\lambda_{\text{off1}}$)	-1.0 nm
	Bandwidth	1.0 nm
Reshaping stage	Parameter	Value
Data signal	Wavelength	1544 nm
	Input power to SPM-HNLF	21.0 dBm
SPM-HNLF	Length	4 km
	Nonlinearity	$10.6 \text{ W}^{-1}\text{km}^{-1}$
	Dispersion	-0.21 ps/nm/km
	Dispersion slope	$0.017 \text{ ps/nm}^2/\text{km}$
Offset filter	Offset($\Delta\lambda_{\text{off2}}$)	1.0 nm
	Bandwidth	0.55 nm

Fig. 5.5 shows the optical spectra of the data signal at different stages of the 3R regenerator (Refer to Fig. 5.4). Fig. 5.5(a) and (b) are the input signal and the recovered clock signal, respectively. Fig. 5.5(c) and (d) are spectra after the XPM-HNLF and the offset filter in the retiming stage, respectively. As shown in Fig. 5.5(c), the clock signal contained many modes with a wide bandwidth. Fig. 5.5(e) and (f) are spectra after the SPM-HNLF and the offset filter in the reshaping stage, respectively. Fig. 5.6 shows the experimental setup for a 40 Gb/s RZ-OOK signal at 1545 nm ($2^{31} - 1$ PRBS) with a pulse width of 10 ps. The OSNR of the input data signal was adjusted using a broad band source (BBS) and a variable optical attenuator (VOA). A polarization scrambler was not used because the quantum-dot laser was not polarization independent. Although there are techniques to make the clock recovery module polarization-insensitive at the cost of added complexity [118], it is not considered in the evaluation of the regenerator performance. The degraded signal was then applied to the regenerator. At the output of the regenerator, the signal was applied to a pre-amplified receiver that consisted of a VOA, EDFA and optical receiver. By varying the input signal OSNR, the Q-factor and timing jitter of the input data signal were adjusted. The improvement in the Q-factor (measured with a sampling oscilloscope) of the regenerated signal is shown in Fig. 5.7. For input signals with an OSNR of less than 30 dB (noise bandwidth of 0.1 nm), the Q-factor is improved. Fig. 5.8 shows the corresponding eye diagrams for several OSNR values. The regenerator suppresses noise for both the one and zero levels.

Fig. 5.9 shows the dependence of the RMS timing jitter of the regenerated signal on the input signal timing jitter. The regenerator effectively reduces the timing jitter when the input signal timing jitter is larger than 500 fs. For the input signal timing

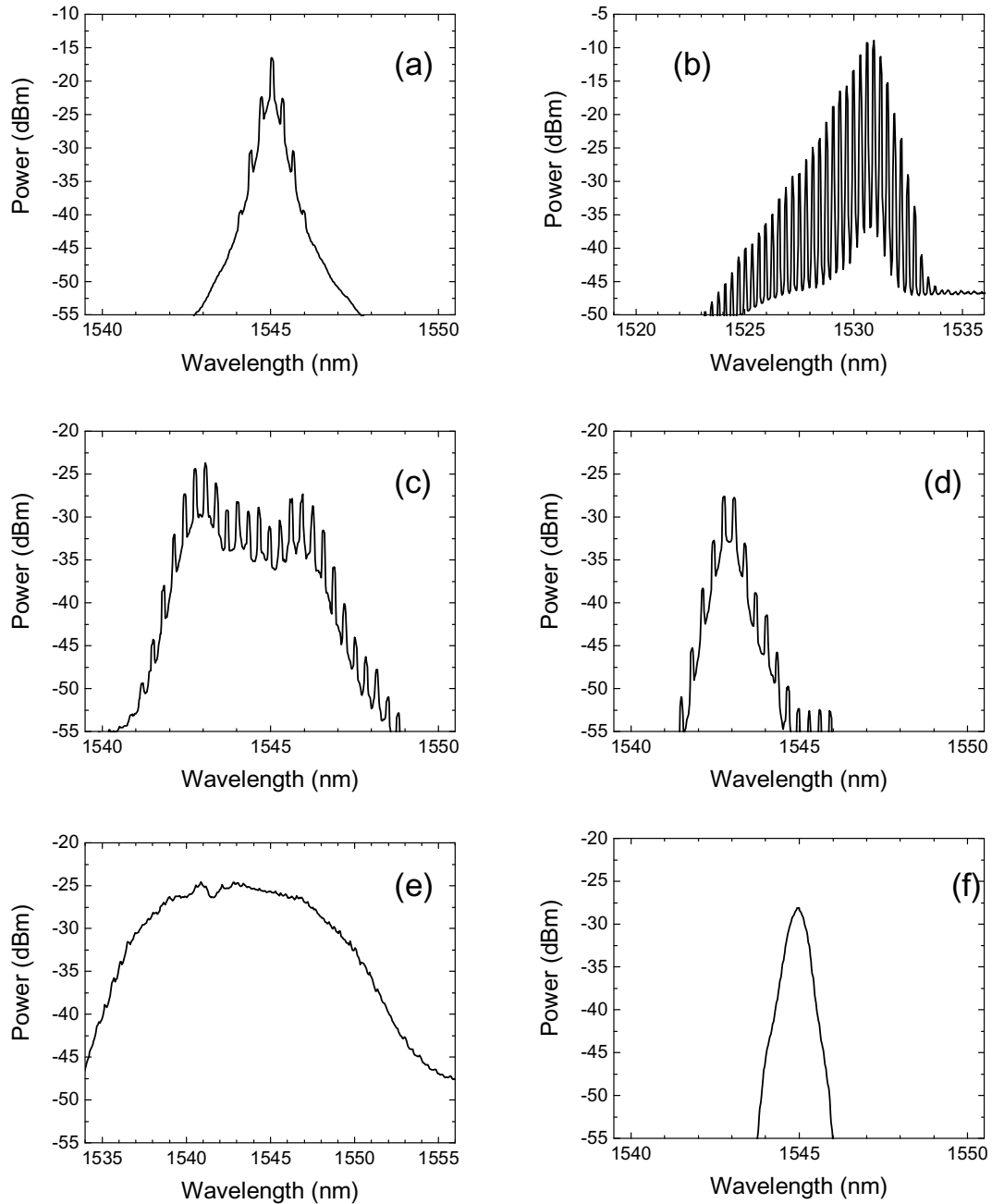


Figure 5.5: Optical spectra at several locations in the regenerator; (a) input signal, (b) clock signal (c) after XPM-HNLF, (d) after retiming stage, (e) after SPM-HNLF, (f) after reshaping stage (refer to Fig. 5.4).

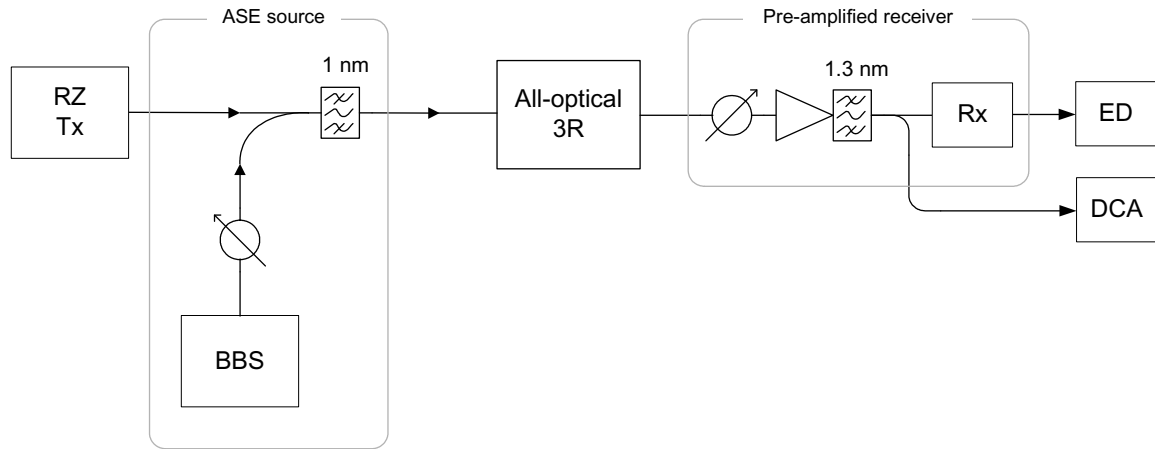


Figure 5.6: Experimental setup of the regenerator using the quantum-dot laser.

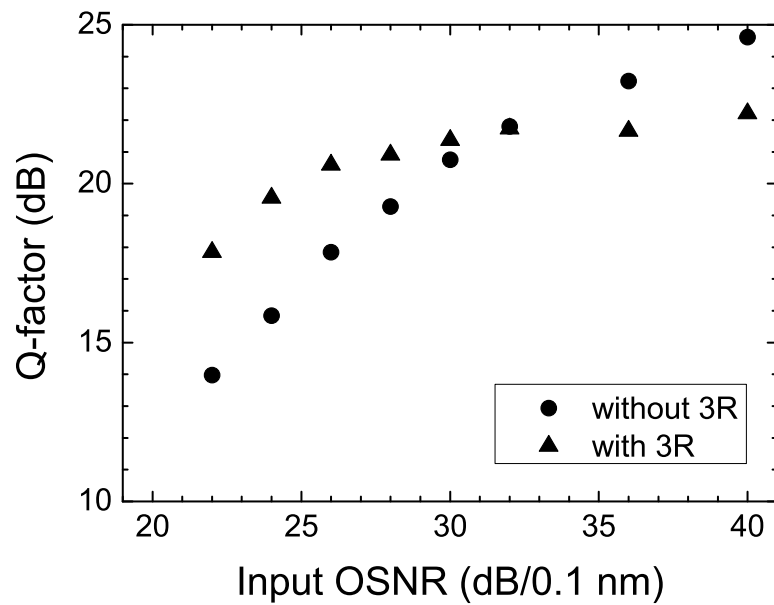


Figure 5.7: Dependence of the Q-factor on the input signal OSNR of the regenerator using the QD-FP laser.

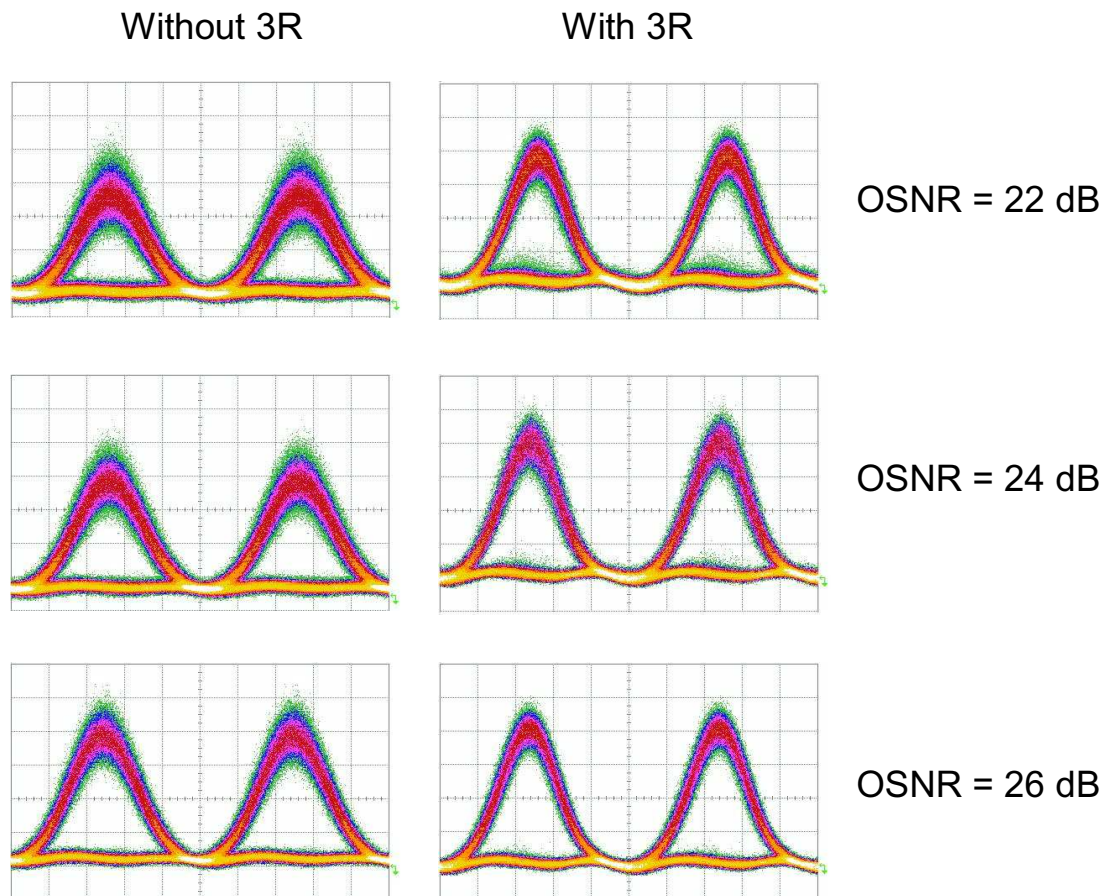


Figure 5.8: Eye diagrams without and with the regenerator using the QD-FP laser (time base = 5 ps/div).

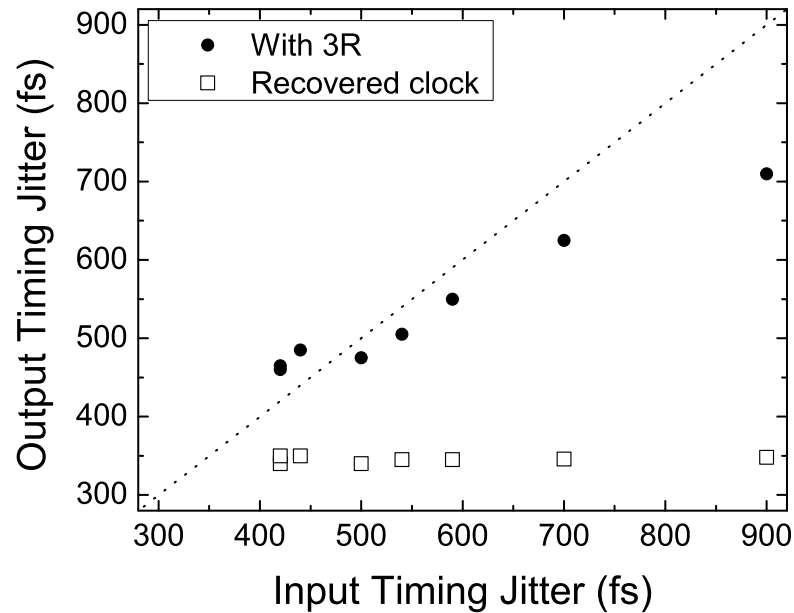


Figure 5.9: Dependence of the output signal RMS timing jitter on the input signal timing jitter of the regenerator using the QD-FP laser.

jitter of 900 fs, the output signal timing jitter is less than 720 fs. As shown in Fig. 5.9, the timing jitter of the recovered clock signal is 350 fs and does not change appreciably as the input signal timing jitter increases from 400 fs to 900 fs. Some amount of amplitude jitter is transferred from the input data signal to the regenerated signal. This amplitude jitter affects the oscilloscope measurement of the timing jitter and contributes to the larger timing jitter for the regenerated signal compared to the recovered clock signal.

Fig. 5.10 shows the dependence of the BER on the input signal OSNR. For a ROP of -15 dBm, there is no BER penalty due to the regenerator. To illustrate the improvement offered by the regenerator, subsequent noise is added after regeneration. To add subsequent noise, the input signal power to the pre-amplifier is decreased to add

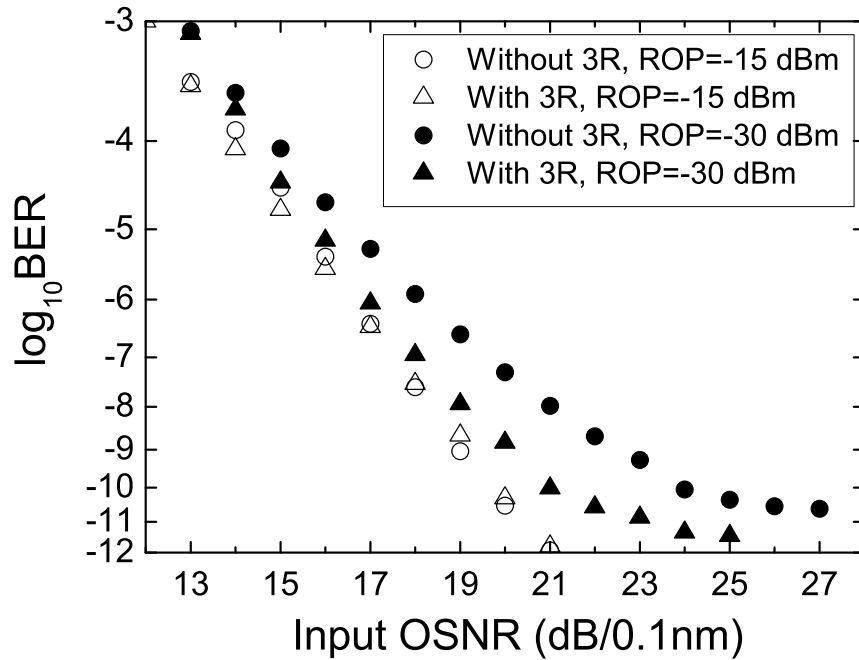


Figure 5.10: Dependence of the BER on the input signal OSNR of the regenerator with the ROPs of -15 dBm and -30 dBm.

receiver noise. The BER was measured for a ROP of -30 dBm. A 2.5 dB improvement in the required OSNR at a BER of 10^{-9} is obtained with the regenerator. The BER floors are due to the noise added in the pre-amplified receiver.

5.3 Summary

We have demonstrated the application of a passively mode-locked quantum-dot Fabry P erot (QD-FP) laser to a wavelength-preserving all-optical 3R regenerator at 40 Gb/s. Since it is a multi mode laser with wide spectral width, stimulated Brillouin scattering of the clock signal was not observed and phase modulation was not necessary. The RMS timing jitter of the recovered clock signal is below 350 fs for the input signal timing jitter up to 900 fs. The regenerator is shown to reduce amplitude noise and timing jitter while it does not cause a power penalty in BER measurement.

Chapter 6

Conclusions

6.1 Summary and contributions

In this thesis, a wavelength-preserving polarization-insensitive all-optical 3R regenerator has been characterized with the following contributions;

1. Wavelength-preserving regeneration is achieved by using Raman amplification in the retiming stage. In the previous demonstration of this regenerator, the retiming and reshaping stages were separately optimized and the wavelength of the input data signal was not preserved. In order to preserve the wavelength, the polarization independent wavelength for XPM, and hence the filter offset in the retiming stage, had to be shifted farther away from the center wavelength of the input data signal. As the clock power was increased to shift the polarization-insensitive wavelength farther, an increased dependency on the input signal SOP was observed. By counter-propagating a depolarized Raman pump signal in the XPM-HNLF, the XPM efficiency can be increased without significantly increasing

the dependency of the SOP of the input data signal. As a result, polarization-insensitive retiming has been achieved at an offset large enough and the input data signal wavelength is preserved after the regenerator.

2. The cascadability of the regenerator has been demonstrated using a recirculating loop for a 10 Gb/s signal. The Q-factor was over 20 dB over 18,000 km. The ultimate performance measure for the regenerator is the BER measurement in a recirculating loop. With a regenerator spacing of 240 km, a 10 Gb/s signal was transmitted over 18,000 km (75 loops) with a power penalty of 1.6 dB compared to the back-to-back case at a BER of 10^{-9} .
3. The regeneration scheme is demonstrated at a bit rate of 40 Gb/s. A phase controlled mode beating laser self-pulsating at 40 GHz was used to recover the clock signal and key regenerator parameters were redesigned. For the retiming stage, signal walk-off had a non-negligible effect on the XPM process and reduced XPM efficiency. For the reshaping stage, the dispersion of the HNLF was adjusted to obtain a high quality output signal. The regenerator at 40 Gb/s is shown to suppress the amplitude noise and timing jitter and does not cause a BER penalty.
4. The cascadability of the regenerator has been demonstrated using a recirculating loop for a 40 Gb/s signal. The Q-factor was over 17 dB up to 12,000 km with a regenerator spacing of 80 km. In the BER measurement, a 40 Gb/s signal was transmitted over 8,000 km (100 loops) with a power penalty of 1.2 dB at a BER of 10^{-9} .

5. A quantum-dot Fabry Pérot (QD-FP) laser has been used for the all-optical clock recovery in a 40 Gb/s regenerator with a fixed SOP of the input data signal. Although the QD-FP laser is able to produce high quality clock signal with very low timing jitter, it has not yet been widely used in communication systems due to its wide spectral width (i.e., a multimode laser). The proposed regeneration technique uses the clock signal to induce XPM on the data signal and the clock signal is not transmitted over the next span. This makes the QD-FP laser a good candidate for the clock recovery of the regenerator. Furthermore, since it is a multimode laser with a wide spectral width, stimulated Brillouin scattering (SBS) was not observed at the output of the HNLFF, which eliminates the need for phase modulation to reduce SBS. No negative effect on the XPM efficiency is observed compared to the single or dual mode self-pulsating laser.

6.2 Conclusions

A wavelength-preserving polarization-insensitive all optical 3R regenerator has been characterized and demonstrated for 10 and 40 Gb/s return to zero on-off keyed signals with practical pulse widths (duty cycle of 33~43%). The proposed regenerator can suppress amplitude noise in the one and zero levels as well as timing jitter while not causing a BER penalty. A recirculating loop experiment verified the cascadability of the regenerator for both 10 and 40 Gb/s signals. In addition, a quantum dot-Fabry Pérot laser has been used to recover the clock signal in the context of all-optical regeneration. The regeneration scheme is applicable to bit rates of 100 - 160 Gb/s provided a low-jitter self-pulsating laser is available and the retiming and reshaping

stages can be co-designed for wavelength-preserving operation.

6.3 Future work

The all-optical 3R regenerator proposed in this thesis meets many requirements necessary for practical applications. The features of the regenerator are described as wavelength-preserving, polarization-insensitive, cascadable, and bit rate scalable with a practical pulse width. However the proposed regenerator is a per-channel device. In order for the regenerator to be a stronger candidate for practical use, multi-channel regeneration is desired. The retiming stage has a potential to realign multiple data signals in time using one clock signal provided the inter channel interference in the HNLF can be managed. For the reshaping stage, some research groups have shown that the SPM based regenerator can regenerate 2-4 channels simultaneously [9, 12].

In addition to multi-channel regeneration, further research on the quantum-dot Fabry P erot (QD-FP) laser based regenerator might be worth pursuing. In the experiment, the SOP of the input data signal was fixed because the QD-FP laser is sensitive to the SOP of the input data signal. One might want to investigate techniques to achieve the polarization-insensitive clock recovery with the QD-FP laser to make the overall regenerator polarization-insensitive.

Another possible direction would be making the regenerator more compact. Different nonlinear fibers [138, 139] or waveguides [140] with very high nonlinearity may allow the regenerator to fit into a smaller package.

Bibliography

- [1] K. Lee and T. Aprille, "SONET evolution: the challenges ahead," in *Global Telecommunications Conference*, 1991, pp. 736–740.
- [2] R. Ballart and Y.-C. Ching, "SONET: now it's the standard optical network," *IEEE Communications Magazine*, vol. 27, no. 3, pp. 8–15, 1989.
- [3] N. Sandesara, G. Ritchie, and B. Engel-Smith, "Plans and considerations for SONET deployment," *IEEE Communications Magazine*, vol. 28, no. 8, pp. 26–33, 1990.
- [4] D. V. Plant, "Agile all-photonics networks," in *Proc. IEEE Laser and Electro Optic Society, Annual Meeting*, 2003, p. 227.
- [5] G. V. Bochmann, T. Hall, O. Yang, M. J. Coates, L. Mason, and R. Vickers, "The agile all-photonics network: an architectural outline," in *Proc. 22nd. Biennial Symposium on Communications*, 2004.
- [6] C. Ito, I. Monfils, and J. C. Cartledge, "All-optical 3R regeneration using higher-order four-wave mixing with a clock-modulated optical pump signal," in *Proc. IEEE Laser and Electro Optic Society, Annual Meeting*, 2006, pp. 223–224.

- [7] F. Parmigiani, S. Asimakis, N. Sugimoto, F. Koizumi, P. Petropoulos, and D. Richardson, "2R regenerator based on a 2-m-long highly nonlinear bismuth oxide fiber," *Optics Express*, vol. 14, no. 12, pp. 5038–5044, 2006.
- [8] H. Simos, A. Argyris, D. Kanakidis, E. Roditi, A. Ikiades, and D. Syvridis, "Regenerative properties of wavelength converters based on FWM in a semiconductor optical amplifier," *IEEE Photonics Technology Letters*, vol. 15, no. 4, pp. 566–568, 2003.
- [9] L. Provost, P. Petropoulos, and D. J. Richardson, "Optical WDM regeneration: status and future prospects," in *Proc. Optical Fiber Communication*, 2009, p. OWD7.
- [10] M. Vasilyev and T. I. Lakoba, "All-optical multichannel 2R regeneration in a fiber-based device," *Optics Express*, vol. 30, no. 12, pp. 1458–1460, 2005.
- [11] C. Kouloumentas, P. Vorreau, L. Provost, P. Petropoulos, W. Freude, J. Leuthold, and I. Tomkos, "All-fiberized dispersion-managed multichannel regeneration at 43 Gb/s," *IEEE Photonics Technology Letters*, vol. 20, no. 22, pp. 1854–1856, 2008.
- [12] F. Parmigiani, P. Vorreau, L. Provost, K. Mukasa, M. Takahashi, M. Tadakuma, P. Petropoulos, D. J. Richardson, W. Freude, and J. Leuthold, "2R regeneration of two 130 Gbit/s channels within a single fiber," in *Proc. Optical Fiber Communication*, 2009, p. JThA56.
- [13] F. Parmigiani, "Multi-wavelength all-optical regeneration techniques," in *Proc. IEEE Photonics Society, Summer Topicals*, 2009, p. TuC4.1.

- [14] Z. Zhu, M. Funabashi, Z. Pan, L. Paraschis, D. L. Harris, and S. J. B. Yoo, "High-performance optical 3R regeneration for scalable fiber transmission system applications," *IEEE Journal of Lightwave Technology*, vol. 25, no. 2, pp. 504–511, 2007.
- [15] L. B. M. Gay and J. C. Simon, "Cascadability and wavelength tunability assessment of a 2R regeneration device based on saturable absorber and semiconductor optical amplifier," in *Proc. Optical Fiber Communication*, 2006, p. OThB1.
- [16] A. Mecozzi and J. Mork, "Saturation effects in nondegenerate four-wave mixing between short optical pulses in semiconductor laser amplifiers," *IEEE Selected Topics in Quantum Electronics*, vol. 3, no. 5, pp. 1190–1207, 1997.
- [17] P. Guerber, B. Lavigne, and O. Leclerc, "Ultimate performance of SOA-based interferometer as decision element in 40 Gbit/s all-optical regenerator," in *Proc. Optical Fiber Communication*, 2002, p. ThGG100.
- [18] A. Mecozzi and J. Mork, "Saturation induced by picosecond pulses in semiconductor optical amplifiers," *Journal of Optical Society of America B*, vol. 14, no. 4, pp. 761–770, 1997.
- [19] A. D'Errico, G. Contestabile, R. Proietti, M. Presi, E. Ciaramella, L. Bramerie, M. Gay, S. Lobo, M. Joindot, J. C. Simon, D. Massoubre, H. T. Nguyen, and J.-L. Oudar, "2R optical regeneration combining XGC in a SOA and a saturable absorber," in *Proc. Optical Fiber Communication*, 2008, p. OWK4.

- [20] J. Leuthold, B. Mikkelsen, R. E. Behringer, G. Raybon, C. H. Joyner, and P. A. Besse, "Novel 3R regenerator based on semiconductor optical amplifier delayed-interference configuration," *IEEE Photonics Technology Letters*, vol. 13, no. 8, pp. 860–862, 2001.
- [21] T. Silveira, A. Teixeira, N. Kataoka, A. Ferreira, N. Wada, X. Wang, T. Miyazaki, and P. Monteiro, "MZI-SOA-based 2R regeneration of OCDMA signals with multiaccess interference noise," *Microwave and Optical Technology Letters*, vol. 50, no. 6, pp. 1521–1523, 2008.
- [22] S. Vehovc, M. Vidmar, and A. Paoletti, "80 Gbit/s optical clock recovery with automatic lock acquisition using electrical phase-locked loop," *Electronics Letters*, vol. 39, no. 8, pp. 673–674, 2002.
- [23] S. Arahira and Y. Ogawa, "Electrical clock recovery based on all-optical signal processing in a monolithic passively mode-locked laser diode," *IEEE Photonics Technology Letters*, vol. 18, no. 16, pp. 1765–1767, 2006.
- [24] Z. Hu, K. Nishimura, H.-F. Chou, L. Rau, M. Usami, J. E. Bowers, and D. J. Blumenthal, "40-Gb/s optical packet clock recovery with simultaneous reshaping using a traveling-wave electroabsorption modulator-based ring oscillator," *IEEE Photonics Technology Letters*, vol. 16, no. 12, pp. 2640–2642, 2004.
- [25] S. R. Han, C. N. Chuang, and S. I. Liu, "A time-constant calibrated phase-locked loop with a fast-locked time," *IEEE Transactions on Circuits and Systems II: Express Briefs*, vol. 54, no. 1, pp. 34–37, 2007.

- [26] T. von Lerber, S. Honkanen, A. Tervonen, H. Ludvigsen, and F. Kuppens, "Optical clock recovery methods: Review," *Optical Fiber Technology*, vol. 15, no. 4, pp. 363–372, 2009.
- [27] M. Möhrle, B. Sartorius, C. Bornholdt, S. Bauer, O. Brox, A. Sigmund, R. Steingrüber, M. Radziunas, and H.-J. Wünsche, "Detuned grating multisection-RW-DFB lasers for high-speed optical signal processing," *IEEE Selected Topics in Quantum Electronics*, vol. 7, no. 2, pp. 217–223, 2001.
- [28] F. Lelarge, B. Rousseau, B. Degens, F. Pommereau, and A. Accard, "Room temperature continuous-wave operation of buried ridge stripe lasers using InAs-InP (100) quantum dots as active core," *IEEE Photonics Technology Letters*, vol. 17, no. 7, pp. 1369–1371, 2005.
- [29] M. Jinno and T. Matsumoto, "Optical tank circuits used for all-optical timing recovery," *IEEE Journal of Quantum Electronics*, vol. 28, no. 4, pp. 895–900, 2002.
- [30] K. Taira and K. Kikuchi, "All-optical clock recovery using a mode-locked laser," *Electronics Letters*, vol. 28, no. 19, pp. 1814–1816, 1992.
- [31] B. Sartorius, M. Möhrle, S. Malchow, and S. Reichenbacher, "Wavelength and polarisation independent all optical synchronisation of high frequency DFB type self-pulsations," *Electronics Letters*, vol. 32, no. 11, pp. 1026–1028, 1996.
- [32] B. Sartorius, M. Möhrle, S. Reichenbacher, H. Preier, H.-J. Wünsche, and U. Bandelow, "Dispersive self-Q switching in self-pulsating DFB lasers," *IEEE Journal of Quantum Electronics*, vol. 33, no. 2, pp. 211–218, 1997.

- [33] C. Johnson, K. Demarest, C. Allen, R. Hui, K. V. Peddanarappagari, and B. Zhu, "Multiwavelength all-optical clock recovery," *IEEE Photonics Technology Letters*, vol. 11, no. 7, pp. 895–897, 1999.
- [34] C. Bintjas, K. Yiannopoulos, N. Pleros, G. Theophilopoulos, M. Kalyvas, H. Avramopoulos, and G. Guekos, "Clock recovery circuit for optical packets," *IEEE Photonics Technology Letters*, vol. 14, no. 9, pp. 1363–1365, 2002.
- [35] N. Pleros, K. Vysokinos, C. Bintjas, K. Yiannopoulos, K. Vlachos, and H. Avramopoulos, "All-optical clock recovery from short asynchronous data packets at 10 Gb/s," *IEEE Photonics Technology Letters*, vol. 15, no. 9, pp. 1291–1293, 2003.
- [36] R. Salem and T. E. Murphy, "Broad-band optical clock recovery system using two-photon absorption," *IEEE Photonics Technology Letters*, vol. 16, no. 9, pp. 2141–2143, 2004.
- [37] E. Kehayas, L. Stampoulidis, H. Avramopoulos, Y. Liu, E. Tangdionga, and H. Dorren, "40 Gb/s all-optical packet clock recovery with ultrafast lock-in time and low inter-packet guardbands," *Optics Express*, vol. 13, no. 2, pp. 475–480, 2005.
- [38] T. von Lerber, J. Tuominen, H. Ludvigsen, S. Honkanen, and F. Kueppers, "Multichannel and rate all-optical clock recovery," *IEEE Photonics Technology Letters*, vol. 18, no. 12, pp. 1395–1397, 2006.

- [39] D. Pudo, M. Depa, and L. Chen, "Single and multiwavelength all-optical clock recovery in single-mode fiber using the temporal Talbot effect," *IEEE Journal of Lightwave Technology*, vol. 25, no. 10, pp. 2898–2903, 2007.
- [40] J. Renaudier, R. Brenot, B. Degens, B. Rousseau, F. Poingt, O. Legouezigou, F. Pommereau, A. Accard, P. Gallion, and G.-H. Duan, "45 GHz self-pulsation with narrow linewidth in quantum dot Fabry-Perot semiconductor lasers at 1.5 μm ," *Electronics Letters*, vol. 41, no. 18, pp. 1007–1007, 2005.
- [41] T. Otani, T. Miyazaki, and S. Yamamoto, "40-Gb/s optical 3R regenerator using electroabsorption modulators for optical networks," *IEEE Journal of Lightwave Technology*, vol. 20, no. 2, pp. 195–200, 2002.
- [42] H. F. Chou and J. E. Bowers, "Simplified optoelectronic 3R regenerator using nonlinear electro-optical transformation in an electroabsorption modulator," *Optics Express*, vol. 13, no. 7, pp. 2742–2746, 2005.
- [43] L. Huo, Y. Yang, Y. Nan, C. Lou, and Y. Gao, "A study on the wavelength conversion and all-optical 3R regeneration using cross-absorption modulation in a bulk electroabsorption modulator," *IEEE Journal of Lightwave Technology*, vol. 24, no. 8, pp. 3035–3044, 2006.
- [44] S. Hofeldt, S. Bischoff, and J. Mork, "All-optical wavelength conversion and signal regeneration using an electroabsorption modulator," *IEEE Journal of Lightwave Technology*, vol. 18, no. 8, pp. 195–200, 2000.

- [45] K. Nishimura, R. Inohara, M. Usami, and S. Akiba, "All-optical wavelength conversion by electroabsorption modulator," *IEEE Selected Topics in Quantum Electronics*, vol. 11, no. 1, pp. 278–284, 2000.
- [46] L. Billès, J. C. Simon, B. Kowalski, M. Henry, G. Michaud, P. Lamouler, and F. Alard, "20 Gbit/s optical 3R regenerator using SOA based Mach-Zehnder interferometer gate," in *Proc. European Conference on Optical Communication*, 1997, pp. 269–272.
- [47] B. Lavigne, D. Chiaroni, P. Guerber, L. Hamon, and A. Jourdan, "Improvement of regeneration capabilities in semiconductor optical amplifier-based 3R regenerator," in *Proc. Optical Fiber Communication*, 1999, pp. 128–130.
- [48] A. E. Kelly, I. D. Phillips, R. J. Manning, A. D. Ellis, D. Nettet, D. G. Moodie, and R. Kashyap, "80 Gbit/s all-optical regenerative wavelength conversion using semiconductor optical amplifier based interferometer," *Electronics Letters*, vol. 35, no. 17, pp. 1477–1478, 1999.
- [49] D. Wolfson, A. Kloch, T. Fjelde, C. Janz, B. Dagens, and M. Renaud, "40-Gb/s all-optical wavelength conversion, regeneration, and demultiplexing in an SOA-based all-active Mach-Zehnder interferometer," *IEEE Photonics Technology Letters*, vol. 12, no. 3, pp. 332–334, 2000.
- [50] Y. Ueno, S. Nakamura, and K. Tajima, "Penalty-free error-free all-optical data pulse regeneration at 84 Gb/s by using a symmetric-Mach-Zehnder-type semiconductor regenerator," *IEEE Photonics Technology Letters*, vol. 13, no. 5, pp. 469–471, 2001.

- [51] R. J. Essiambre, B. Mikkelsen, and G. Raybon, "Semiconductor-based all-optical 3R regenerator demonstrated at 40 Gbit/s," *Electronics Letters*, vol. 40, no. 3, pp. 192–194, 2004.
- [52] Y. A. Leem, D. C. Kim, E. Sim, S. B. Kim, H. Ko, K. H. Park, D. S. Yee, J. O. Oh, S. H. Lee, and M. Y. Jeon, "The characterization of all-optical 3R regeneration based on InP-related semiconductor optical devices," *IEEE Selected Topics in Quantum Electronics*, vol. 12, no. 4, pp. 726–735, 2006.
- [53] J. L. Pleumeekers, M. Kauer, K. Dreyer, C. Burrus, A. G. Dentai, S. Shunk, J. Leuthold, and C. H. Joyner, "Analysis and optimization of SPM-based 2R signal regeneration at 40 Gb/s," *IEEE Photonics Technology Letters*, vol. 14, no. 1, pp. 12–14, 2002.
- [54] S. Hofeldt, S. Bischoff, and J. Mork, "All-optical wavelength conversion by semiconductor optical amplifiers," *IEEE Journal of Lightwave Technology*, vol. 14, no. 6, pp. 942–954, 1996.
- [55] P. S. Cho, D. Mahgerefteh, J. Goldhar, L. G. Joneckis, and G. L. Burdge, "High performance non-interferometric semiconductor-optical-amplifier/fibre-bragg-grating wavelength converter," *Electronics Letters*, vol. 34, no. 4, pp. 371–373, 1998.
- [56] H. Lee, H. Yoon, Y. Kim, and J. Jeong, "Theoretical study of frequency chirping and extinction ratio of wavelength-converted optical signals by XGM and XPM using SOAs," *IEEE Journal of Quantum Electronics*, vol. 35, no. 8, pp. 1213–1219, 1999.

- [57] K. Obermann, S. Kindt, D. Breuer, K. Petermann, C. Schmidt, S. Diez, and H. G. Weber, "Noise characteristics of semiconductor-optical amplifiers used for wavelength conversion via cross-gain and cross-phase modulation," *IEEE Photonics Technology Letters*, vol. 9, no. 3, pp. 312–314, 1997.
- [58] A. Bogris and D. Syvridis, "Regenerative properties of a pump-modulated four-wave mixing scheme in dispersion-shifted fibers," *IEEE Journal of Lightwave Technology*, vol. 21, no. 9, pp. 1892–1902, 2003.
- [59] G. P. Agrawal, *Nonlinear Fiber Optics, Fourth Edition*. Academic Press, 2007.
- [60] K. Inoue, "Optical nonlinearity in optical fibers and semiconductor optical amplifiers," in *Proc. Conference on Lasers and Electro-Optics (CLEO)*, 1999, pp. 1089–1090.
- [61] A. Reale, P. Lugli, and S. Betti, "Format conversion of optical data using four-wave mixing in semiconductor optical amplifiers," *IEEE Selected Topics in Quantum Electronics*, vol. 7, no. 4, pp. 703–709, 2001.
- [62] C. Politi, D. Klonidis, and M. J. OMahony, "Waveband converters based on four-wave mixing in SOAs," *IEEE Journal of Lightwave Technology*, vol. 21, no. 3, pp. 1203–1217, 2006.
- [63] C. Yu, T. Luo, B. Zhang, Z. Pan, M. Adler, Y. Wang, J. E. McGeehan, and A. E. Willner, "Wavelength-shift-free 3R regenerator for 40-Gb/s RZ system by optical parametric amplification in fiber," *IEEE Photonics Technology Letters*, vol. 18, no. 24, pp. 2569–2571, 2006.

- [64] P. Mamyshev, "All-optical data regeneration based on self-phase modulation effect," in *Proc. European Conference on Optical Communication*, vol. 1, 1998, pp. 475–476.
- [65] C. Ito and J. Cartledge, "Polarization independent all-optical 3R regeneration based on the Kerr effect in highly nonlinear fiber and offset spectral slicing," *IEEE Selected Topics in Quantum Electronics*, vol. 14, no. 3, pp. 616–624, 2007.
- [66] M. Rochette, J. L. Blows, and B. J. Eggleton, "3R optical regeneration: An all-optical solution with BER improvement," *Optics Express*, vol. 14, no. 14, pp. 6414–6427, 2006.
- [67] M. Matsumoto, "Performance analysis and comparison of optical 3R regenerators utilizing self-phase modulation in fibers," *IEEE Journal of Lightwave Technology*, vol. 22, no. 6, pp. 1472–1482, 2004.
- [68] ———, "Performance analysis and comparison of optical 3R regenerators utilizing self-phase modulation in fibers," *IEEE Journal of Lightwave Technology*, vol. 22, no. 6, pp. 1472–1482, 2004.
- [69] G. Raybon, Y. Su, J. Leuthold, R. Essiambre, T. Her, C. Joergensen, P. Steinvurzel, and K. Feder, "40 Gbit/s pseudo-linear transmission over one million kilometers," in *Proc. Optical Fiber Communication*, 2002, pp. FD10–1–FD10–3.

- [70] A. Striegler and B. Schmauss, "Analysis and optimization of SPM-based 2R signal regeneration at 40 Gb/s," *IEEE Journal of Lightwave Technology*, vol. 24, no. 7, pp. 2835–2843, 2006.
- [71] M. Aoudeh and J. Cartledge, "Impact of residual dispersion and ASE noise on the performance optimization of all-optical regenerators utilizing self-phase modulation in a highly nonlinear fiber," *IEEE Selected Topics in Quantum Electronics*, vol. 12, no. 4, pp. 717–725, 2006.
- [72] M. R. E. Lamont, M. Rochette, D. J. Moss, and B. J. Eggleton, "Two-photon absorption effects on self-phase-modulation-based 2R optical regeneration," *IEEE Photonics Technology Letters*, vol. 18, no. 10, pp. 1185–1187, 2006.
- [73] L. Fu, M. Rochette, V. Ta'eed, D. Moss, and B. Eggleton, "Investigation of self-phase modulation based optical regeneration in single mode As_2Se_3 chalcogenide glass fiber," *Optics Express*, vol. 13, no. 19, p. 7637, 2005.
- [74] C. Schubert, R. Ludwig, S. Watanabe, E. Futami, C. Schmidt, J. Berger, C. Boerner, S. Ferber, and H. G. Weber, "160 Gbit/s wavelength converter with 3R-regenerating capability," *Electronics Letters*, vol. 38, no. 16, pp. 903–904, 2002.
- [75] S. Watanabe, F. Futami, R. Okabe, Y. Takita, S. Ferber, R. Ludwig, C. Schubert, C. Schmidt, and H. G. Weber, "160 Gbit/s optical 3R-Regenerator in a fiber transmission experiment," in *Proc. Optical Fiber Communication*, 2002, pp. PD16–1 – PD16–3.

- [76] S. Arahira and Y. Ogawa, "160-Gb/s OTDM signal source with 3R function utilizing ultrafast mode-locked laser diodes and modified NOLM," *IEEE Photonics Technology Letters*, vol. 17, no. 5, pp. 992–994, 2005.
- [77] M. S. A. Bogoni, P. Ghelfi and L. Potí, "All-optical regeneration and demultiplexing for 160-Gb/s transmission systems using a NOLM-based three-stage scheme," *IEEE Selected Topics in Quantum Electronics*, vol. 10, no. 1, pp. 92–96, 2004.
- [78] J. Li, B. E. Olsson, M. Karlsson, and P. A. Andrekson, "OTDM demultiplexer based on XPM-induced wavelength shifting in highly nonlinear fiber," *IEEE Photonics Technology Letters*, vol. 15, no. 12, pp. 1770–1772, 2003.
- [79] J. Suzuki, T. Tanemura, K. Taira, Y. Ozeki, and K. Kikuchi, "All-optical regenerator using wavelength shift induced by cross-phase modulation in highly nonlinear dispersion-shifted fiber," *IEEE Photonics Technology Letters*, vol. 17, no. 2, pp. 423–425, 2005.
- [80] S. J. Savage, B. S. Robinson, and S. A. Hamilton, "Wavelength-maintaining polarization-insensitive all-optical 3R regenerator," *Optics Express*, vol. 14, no. 5, pp. 1748–1754, 2006.
- [81] R. Salem, A. S. Lenihan, G. M. Carter, and T. Murphy, "Techniques for polarization-independent cross-phase modulation in nonlinear birefringent fibers," *IEEE Selected Topics in Quantum Electronics*, vol. 14, no. 3, pp. 540–550, 2008.

- [82] A. S. Lenihan, R. Salem, T. E. Murphy, and G. M. Carter, "All-optical 80-Gb/s time-division demultiplexing using polarization-insensitive cross-phase modulation in photonic crystal fiber," *IEEE Photonics Technology Letters*, vol. 18, no. 12, pp. 1329–1331, 2006.
- [83] R. Salem, A. S. Lenihan, G. M. Carter, and T. E. Murphy, "160-Gb/s polarization-independent optical demultiplexing in 2-m nonlinear fiber," *IEEE Photonics Technology Letters*, vol. 18, no. 21, pp. 2245–2247, 2006.
- [84] J. Li, A. Berntson, and G. Jacobsen, "Polarization-independent optical demultiplexing using XPM-induced wavelength shifting in highly nonlinear fiber," *IEEE Photonics Technology Letters*, vol. 20, no. 9, pp. 691–693, 2008.
- [85] W. Astar, C.-C. Wei, Y.-J. Chen, J. Chen, and G. M. Carter, "Polarization-insensitive, 40 Gb/s wavelength and RZ-OOK-to-RZ-BPSK modulation format conversion by XPM in a highly nonlinear PCF," *Optics Express*, vol. 16, no. 16, pp. 12 039–12 049, 2008.
- [86] T. Tanemura, J. Suzuki, K. Katoh, and K. Kikuchi, "Polarization-insensitive all-optical wavelength conversion using cross-phase modulation in twisted fiber and optical filtering," *IEEE Photonics Technology Letters*, vol. 17, no. 5, pp. 1052–1054, 2005.
- [87] C. Ito, S. H. Chung, I. Monfils, and J. C. Cartledge, "Polarization independent all-optical retiming based on cross-phase modulation and spectral slicing," in *Proc. Optical Fiber Communication*, 2007, p. OThB5.

- [88] O. Leclerc, B. Lavigne, E. Balmeffre, P. Brindel, L. Pierre, D. Rouvillain, and F. Segumineau, "Optical regeneration at 40 Gb/s and beyond," *IEEE Journal of Lightwave Technology*, vol. 21, no. 11, pp. 2779–2790, 2003.
- [89] K. Igarashi and K. Kikuchi, "Optical signal processing by phase modulation and subsequent spectral filtering aiming at applications to ultrafast optical communication systems," *IEEE Selected Topics in Quantum Electronics*, vol. 14, no. 3, pp. 551–565, 2008.
- [90] M. Matsumoto, "Efficient all-optical 2R regeneration using self-phase modulation in bidirectional fiber configuration," *Optics Express*, vol. 14, no. 23, pp. 11 018–11 023, 2006.
- [91] M. Matsumoto, Y. Shimada, and H. Sakaguchi, "Wavelength-shift-free SPM-based 2R regeneration by bidirectional use of a highly nonlinear fiber," in *Proc. Optical Fiber Communication*, 2007, p. OME5.
- [92] J. H. Lee, T. Nagashima, T. Hasegawa, S. Ohara, N. Sugimoto, Y.-G. Han, S. B. Lee, and K. Kikuchi, "Output performance investigation of self-phase-modulation-based 2R regenerator using bismuth oxide nonlinear fiber," *IEEE Photonics Technology Letters*, vol. 18, no. 12, pp. 1296–1298, 2006.
- [93] L. B. Fu, M. Rochette, V. G. Taeed, D. J. Moss, and B. J. Eggleton, "Investigation of self-phase modulation based optical regeneration in single mode As_2Se_3 chalcogenide glass fiber," *Optics Express*, vol. 13, no. 19, pp. 7637–7644, 2005.

- [94] T.-H. Her, G. Raybon, and C. Headley, "Optimization of pulse regeneration at 40 Gb/s based on spectral filtering of self-phase modulation in fiber," *IEEE Photonics Technology Letters*, vol. 16, no. 1, pp. 200–202, 2004.
- [95] M. Rochette, L. Fu, V. Taeed, D. J. Moss, and B. J. Eggleton, "2R optical regeneration: an all-optical solution for BER improvement," *IEEE Selected Topics in Quantum Electronics*, vol. 12, no. 4, pp. 736–744, 2006.
- [96] M. Rochette, J. N. Kutz, J. L. Blows, D. Moss, J. T. Mok, and B. J. Eggleton, "Bit-error-ratio improvement with 2R optical regenerators," *IEEE Photonics Technology Letters*, vol. 17, no. 4, pp. 908–910, 2005.
- [97] P. Johannisson and M. Karlsson, "Characterization of a self-phase-modulation-based all-optical regeneration system," *IEEE Photonics Technology Letters*, vol. 17, no. 12, pp. 2667–2669, 2005.
- [98] L. Provost, C. Kouloumentas, F. Parmigiani, S. Tsolakidis, I. Tomkos, P. Petropoulos, and D. J. Richardson, "Experimental investigation of a dispersion-managed multi-channel 2R optical regenerator," in *Proc. Optical Fiber Communication*, 2008, p. OThJ3.
- [99] M. Vasilyev, T. I. Lakoba, and P. G. Patki, "Multi-wavelength all-optical regeneration," in *Proc. Optical Fiber Communication*, 2008, p. OWK3.
- [100] H. Simos, A. Bogris, and D. Syvridis, "Investigation of a 2R all-optical regenerator based on four-wave mixing in a semiconductor optical amplifier," *IEEE Journal of Lightwave Technology*, vol. 22, no. 2, pp. 595–604, 2004.

- [101] E. Ciaramella and S. Trillo, "All-optical signal reshaping via four-wave mixing in optical fibers," *IEEE Photonics Technology Letters*, vol. 12, no. 7, pp. 849–851, 2000.
- [102] A. Bogris and D. Syvridis, "Regenerative properties of a pump-modulated four-wave mixing scheme in dispersion-shifted fibers," *IEEE Journal of Lightwave Technology*, vol. 21, no. 9, pp. 1892–1902, 2003.
- [103] M. Meissner, K. Sponsel, K. Cvecek, A. Benz, S. Weisser, B. Schmauss, and G. Leuchs, "3.9-dB OSNR gain by an NOLM-based 2-R regenerator," *IEEE Photonics Technology Letters*, vol. 16, no. 9, pp. 2105–2107, 2004.
- [104] A. G. Striegler, M. Meissner, K. Cveček, K. Sponsel, G. Leuchs, and B. Schmauss, "NOLM-based RZ-DPSK signal regeneration," *IEEE Photonics Technology Letters*, vol. 17, no. 3, pp. 639–641, 2005.
- [105] Z. Huang, A. Gray, I. Khrushchev, and I. Bennion, "10-Gb/s transmission over 100 Mm of standard fiber using 2R regeneration in an optical loop mirror," *IEEE Photonics Technology Letters*, vol. 16, no. 11, pp. 2526–2528, 2004.
- [106] F. Ohman, S. Bischoff, B. Tromborg, and J. Mork, "Noise and regeneration in semiconductor waveguides with saturable gain and absorption," *IEEE Journal of Quantum Electronics*, vol. 40, no. 3, pp. 245–255, 2004.
- [107] D. Rouvillain, F. Segueineau, L. Pierre, P. Brindel, H. Choumane, G. Aubin, J.-L. Oudar, and O. Leclere, "40Gbit/s optical 2R regenerator based on passive saturable absorber for WDM long-haul transmissions," in *Proc. Optical Fiber Communication*, 2002, pp. FD11–1.

- [108] S. Radic, C. J. McKinstrie, R. M. Jopson, J. C. Centanni, and A. R. Chraplyvy, "All-optical regeneration in one- and two-pump parametric amplifiers using highly nonlinear optical fiber," *IEEE Photonics Technology Letters*, vol. 15, no. 7, pp. 957–959, 2003.
- [109] C. Ito, I. Monfils, and J. C. Cartledge, "All-optical 3R regenerator using higher-order four-wave mixing with a clock-modulated optical pump signal," in *Proc. IEEE Laser and Electro Optic Society, Annual Meeting*, 2006, pp. 223–224.
- [110] T. Yang, C. Shu, and C. Lin, "Depolarization technique for wavelength conversion using four-wave mixing in a dispersion-flattened photonic crystal fiber," *Optics Express*, vol. 13, no. 14, pp. 5409–5415, 2005.
- [111] K. K. Chow, C. Shu, C. Lin, and A. Bjarklev, "Polarization-insensitive widely tunable wavelength converter based on four-wave mixing in a dispersion-flattened nonlinear photonic Crystal fiber," *IEEE Photonics Technology Letters*, vol. 17, no. 3, pp. 624–626, 2005.
- [112] M. Gay, L. Bramerie, H. T. Nguyen, S. Lobo, G. Aubin, Q. T. Le, and M. Join-dot, "Regeneration and cascability assessment of a new passive 2R regenerator based on a dual-stage saturable absorber gate," in *Proc. European Conference on Optical Communication*, 2008, p. Tu.4.D.2.
- [113] C. Bornholdt, B. Sartorius, M. Möhrle, and S. Bauer, "Self-pulsating DFB laser for all-optical clock recovery at 40 Gbit/s," *Electronics Letters*, vol. 36, no. 4, pp. 327–328, 2000.

- [114] H. Wenzel, U. Bandelow, H.-J. Wünsche, and J. Rehberg, "Mechanisms of fast self pulsations in two section DFB lasers," *IEEE Journal of Quantum Electronics*, vol. 32, no. 1, pp. 69–78, 1996.
- [115] H.-J. Wünsche, M. Radziunas, S. Bauer, O. Brox, and B. Sartorius, "Modeling of mode control and noise in self-pulsating PhaseCOMB lasers," *IEEE Selected Topics in Quantum Electronics*, vol. 9, no. 3, pp. 857–864, 2003.
- [116] F. Lelarge, B. Dagens, J. Renaudier, R. Brenot, A. Accard, F. van Dijk, D. Make, O. Le Gouezigou, J.-G. Provost, F. Poingt, J. Landreau, O. Drisse, E. Derouin, B. Rousseau, F. Pommereau, and G.-H. Duan, "Recent advances on InAs/InP quantum dash based semiconductor lasers and optical amplifiers operating at 1.55 μm ," *IEEE Selected Topics in Quantum Electronics*, vol. 13, no. 1, pp. 111–124, 2007.
- [117] B. Lavigne, J. Renaudier, F. Lelarge, O. Legouezigou, H. Gariah, and G.-H. Duan, "Polarization-insensitive low timing jitter and highly optical noise tolerant all-optical 40-GHz clock recovery using a bulk and a quantum-dots-based self-pulsating laser cascade," *IEEE Journal of Lightwave Technology*, vol. 25, no. 1, pp. 170–176, 2007.
- [118] K. Inoue, "Polarization independent wavelength conversion using fiber four-wave mixing with two orthogonal pump lights of different frequencies," *IEEE Journal of Lightwave Technology*, vol. 12, no. 11, pp. 1916–1920, 1994.
- [119] N. Y. Kim, N. Cheng, and J. C. Cartledge, "Optimization of all-optical wavelength converter based on a nonlinear semiconductor optical amplifier and delay

- interferometer,” in *Proc. IEEE Laser and Electro Optic Society, Annual Meeting*, 2006, pp. 225–226.
- [120] C. Ito and J. C. Cartledge, “Design considerations for polarization-independent all-optical retiming based on cross-phase modulation and spectral slicing,” *IEEE Photonics Technology Letters*, vol. 20, no. 6, pp. 425–427, 2008.
- [121] S. Kumar, A. Selvarajan, and G. V. Anand, “Nonlinear copropagation of two optical pulses of different frequencies in birefringent fibers,” *Journal of the Optical Society of America B*, vol. 11, no. 5, pp. 810–817, 1994.
- [122] C. Ito and J. C. Cartledge, “Polarization independent all-optical 3R regeneration of optical packets based on the Kerr effect and offset spectral slicing,” in *Proc. European Conference on Optical Communication*, 2007, p. 5.3.6.
- [123] C. R. S. Fludger, V. Handerek, and R. J. Mears, “Pump to signal RIN transfer in Raman fiber amplifiers,” *IEEE Journal of Lightwave Technology*, vol. 19, no. 8, pp. 1140–1148, 2001.
- [124] I. Monfils, *All-optical clock recovery in a Q-switching self-pulsating DFB laser*, *Ph.D. thesis*. Queen's University, 2007.
- [125] S. Taccheo and L. Boivin, “Investigation and design rules of supercontinuum sources for WDM applications,” in *Proc. Optical Fiber Communication*, 2000, p. ThA1.

- [126] M. Nakazawa, H. Kubota, and K. Tamura, "Random evolution and coherence degradation of a high-order optical soliton train in the presence of noise," *Optics Letters*, vol. 24, no. 5, pp. 318–320, 1999.
- [127] C. Ito, *All-optical 3R regeneration for Agile All-Photonic Networks*, Ph.D. thesis. Queen's University, 2007.
- [128] G. P. Agrawal, *Fiber-Optic Communication Systems*. Wiley-Interscience, 2002.
- [129] D. Derickson, *Fiber Optic Test and Measurement*. Upper Saddle River, NJ: Prentice Hall, 1998.
- [130] L. Provost, C. Finot, K. Mukasa, P. Petropoulos, and D. Richardson, "Generalisation and experimental validation of design rules for self-phase modulation-based 2R-regenerators," in *Proc. Optical Fiber Communication*, 2007, p. OThB6.
- [131] S. H. Chung and J. Cartledge, "Characterizing the noise transfer properties of an all-optical regenerator," in *Proc. Optical Fiber Communication*, 2008, p. OWK6.
- [132] S. H. Chung and J. C. Cartledge, "Wavelength-preserving polarization-insensitive all-optical 3R regenerator utilizing Raman amplification, cross and self-phase modulation, and offset filtering," in *Proc. IEEE Laser and Electro Optic Society, Annual Meeting*, 2008, p. MP1.
- [133] S. H. Chung, X. Tang, and J. C. Cartledge, "Polarization insensitive all-optical retiming based on cross-phase modulation and offset filtering with distributed

- Raman amplification,” in *Proc. European Conference on Optical Communication*, 2008, p. Tu.4.D.5.
- [134] S. H. Chung, X. Tang, and J. Cartledge, “Performance of a polarization-insensitive all-optical 3R regenerator using cross- and self-phase modulation and offset filtering in a recirculating Loop,” in *Proc. Optical Fiber Communication*, 2009, p. OThF2.
- [135] S. K. Korotky, P. B. Hansen, L. Eskildsen, and J. J. Veselka, “Efficient phase modulation scheme for suppressing stimulated Brillouin scattering,” in *Proc. Int. Conf. Integrated Optics and Optical Fibre Communication (IOOC)*, 1995, pp. 110–111.
- [136] Y. Liu, Z. Lü, Y. Dong, and Q. Li, “Research on stimulated Brillouin scattering suppression based on multi-frequency phase modulation,” *Chinese Optics Letters*, vol. 7, no. 1, pp. 29–31, 2009.
- [137] J. Renaudier, G.-H. Duan, P. Landais, and P. Gallion, “Phase correlation and linewidth reduction of 40 GHz self-pulsation in distributed bragg reflector semiconductor lasers,” *IEEE Journal of Quantum Electronics*, vol. 43, no. 2, pp. 147–156, 2007.
- [138] M. R. E. Lamont, L. Fu, M. Rochette, D. J. Moss, and B. J. Eggleton, “2R optical regenerator in As_2Se_3 chalcogenide fiber characterized by a frequency-resolved optical gating analysis,” *Applied Optics*, vol. 45, no. 30, pp. 7904–7907, 2006.

- [139] S. Asimakis, F. Parmigiani, P. Petropoulos, D. J. Richardson, N. Sugimoto, and F. Koizumi, "A 2-m-long reshaping regenerator based on a highly nonlinear bismuth oxide fiber," in *Proc. Optical Fiber Communication*, 2006, p. OThB5.
- [140] M. Pelusi, V. Ta'eed, M. Lamont, S. Madden, D.-Y. Choi, B. Luther-Davies, and B. Eggleton, "Ultra-high nonlinear As_2S_3 planar waveguide for 160-Gb/s optical time-division demultiplexing by four-wave mixing," *IEEE Photonics Technology Letters*, vol. 19, no. 19, pp. 1496–1498, 2007.